



IJOER
RESEARCH JOURNAL

ISSN

2395-6992

International Journal of Engineering Research & Science

www.ijoer.com

www.adpublications.org

Volume-5! Issue-9! September, 2019

www.ijoer.com ! info@ijoer.com

Preface

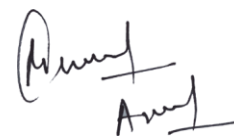
We would like to present, with great pleasure, the inaugural volume-5, Issue-9, September 2019, of a scholarly journal, *International Journal of Engineering Research & Science*. This journal is part of the AD Publications series *in the field of Engineering, Mathematics, Physics, Chemistry and science Research Development*, and is devoted to the gamut of Engineering and Science issues, from theoretical aspects to application-dependent studies and the validation of emerging technologies.

This journal was envisioned and founded to represent the growing needs of Engineering and Science as an emerging and increasingly vital field, now widely recognized as an integral part of scientific and technical investigations. Its mission is to become a voice of the Engineering and Science community, addressing researchers and practitioners in below areas

Chemical Engineering	
Biomolecular Engineering	Materials Engineering
Molecular Engineering	Process Engineering
Corrosion Engineering	
Civil Engineering	
Environmental Engineering	Geotechnical Engineering
Structural Engineering	Mining Engineering
Transport Engineering	Water resources Engineering
Electrical Engineering	
Power System Engineering	Optical Engineering
Mechanical Engineering	
Acoustical Engineering	Manufacturing Engineering
Optomechanical Engineering	Thermal Engineering
Power plant Engineering	Energy Engineering
Sports Engineering	Vehicle Engineering
Software Engineering	
Computer-aided Engineering	Cryptographic Engineering
Teletraffic Engineering	Web Engineering
System Engineering	
Mathematics	
Arithmetic	Algebra
Number theory	Field theory and polynomials
Analysis	Combinatorics
Geometry and topology	Topology
Probability and Statistics	Computational Science
Physical Science	Operational Research
Physics	
Nuclear and particle physics	Atomic, molecular, and optical physics
Condensed matter physics	Astrophysics
Applied Physics	Modern physics
Philosophy	Core theories

Chemistry	
Analytical chemistry	Biochemistry
Inorganic chemistry	Materials chemistry
Neurochemistry	Nuclear chemistry
Organic chemistry	Physical chemistry
Other Engineering Areas	
Aerospace Engineering	Agricultural Engineering
Applied Engineering	Biomedical Engineering
Biological Engineering	Building services Engineering
Energy Engineering	Railway Engineering
Industrial Engineering	Mechatronics Engineering
Management Engineering	Military Engineering
Petroleum Engineering	Nuclear Engineering
Textile Engineering	Nano Engineering
Algorithm and Computational Complexity	Artificial Intelligence
Electronics & Communication Engineering	Image Processing
Information Retrieval	Low Power VLSI Design
Neural Networks	Plastic Engineering

Each article in this issue provides an example of a concrete industrial application or a case study of the presented methodology to amplify the impact of the contribution. We are very thankful to everybody within that community who supported the idea of creating a new Research with IJOER. We are certain that this issue will be followed by many others, reporting new developments in the Engineering and Science field. This issue would not have been possible without the great support of the Reviewer, Editorial Board members and also with our Advisory Board Members, and we would like to express our sincere thanks to all of them. We would also like to express our gratitude to the editorial staff of AD Publications, who supported us at every stage of the project. It is our hope that this fine collection of articles will be a valuable resource for *IJOER* readers and will stimulate further research into the vibrant area of Engineering and Science Research.



Mukesh Arora
(Chief Editor)

Board Members

Mukesh Arora(Editor-in-Chief)

BE(Electronics & Communication), M.Tech(Digital Communication), currently serving as Assistant Professor in the Department of ECE.

Prof. Dr. Fabricio Moraes de Almeida

Professor of Doctoral and Master of Regional Development and Environment - Federal University of Rondonia.

Dr. Parveen Sharma

Dr Parveen Sharma is working as an Assistant Professor in the School of Mechanical Engineering at Lovely Professional University, Phagwara, Punjab.

Prof.S.Balamurugan

Department of Information Technology, Kalaignar Karunanidhi Institute of Technology, Coimbatore, Tamilnadu, India.

Dr. Omar Abed Elkareem Abu Arqub

Department of Mathematics, Faculty of Science, Al Balqa Applied University, Salt Campus, Salt, Jordan, He received PhD and Msc. in Applied Mathematics, The University of Jordan, Jordan.

Dr. AKPOJARO Jackson

Associate Professor/HOD, Department of Mathematical and Physical Sciences, Samuel Adegboyega University, Ogwa, Edo State.

Dr. Ajoy Chakraborty

Ph.D.(IIT Kharagpur) working as Professor in the department of Electronics & Electrical Communication Engineering in IIT Kharagpur since 1977.

Dr. Ukar W.Soelistijo

Ph D , Mineral and Energy Resource Economics, West Virginia State University, USA, 1984, Retired from the post of Senior Researcher, Mineral and Coal Technology R&D Center, Agency for Energy and Mineral Research, Ministry of Energy and Mineral Resources, Indonesia.

Dr. Samy Khalaf Allah Ibrahim

PhD of Irrigation &Hydraulics Engineering, 01/2012 under the title of: "Groundwater Management Under Different Development Plans In Farafra Oasis, Western Desert, Egypt".

Dr. Ahmet ÇİFCİ

Ph.D. in Electrical Engineering, Currently Serving as Head of Department, Burdur Mehmet Akif Ersoy University, Faculty of Engineering and Architecture, Department of Electrical Engineering (2015-...)

Dr. Mohamed Abdel Fatah Ashabrawy Moustafa

Ph.D. in Computer Science - Faculty of Science - Suez Canal University University, 2010, Egypt.

Assistant Professor Computer Science, Prince Sattam bin AbdulAziz University ALkharj, KSA.

Dr. Heba Mahmoud Mohamed Afify

Ph.D degree of philosophy in Biomedical Engineering, Cairo University, Egypt worked as Assistant Professor at MTI University.

Dr. Aurora Angela Pisano

Ph.D. in Civil Engineering, Currently Serving as Associate Professor of Solid and Structural Mechanics (scientific discipline area nationally denoted as ICAR/08—"Scienza delle Costruzioni"), University Mediterranea of Reggio Calabria, Italy.

Dr. Faizullah Mahar

Associate Professor in Department of Electrical Engineering, Balochistan University Engineering & Technology Khuzdar. He is PhD (Electronic Engineering) from IQRA University, Defense View, Karachi, Pakistan.

Dr. S. Kannadhasan

Ph.D (Smart Antennas), M.E (Communication Systems), M.B.A (Human Resources).

Dr. Christo Ananth

Ph.D. Co-operative Networks, M.E. Applied Electronics, B.E Electronics & Communication Engineering Working as Associate Professor, Lecturer and Faculty Advisor/ Department of Electronics & Communication Engineering in Francis Xavier Engineering College, Tirunelveli.

Dr. S.R.Boselin Prabhu

Ph.D, Wireless Sensor Networks, M.E. Network Engineering, Excellent Professional Achievement Award Winner from Society of Professional Engineers Biography Included in Marquis Who's Who in the World (Academic Year 2015 and 2016). Currently Serving as Assistant Professor in the department of ECE in SVS College of Engineering, Coimbatore.

Dr. Maheshwar Shrestha

Postdoctoral Research Fellow in DEPT. OF ELE ENGG & COMP SCI, SDSU, Brookings, SD
Ph.D, M.Sc. in Electrical Engineering from SOUTH DAKOTA STATE UNIVERSITY, Brookings, SD.

Zairi Ismael Rizman

Senior Lecturer, Faculty of Electrical Engineering, Universiti Teknologi MARA (UiTM) (Terengganu) Malaysia
Master (Science) in Microelectronics (2005), Universiti Kebangsaan Malaysia (UKM), Malaysia. Bachelor (Hons.) and Diploma in Electrical Engineering (Communication) (2002), UiTM Shah Alam, Malaysia

Dr. D. Amaranatha Reddy

Ph.D.(Postdoctoral Fellow,Pusan National University, South Korea), M.Sc., B.Sc. : Physics.

Dr. Dibya Prakash Rai

Post Doctoral Fellow (PDF), M.Sc.,B.Sc., Working as Assistant Professor in Department of Physics in Pachhunga University College, Mizoram, India.

Dr. Pankaj Kumar Pal

Ph.D R/S, ECE Deptt., IIT-Roorkee.

Dr. P. Thangam

BE(Computer Hardware & Software), ME(CSE), PhD in Information & Communication Engineering, currently serving as Associate Professor in the Department of Computer Science and Engineering of Coimbatore Institute of Engineering and Technology.

Dr. Pradeep K. Sharma

PhD., M.Phil, M.Sc, B.Sc, in Physics, MBA in System Management, Presently working as Provost and Associate Professor & Head of Department for Physics in University of Engineering & Management, Jaipur.

Dr. R. Devi Priya

Ph.D (CSE),Anna University Chennai in 2013, M.E, B.E (CSE) from Kongu Engineering College, currently working in the Department of Computer Science and Engineering in Kongu Engineering College, Tamil Nadu, India.

Dr. Sandeep

Post-doctoral fellow, Principal Investigator, Young Scientist Scheme Project (DST-SERB), Department of Physics, Mizoram University, Aizawl Mizoram, India- 796001.

Mr. Abilash

MTech in VLSI, BTech in Electronics & Telecommunication engineering through A.M.I.E.T.E from Central Electronics Engineering Research Institute (C.E.E.R.I) Pilani, Industrial Electronics from ATI-EPI Hyderabad, IEEE course in Mechatronics, CSHAM from Birla Institute Of Professional Studies.

Mr. Varun Shukla

M.Tech in ECE from RGPV (Awarded with silver Medal By President of India), Assistant Professor, Dept. of ECE, PSIT, Kanpur.

Mr. Shrikant Harle

Presently working as a Assistant Professor in Civil Engineering field of Prof. Ram Meghe College of Engineering and Management, Amravati. He was Senior Design Engineer (Larsen & Toubro Limited, India).

Table of Contents

S.No	Title	Page No.
1	<p>Modeling and Monitoring the Experimental Implant for Measuring the Ethanol Concentration Authors: Erinda Piluri, Dhurata Premti</p> <p> DOI: https://dx.doi.org/10.5281/zenodo.3465237</p> <p> DIN Digital Identification Number: IJOER-SEP-2019-1</p>	01-03
2	<p>Tannic Acid-Terminated Poly(Propylene Oxide) as Efficient Dispersant for Multi-Walled Carbon Nanotube to Prepare Highly Conductive Composites Authors: Pei-Ni Song, Jin-Long Hong</p> <p> DOI: https://dx.doi.org/10.5281/zenodo.3465251</p> <p> DIN Digital Identification Number: IJOER-SEP-2019-2</p>	04-18
3	<p>Features of some interacting tropical cyclones in the Indian Ocean after the Mount Pinatubo eruption Authors: Vladimir Kostin, Gennady Belyaev, Olga Ovcharenko, Elena Trushkina</p> <p> DOI: https://dx.doi.org/10.5281/zenodo.3465257</p> <p> DIN Digital Identification Number: IJOER-SEP-2019-3</p>	19-26
4	<p>Novel Combinative Structure of High-Performance Solar Steam Device derived from Areca Nut Authors: Tzu-min Chou, Jin-Long Hong</p> <p> DOI: https://dx.doi.org/10.5281/zenodo.3465269</p> <p> DIN Digital Identification Number: IJOER-SEP-2019-4</p>	27-34
5	<p>Discussion on Inexact Optimal Solution under Fuzzy Environment Authors: Pei-Chun Feng</p> <p> DOI: https://dx.doi.org/10.5281/zenodo.3470678</p> <p> DIN Digital Identification Number: IJOER-SEP-2019-5</p>	35-41

6	<p>Discussion of two motivations provided by Sphicas 2006 Authors: Pei-Chun Feng</p> <p> DOI: https://dx.doi.org/10.5281/zenodo.3470682</p> <p> DIN Digital Identification Number: IJOER-SEP-2019-8</p>	42-47
7	<p>Discussion on Weighted Similarity Measure under Intuitionistic Fuzzy Sets Environment Authors: Edward Lin, Daniel Schaeffer</p> <p> DOI: https://dx.doi.org/10.5281/zenodo.3470686</p> <p> DIN Digital Identification Number: IJOER-SEP-2019-10</p>	48-56

Modeling and Monitoring the Experimental Implant for Measuring the Ethanol Concentration

Erinda Piluri¹, Dhurata Premti²

¹General Directorate of Metrology, Albania

²Department of Industrial Chemistry, University of Tirana, Faculty of Natural Sciences, Albania

Abstract- *In this set of experiments we have tried to monitor a system of three reactors placed in series through experimental measurements of the ethanol concentration, temperature, flow and pressure at the outlet of system. We compared the results when the system has different metallic tubes used between vessels. For each set of experiments, we have used tubes with 6 and 8 mm diameter because they influence the pressure drop in our system.*

Keywords- *Continuous system, Ethanol concentration, flow, pressure and temperature parameters.*

I. INTRODUCTION

The objective of this experimental work is to determine the concentration of ethanol in a system and to study the parameters affecting it. An important part are also the factors that are influencing the calibration solution. We can mention the physical and chemical properties of each component; the interval of ethanol concentration on the solution and the ability to work and change the parameters in the solution (temperature, pressure, flow).



FIGURE 1: System for monitoring the ethanol concentration.

II. RESULTS

In this set of experiments we have tried to monitor a system of three reactors placed in series through experimental measurements of the ethanol concentration, flow, pressure and temperature at the outlet of system. We compared the results when the system has different metallic tubes used between vessels. For each set of experiments, we have used tubes with 6 and 8 mm diameter. The gas flow was kept from 10 to 20 L/min and temperature 34 °C. After receiving all the values from the experiments we had these results:

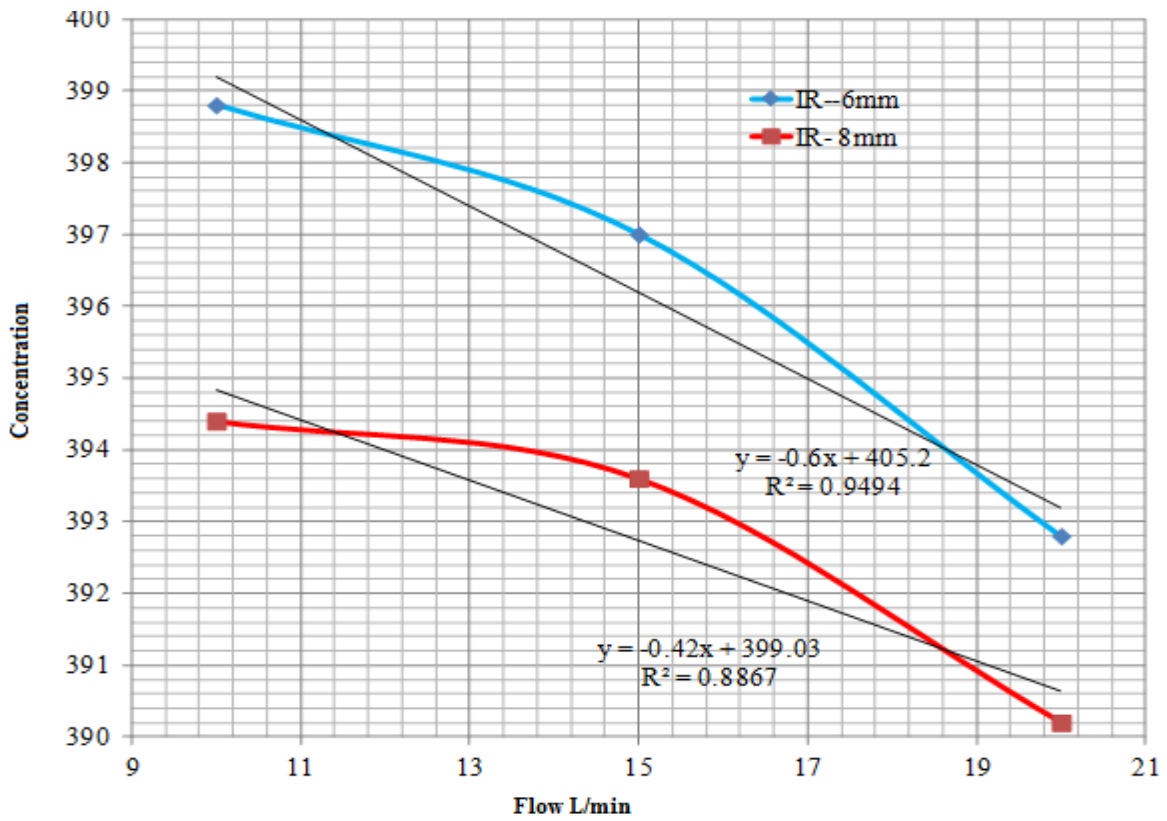


FIGURE 2: Graphic presentation of flow dependency from concentration with 6 and 8 mm connectors

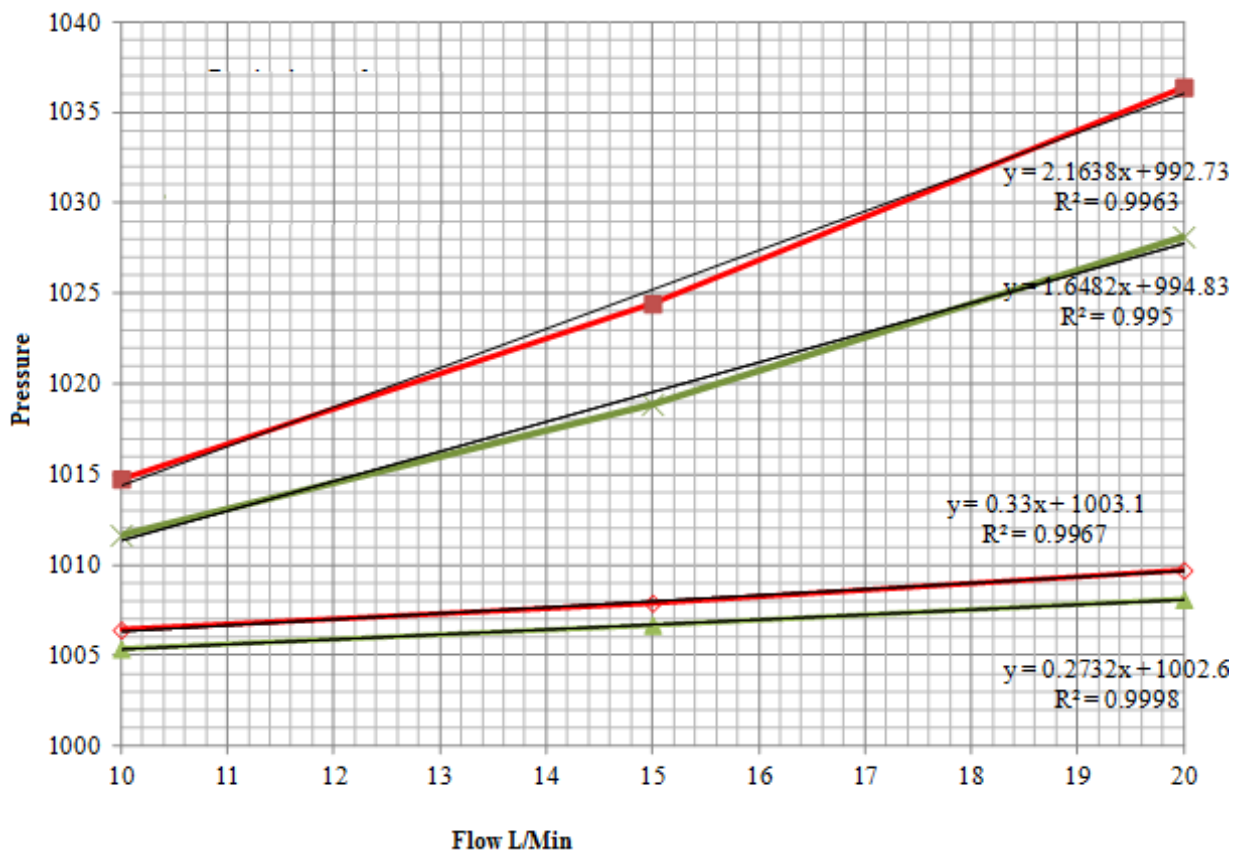


FIGURE 3: Graphic presentation of flow dependency from pressure with 6 and 8 mm connectors

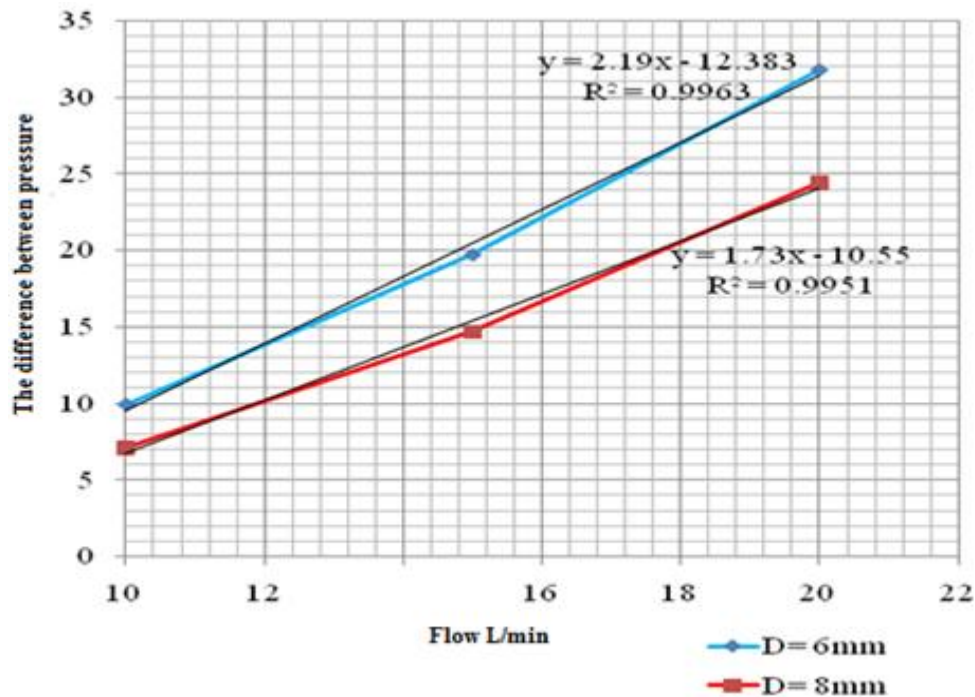


FIGURE 4: Graphic presentation of flow dependency from the difference of pressure with 6 and 8 mm connectors

III. CONCLUSION

We studied the dynamic model that gives the correlation of ethanol concentration with parameters affecting thermodynamic equilibrium. The parameters:

- **Temperature** – The increase of the temperature, rise an increase of ethanol concentration in the gaseous phase with a fixed ratio of ethanol separation in the gas on the solution.
- **Pressure**- The increase of the pressure drop difference results reduces the decrease in the gas phase concentration.
- **Flow rate**- The increase of the flow rate of gas reduces the ethanol concentration in gaseous phase.

ACKNOWLEDGEMENTS

The measurements are done in the laboratory of General Directorate of Metrology in Albania. The acknowledgement goes for this institution.

REFERENCES

- [1] *The role of the drinking driver in traffic accidents (The Grand Rapids Study)*, R.F. Borkenstein, R.F.Crowther, R.P. Shumate, W.B. Ziel, R. Zylman, 1964, Department of Police Administration, Indiana University and 1974, Blutalkohol, Vol. 11, Supplement 1
- [2] *Beweissicherheit der Atemalkoholanalyse*, G. Schoknecht, 1992, Unfall- und Sicherheitsforschung Straßenverkehr, Volume 86 (1992)
- [3] *OIML R 126 Evidential breath analyzers*, OIML, 1998
- [4] *Guide to the expression of uncertainty in measurement (GUM)*, ISO, 1995
- [5] *Breath-Alcohol Simulators: Scientific Basis and Actual Performance*, K.M. Dubowski, 1979, Journal of Analytical Toxicology, Vol.3, Sept./October 1979, pp. 177-182
- [6] *A New Wet Bath Simulator System with Depletion Compensation for Calibrating Evidential Breathalcohol Analyzers*, A. Slemeyer, 2001, Blutalkohol Vol. 38/2001, pp. 1-6.

Tannic Acid-Terminated Poly(Propylene Oxide) as Efficient Dispersant for Multi-Walled Carbon Nanotube to Prepare Highly Conductive Composites

Pei-Ni Song¹, Jin-Long Hong^{2*}

¹Department of Materials and Optoelectronic Science, National Sun Yat-sen University

^{2*}Department of Materials and Optoelectronic Science, National Sun Yat-sen University, Kaohsiung, Taiwan 80424, ROC

Abstract—In this study, multi-functional tannic acid (TA) was incorporated with soft poly(propylene oxide) (PPO) chain to result in a TA-terminated JTA polymer, in which the TA terminals impart reversible aromatic π - π and hydrogen bond (H bond) interactions to JTA polymer. Moreover, the aromatic TA terminals of JTA can preferably bind to the surface carbon rings of multi-walled carbon nanotubes (MWCNTs) to result in JCTx composites containing large amounts (up to 96 wt%) of MWCNTs. The sorption isotherm study indicated a two-step sorption mechanism of the sorbed JTA on MWCNT. Dependent on the MWCNT content, JCTx composites can be healable elastomers with high fracture strain (up to 700%) or plastics with outstanding conductivity (up to $1.21 \times 10^6 \text{ m}^{-1}$). Experimental mechanical modulus and conductivity of JCTx also were approached by the theoretical Kolarik model and scaling law, respectively. The result was explained in term of morphological arrangement of the MWCNT, evaluated from scanning and transmission) electron microscopies in JTA matrix. This study provided theoretical evaluation of highly MWCNT-loaded composites.

Keywords—Tannic acid, MWCNT, carbon material dispersion, π - π stacking, hydrogen bonding, conductive composite, Kolarik model, scaling law.

I. INTRODUCTION

Molecular engineering using delicate design and testing of molecular structures and interactions enables the fabrication of advanced materials with different application fields. Given the extraordinary mechanical, electrical, and thermal properties, carbon nanotubes (CNTs) provided versatile routes for the preparations of advanced materials, among them, polymer/CNT nanocomposites^{1,2} were studied frequently despite the existing difficulty in fabricating homogenous composite products. Primarily, dispersing CNTs without destroying the superior mechanical and electrical properties, with some notable exceptions (<10%)³⁻⁵, were hampered by the lack of effective method in dispersing large amounts of CNTs. Primarily, it is difficult to disperse nanotubes in water due to the repulsive interactions⁶⁻⁸ between nanotubes and water. Moreover, the large attractive interparticle potential between the nanoscale tubes^{9,10} caused the easy formation of aligned aggregated tubes. Several methods have been developed to disperse CNTs¹¹⁻¹³ previously, nevertheless, the amounts of nanotubes incorporated in the polymer composites are limited ($\leq 10 \text{ wt}\%$) due to the preferable aggregation tendency of nanotubes in the polymer solutions.

Introducing conductive materials into insulating hosts¹⁴⁻¹⁶ always is an attracting topic because of the scientific and practical importance. The electrical conductivity of nanotubes can reach 10^6 S m^{-1} , but polymer matrices usually are poor in conductivity with values between 10^{-16} and $10^{-12} \text{ S m}^{-1}$. Adding small amounts of nanotubes to polymer matrices significantly increased the conductivity¹⁷⁻²⁴ (to 10^{-6} S m^{-1} , approximately), which stimulated the practical applications of polymer/carbon nanotube (PCNT) composites in electronics, sensors, and actuators, as well as many others^{25,26} in the electronics industry. The critical concentration^{27,28}, known as percolation threshold, at which conductive networks start to form is inversely related to the aspect ratio (length per diameter) of the dispersed nanomaterials. Regarding the high aspect ratio of nanotubes, PCNT nanocomposites generally exhibit extremely low (< 0.5 wt%) percolation thresholds²⁹⁻³³. Experimental and theoretical approaches for the percolation thresholds indicated that conductivity of PCNTs was limited by the potential barriers between nanotubes and polymer because the surfaces of the nanotube bundles always were covered by polymer coatings.

Besides conductivity, a percolation threshold, known as mechanical percolation, also was observed in the mechanical tests of PCNTs. Previous study^{34,35} had interpreted the high levels of modulus in reinforced composites and nanocomposites by mechanical percolation. CNTs show Young's moduli of around 1000 GPa as well as tensile strengths in range from 10 to 50 GPa³⁶. The excellent mechanical performance as well as the extraordinary physical properties, such as high aspect ratios and large surface areas, justifies their beneficial role in PCNTs. Again, the advantage of nanotubes was only realized when they are uniformly dispersed in the polymer matrices, because that they tend to aggregate/agglomerate³⁷ seriously in the processing solution step. Therefore, more promising PCNTs³⁸⁻⁴⁹ with low (e.g. 0.8 wt%), medium (e.g. 10 wt%) and high (e.g. 33 wt%) nanotube content had been previously attempted. Among them, poly(acrylic acid)/poly(ethylene oxide)-poly(propylene oxide)-poly(ethylene oxide)⁴⁹ (PAA/F108) was used as excellent dispersant of CNT to result in PCNT with a high amount (33 wt%) of CNT. The facile hydrogen bond (H bond) interactions between carboxylic acids in PAA and over the active surface of CNT are responsive for the homogeneity of the resulting PCNTs.

As a universal environmental organic molecule, tannic acid (TA)^{50,51} was previously used as effective dispersant for CNTs. The enriched aromatic rings and phenolic hydroxyl OH groups of TA are responsible for the effective dispersion of CNTs and accordingly, a two-stage sorption mechanism⁵⁰ was proposed: the TA molecules were adsorbed first onto the surfaces of CNTs with the aromatic rings binding to the surface carbon rings of CNT via the aromatic π - π interactions, forming a monolayer in the interface, which further adsorbed the dissolved TA molecules by the self-interacting H bonding and other possible polar interactions. The adsorbed TA molecules increased the steric repulsion between individual CNT, which then acted to disperse the loose CNT aggregates to result in the stabilization of CNTs in the TA solution. The sorption and suspending process also was examined by transmission electron (TEM) microscopy, providing further evidence for the above sorption mechanism.

In this study, we designed and synthesized a TA-terminated poly(propylene oxide) (PPO) of JTA (Scheme 1), which turned out to be effective sorbent for MWCNT exclusively binding to various amount of MWCNT to result in JCTx (x: wt% of MWCNT, ranging from 1 to 96) composites with high conductivity (from 1.20×10^{-3} to $1.21 \times 10^6 \text{ S m}^{-1}$) and excellent mechanical properties to be studied with. The multi-functional JTA polymer is an elastomer due to its unique molecular feature that the soft PPO chain is the mobile and stretchable part while the aromatic π - π and H bond interaction sites of TA terminals provide mechanical strength susceptible to external deformation. TA terminals of JTA also imparted exclusive aromatic π - π interactions to the surface carbon rings of MWCNT, rendering stretchable elastomer (while MWCNT content is low (≤ 40 wt%)) or hard conductive plastics (while MWCNT content is higher than 40 wt%) with interesting mechanical and conductive properties to be studied with. Rather than previous study^{52,53} always concentrated on PCNTs with concentration below percolation threshold, the JCTx composites provided us the opportunity to approach the experimental mechanical modulus (E) and conductivity with theoretical Kolarik model⁵⁴ and scaling law⁵⁵, respectively, at concentration well beyond percolation threshold. Starting from the sorption study in the solution state, a two-stage sorption model was proposed to illustrate the interaction between MWCNTs and JTA. Mechanical and conductive properties of the solid composites also were correlated with the morphological arrangement of MWCNTs in JTA matrix evaluated from scanning (SEM) and transmission (TEM) electron microscopies. This study therefore provided theoretical background on the highly MWCNT-loaded PCNTs.

II. EXPERIMENTAL

2.1 Materials

Amine-terminated PPO (Jeffamine, $M_n=4,684$ g/mol, Sigma-Aldrich) and hexamethylene diisocyanate (HDI, $M_n=168$ g/mol, Acros) and TA ($M_n=1,701$ g/mol, Acros) were directly used without purification. MWCNT was purchased from Golden Innovation Business Co., Ltd, which was claimed to have inner and outer diameters of 10 nm and 20 nm, and 1 to 2 μm in length, respectively. Preparation method is Model equation and parameter definition (CVD). *N,N*-dimethyl formamide (DMF) was refluxed over CaH_2 for two days in prior to distillation for use.

2.2 Preparation of JTA

The JTA was synthesized by a two-step reaction procedure (Scheme 1). Briefly, solution of Jeffamine (5g, 1.07 mmol) and HDI (0.38 g, 2.25 mmol) in dry DMF (25 mL) were heated at 70 °C for 3 hr to result in homogeneous JHDI solution. A small portion of the solution was taken and extracted by hexane before being precipitated from distilled water to obtain JHDI for analysis. Afterwards, TA (4.55 g, 2.68 mmol) was added to the solution mixture and the reaction was continued at 80 °C for another 24 hr. The reaction mixture was then cooled to room temperature and extracted by hexane for several times before being precipitated from distilled water. The slurry-like product was filtered and dried at 70 °C for 24 hr under vacuum.

2.3 Preparation of conductive composite film

Calculated amounts of JTA and MWCNT were sonicated in DMF (5 mL) for 1 hr to ensure complete dispersion of MWCNT. The resulting homogeneous solution was then dried under vacuum for 24 hr to result in JCTx composite films for study.

2.4 Sorption and Stabilization Experiments

Sorption isotherms were obtained using a batch equilibration technique at 25°C. Two hundred milligrams of MWCNTs were added into 20 mL vials with different JTA concentrations of 0.8, 9, 44.5, 89, 445 and 890 mg/L. The whole vial was sonicated for 1 hr before standing still for equilibration for 7 days, and the resulting supernatants, the stable suspensions possibly with dispersed individual nanotubes, were taken out and measured with UV-Vis spectrometer (Jasco V-770, USA) at 800 nm. Measurement at 800 nm had been used to quantify MWCNTs in DMF phase. Preliminary experiments indicated that the absorbances at 800 nm are the same for solutions after being sonicated for 0.5 hr and 3 hr, thus, the suspended MWCNTs in the supernatants after sonication were considered to be stable in JTA solutions.

2.5 Characterizations

¹H NMR spectra were measured using a Varian Unity VXR-500 MHz spectrometer (McKinley Scientific, Sparta, NJ, USA), with *d*₆-DMSO as the solvent and tetramethylsilane (TMS) as the external standard. A mass spectrum was obtained by using a Bruker Daltonics Autoflex III MalDI-ToF mass spectrometer with *trans*-2-[3-(4-*tert*-butylphenyl)-2-methyl-2-propenylidene] malononitrile (DCTB) as matrix material. The number and weight-average molecular weights (M_n and M_w) and polydispersity (PDI) were determined from gel permeation chromatography (GPC) using a Waters 510 high-performance liquid chromatography system and DMF at 45 °C as the eluent (flow rate: 0.6 mL min⁻¹). The electric properties were determined at room temperature by an LCR Tonghui TH 2829 meter at 1 kHz with each data point as the average value of five measurements. Bright field TEM images of mass-thickness contrast were obtained using a Jeol JEM 2100 TEM spectrometer at an accelerating voltage of 200 kV. The samples were prepared by air-drying a drop of the suspensions onto a copper TEM grid. SEM images were obtained using a Jeol JSM 6700F microscope operated at 10 kV.

III. RESULT AND DISCUSSION

As illustrated in Scheme 2, the preparation of the desired polymer JTA required the preliminary synthesis of a key precursor JHDI. The reaction of the amino terminals of Jeffamine with excess (2.1 eq) HDI resulted in an isocyanate-terminated JHDI, which under attack of the phenolic OH groups of TA (2.5 eq) produced the desired JTA for study. To examine the efficiency of the applied end-capping reaction, the ¹H NMR spectrum of JTA, including all peak assignments, was compared with those of *d*₆-DMSO, Jeffamine and JHDI in Figure 1. The average HDI unit per Jeffamine chain of JHDI was determined from the integration ratio between resonance protons H_e at 2.89 ppm and H_{a,d} at 0.93-1.14 ppm. Here, the peak intensity of protons H_e was used to calculate the fraction of H_d in the overlapped H_{a,d} peaks as H_e and H_d belong to the same hexamethyl unit of HDI terminals with a fixed ratio of 1 to 2. Accordingly, the average HDI unit per Jeffamine chain of JHDI is 1.93. Likewise deduction, from the integration ratio between protons H_{h1+h2+j1+j2} and H_{a,d}, resulted in an average 1.89 TA terminals per JTA chain. The resolved M_n s (5,009 g/mol for JHDI and 8,289 g/mol for JTA) listed in Table 1 are comparable with those determined from MalDI-ToF mass spectroscopy but are smaller than those from the GPC analysis. The high molecular weights determined from GPC can only be regarded as reference values because GPC analysis involved only excluded volume of the polymer, rather than real molecular weights, in DMF eluent.

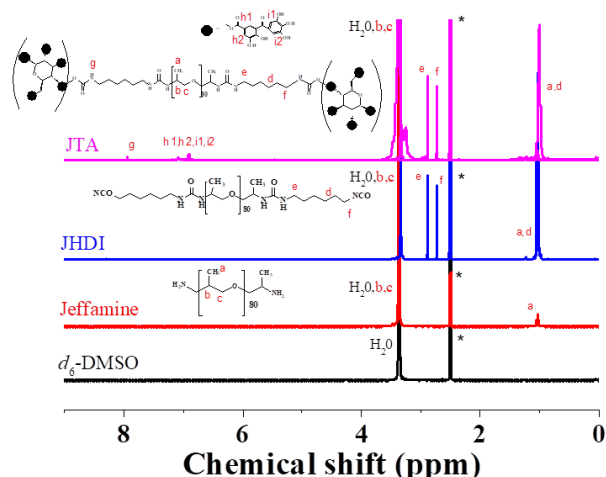


FIGURE 1. ^1H NMR spectra of d_6 -DMSO, Jeffamine, JHDI and TA-terminated JTA (d_6 -DMSO).

TABLE 1
MOLECULAR WEIGHT OF JHDI/JTA EVALUATED FROM ^1H NMR, MALDI-TOF MASS SPECTROSCOPY AND GPC

Sample	^1H NMR ^a	Maldi-Tof mass spectroscopy ^b			GPC ^c		
	M_n (g/mol)	M_n (g/mol)	M_w (g/mol)	PDI	M_n (g/mol)	M_w (g/mol)	PDI
JHDI	5009	5405	5545	1.03	6081	7175	1.18
JTA	8289	8952	9848	1.10	9445	11646	1.23

The resulting JTA is an elastomer with fracture strain (ϵ_f) of 813% at fracture stress (σ_f) of 0.2MPa (Figure S1) and moreover, it is a healable elastomer with high healing efficiency. All these referred to the unique molecular feature of JTA that the soft PPO chains represent the stretchable part while the aromatic TA terminals provide the reversible aromatic π - π and H bond interactions required for the mechanical strength and the observed autonomous recovery process. More importantly, the aromatic TA terminals of JTA can bind to MWCNT, rendering JCx composites with varied MWCNT contents (from 1 to 96 wt%).

3.1 Sorption isotherm and morphology

The superior mechanical and electrical behavior of MWCNT stimulated our study on using MWCNT as building block to develop advanced JCTx composites. Generally, transforming MWCNT into soluble materials that can be easily manipulated in the solution state may be subjected to dispersion difficulty and so, the effective utilization of MWCNT strongly depends on two factors: homogeneous dispersion of nanotubes throughout the polymer matrix without destroying the integrity of the tubes, and adequate interfacial adhesion between the nanotubes and polymers. The first factor can be demonstrated by the homogeneity of the solutions we prepared (Figure 2(a)), in which the dispersed MWCNTs can remained in the solution after a long period of time (> 1 month), which demonstrated the great dispersion power of JTA for MWCNTs. The second factor can be seen from the elastomeric properties of certain elastomeric JCTx ($x = 10$ to 40), which can sustain high strain (with high ϵ_f values ranging from 100 to 700%) without mechanical failure.

Basically, there are four commonly used models⁵⁶ for nonlinear isotherm behavior, including Langmuir (LM), Dual-mode (DMM), Dual-Langmuir (DLM), and Freundlich (FM) models. Specially, the LM was developed to describe individual chemical adsorbents and is applicable to monolayer physical adsorption⁵⁷, and DMM model was originally proposed for describing the sorption behavior of natural organic matters⁵⁸. The FM is an empirical approach for adsorbents with uneven adsorbing site energy and is applicable to adsorption for a single-solute system within high- and middle-concentration environments. For FM, the goodness of fit varied with the MWCNTs (Figure S2a). The results suggested that the fit of FM is better than LM at high concentration but is worse at other range. Good fit was obtained for DLM (Figure S2b) with adj r2

0.98. However, two parameters among the four, i.e., adsorbed capacity (Q_2^0) and DLM constant (b_2) of site population 2 were significantly unreliable with $p \gg 0.01$ (Table S1). Thus, the sorption process of JTA by MWCNTs may not be limited by the two types of adsorption sites. As a result⁵⁰, our initial attempt for sorption used both DMM and LM to fit our experimental result.

The result from LM estimation deviated from the experimental data of JTA by MWCNTs (Figure S3), which can be also seen from the low adj r^2 value of 0.87. Significant deviation of LM result from the experimental data was observed for LM at high concentration. The deviation indicates that the sorption of JTA, on the MWCNTs, may not be monolayer formation on a homogeneous surface, that is, the MWCNTs aggregated in the JTA solutions and the adsorbed JTA monolayer may continue to sorb the dissolved JTA molecules, via H bonds and other polar interactions, till the state that most MWCNT aggregates were surrounded by majority of JTA polymers.

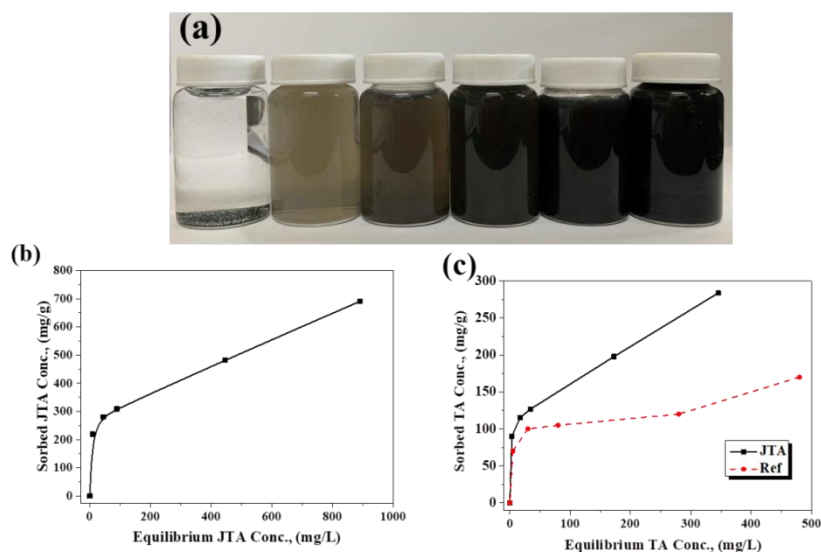


FIGURE 2. (a) Solutions of MWCNT (200 mg/L) in DMF (20 mL) with varied concentrations of JTA (from left to right: with 0, 8.9, 44.5, 89, 445 and 890 mg of JTA in 1 L of DMF, respectively) (b) sorption isotherms of JTA and MWCNTs revealed a good fit with the theoretical curves predicted by the dual-mode model (DMM) and (c) compared with the result based on pure TA (dashed line) and MWCNT of the same dimensions.

Sorption isotherms by DMM was examined in Figure 2(b), which exhibited non-linear relationship between equilibrium and sorbed JTA concentrations. We further transformed the JTA concentration into TA terminal concentration (Figure 2(c)) based on the ^1H NMR result that M_n of JTA is 8289 g/mol and there are 1.89 TA terminals per JTA chain. Both non-linear isotherms in Figure 2(b) and 2(c), using parameters (Table S1) of MWCNT with the respective inner and outer diameters of 10 and 20 nm, revealed a good fit between DMM estimation⁵⁸ and experimental results. The good fits (adj r^2 is 0.99) suggested that the sorption of JTA by MWCNT followed the same two-step sorption model previously proposed for pure TA on MWCNTs⁵⁰ that TA terminals of JTA may be sorbed first onto MWCNTs with its aromatic rings binding to the surface carbon rings of MWCNT via π - π interactions, until forming a monolayer, and then the JTA monolayer formed further sorbed the dissolved JTA by H bonds and other polar interactions. The sorbed JTA increased the steric repulsion between individual MWCNTs, which might disperse the relatively loose MWCNT aggregates and result in the stabilization of MWCNTs in JTA solution.

Experimental data in Figure 2(c) also compared with the result⁵⁰ from pure TA (dashed line) and MWCNT of the same dimensions. Despite being lower in TA concentration, JTA nevertheless is superior to pure TA in dispersing MWCNTs. We attributed this high dispersion power of JTA to two factors: DMF solvent used in our example is a better dispersion solvent for MWCNTs than water used in previous case. Moreover, with the PPO chain, JTA should be superior to TA in hydrophobicity and in dispersing the hydrophobic MWCNTs. The superior dispersion power of JTA thereby imparts high loads of MWCNTs in DMF, providing JCTx composites containing large amounts of MWCNTs (from 10 to 96 wt%) after removal of DMF.

The solid JCTx composites are either stretchable elastomers when $x \leq 40$ (Table 2) or rigid and highly conductive plastics when $x > 50$. The morphology of JCTx with small (40 wt%, Figure 3(a)), medium (70 wt%, Figure 3(b)) and large (96 wt%, Figure 3(c)) concentrations of MWCNTs was primarily examined by SEM. The resolved images are fundamentally similar with each other, all exhibiting tree branch-like bunches in micrometer sizes all over the samples. The randomly distributed branches should consist of inner MWCNT core wrapped by outer JCTx wall. The higher is the MWCNT content; the lower is the diameter of the resolved branches. The branches with smaller diameter may have tighter aggregation and entanglement, which may not be able to be dispersed by JTA during the preparation step in DMF. The looser agglomerates of the larger branches could be dispersed by JTA with shaking in DMF. The branch density also increased with increasing MWCNT content and the highest MWCNT-loaded JCT96 composite exhibited a morphology that the densely packed branches were interconnected with each other to result in a 3D crosslinked network with irregular, large knots, constituted by aggregated and entangled MWCNTs, as the crosslinking points to maintain the integrity of JCT96.

TABLE 2
CHARACTERISTICS OF THE JTA COMPOSITES FROM JCT1 TO JCT96

	Mass fraction p (%)	Volume fraction ϕ_f (%)	Density (g/ml)	Stretchability (ϵ_ϕ MPa, σ_f %)	Conductivity σ (S.m ⁻¹)
JTA	----	-----	1.17	Yes (813, 0.20)	----- ⁻³
JCT1	1	0.01	1.18	Yes (797, 0.23)	1.2×10 ⁻²
JCT10	10	0.09	1.20	Yes (690, 0.52)	7.14×10 ⁻¹
JCT20	20	0.18	1.24	Yes (524, 0.80)	9.84×10 ¹
JCT30	30	0.26	1.27	Yes (350, 3.09)	3.2×10 ²
JCT40	40	0.32	1.30	Yes (175, 6.06)	6.55×10 ³
JCT50	50	0.41	1.34	No (--)	3.02×10 ³
JCT60	60	0.49	1.37	No (--)	9.15×10 ⁴
JCT70	70	0.59	1.40	No (--)	6.76×10 ⁵
JCT80	80	0.70	1.43	No (--)	3.46×10 ⁵
JCT90	90	0.84	1.47	No (--)	8.31×10 ⁶
JCT96	96	0.92	1.49	No (--)	1.21×10 ⁶

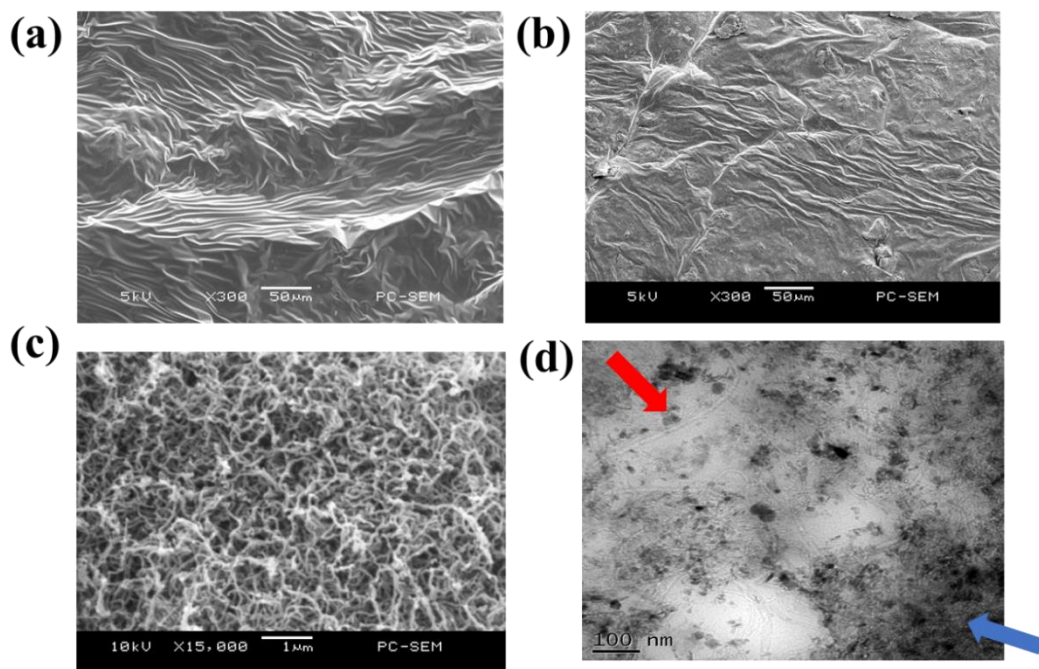


FIGURE 3. SEM images of (a) JCT40, (b) JCT70, and (c) JCT96 and TEM image of (d) JCT50

To see the interior of the tree branch, a JCT50 sample was then investigated by TEM. The small, white spherical images of the TEM micrograph (Figure 3(d)), which illustrated the vertical view of MWCNTs, are due to the inner empty core while the black images in between the white ones represent the outer wall of MWCNT. All these vertically erected MWCNTs are aggregated into large bundles and interestingly, all these vertical bundles are surrounded by extended rope-shaped tubes (red arrow), which represent the parallel view of MWCNT with the respective inner and outer diameters of 9.6 and 18.8 nm, close to the respective values of 10 and 20 nm given by the supplier. The sharp boundary between the inner vertical bundle and the outer parallel tube corresponds to flaws with mechanical weakness, which should lower the mechanical strength of the JCTx composites, a point will be discussed next. It is difficult to avoid aggregation of MWCNTs into bundle in considering that the TA terminals of JTA are insufficient in number to cover all the vast surfaces of the nano-sized MWCNTs. In consequence, a plethora of MWCNTs should associate together into large-sized bundles with much reduced surface areas to be covered by JTAs. Besides the MWCNT bundles, there are certain large black regions, which should correlate with the embedded JTA aggregates and the JTA polymer in the interphase region (blue arrow). Several vertical MWCNT bundles inside the interphase region may be an indication of how well the MWCNTs can be dispersed by JTA.

3.2 Mechanical properties of the JCTx composite films.

As the effective conductor, MWCNT also acted to reinforce the mechanical strength of the JCTx composites. Without MWCNT, pure JTA is soft and highly stretchable with the resolved ϵ_f value of 813% (Figure 4(a)) and the incorporation of rigid MWCNTs raised the mechanical strength at the expense of stretchability of the JCTx ($x \leq 40$) films. With 40 wt% of rigid MWCNT, the JCT40 composite is still an elastomer with a high ϵ_f value of near 200% (Table 2), which demonstrated the strong interfacial adhesion between MWCNT and JTA. Higher content of rigid MWCNT nevertheless resulted in non-stretchable, rigid JCTx ($x \geq 40$) composites. Because all the JCTx composites prepared in this study having a MWCNT content well beyond the percolation threshold (generally, < 0.1 wt%), the mechanical and conductive characterizations conducted hereafter are unprecedented.

Because the SEM image of JCT40 (Figure 3(a)) suggested the continuous distribution of the branches over the polymer matrices, the Kolarik⁵⁴ model based on a 3D cross-orthogonal skeleton (COS) should be appropriate in analyzing the mechanical property of the stretchable JCTx (x from 0 to 40 wt%) at concentration well above the percolation threshold. Based on the COS structure, Kolarik calculated the tensile modulus (E) of the composites with co-continuous morphology using:

$$E = E_m(1 - f^2) + E_f f^2 + [f(1-f) E_m] / [1 - f + (f E_m / E_f)] \quad (1)$$

$$1 - \Phi_f - (1-f)^2(1+2f) = 0 \quad (2)$$

Where in equation (1), E_f and E_m are the tensile moduli of the filler and the JTA polymer matrix, respectively, Φ_f is the filler volume fraction and the Φ_f -dependent parameter f can be determined from equation (2). Rather than small nanotubes, the filler phase contained in JCTx are large branches constituted by rigid MWCNT bundle core surrounded by soft JTA walls, which also is correlated with a 3D co-continuous structure and should be valid for Kolarik approach, too.

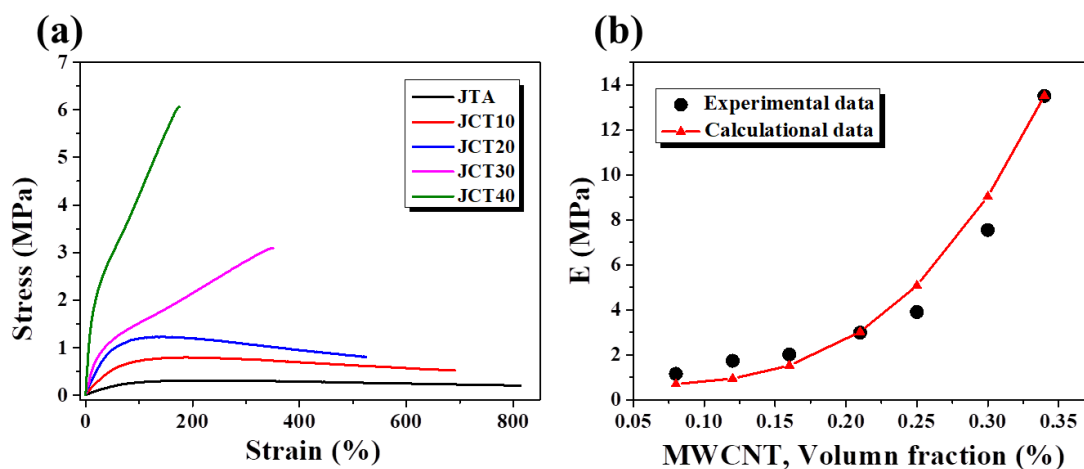


FIGURE 4. (a) Stress-strain curves and (b) comparison of the experimental moduli E_s of JCTx (x from 10 to 40) with the theoretical values determined from equation (1)

The experimental E values as function of MWCNT content were plotted in Figure 4(b) to correlate with the calculated results based on Kolarik model. The E_m , E_f and parameter f involved in calculation of the theoretical E values were summarized in Table S2. The results depicted in Figure 4(b) clearly indicated the fair agreement between the experimental and the theoretical data. The E_f value of 85.6 MPa was obtained from fitting experimental E value of JCT40 into equation (1). Previous approach had commented on the dilemma in evaluating the mechanical property of MWCNT: although the strength of individual CNT shells is extremely high (with E up to 1,000 GPa), weak shear interactions between adjacent shells and tubes lead to significant reduction⁵⁹ in the effective strength of MWCNTs and CNT bundles down to few GPa. The present case nevertheless illustrated an even lower E_f value of 85.6 MPa, which may be attributed to the nature of the structural unit evaluated from SEM and TEM analysis. Instead of MWCNT bundles, the responsive structural unit in JCTx is branches consisting of inner MWCNT bundles wrapped by the outer polymer wall. The embedded polymer and the polymer wall all are soft segments representative of mechanical weak points acting to lower the E value of the JCTx composites, which is plausible for the low E_f value of 85.6 MPa for JCT40.

3.3 Conductive properties of the JCTx composite films.

JTA polymer is an insulator but the incorporation of MWCNT with a concentration well beyond percolation threshold resulted in conductive composite with high conductivity (Table 2). At percolation threshold, conducting network forms in the polymer matrix starts to transfer electrons and creates the conductivity. SEM images (Figure 3(a) ~ (c)) revealed the presence of branches, which constituted the interconnected network effective in transferring electrons, in the JCTx composites. All JCTx composites are good at electron transfer according to the result that JCT1 is a semi-conductor with a conductivity of $1.2 \times 10^{-3} \text{ Sm}^{-1}$, and the increase of MWCNT content enhanced the conductivity to an ultimate high value of $1.21 \times 10^6 \text{ S m}^{-3}$ for JCT96. Essentially, the dense-packed branches of JCT96 contributed to its high conductivity, which is close to the conductivity (10^7 Sm^{-1}) of pure MWCNT.

According to classical percolation theory⁵⁵, the conductivity of composite materials as conductive filler content is increased can be described by a scaling law of the form

$$\sigma \propto (\pi - \pi_c)^t \quad (3)$$

where σ is conductivity, p is mass fraction, p_c is the electric percolation threshold (EPT)⁵⁵ and exponent t is expected to depend on sample dimensionality with calculated values of ~ 1.33 and ~ 2.0 in 2 D and 3 D arrangements, respectively. For the present case, p is much larger than p_c , therefore eqn (3) can be further simplified:

$$\sigma \propto p^t \quad (4)$$

In Figure 5(a), the dc conductivity data are shown on a semilogarithmic scale versus $\ln(p)$. The expected linear relationship is observed, with the solid line as a good fit with a slope of 1.92. The resulting t value of 1.92 for JCTx is found to agree with the universal value of 2 observed for composites in which the conductive fillers form a continuous 3D percolating path throughout the matrix⁶⁰. The percolation path of JCTx refers to the continuous branches distributed randomly in 3D dimension.

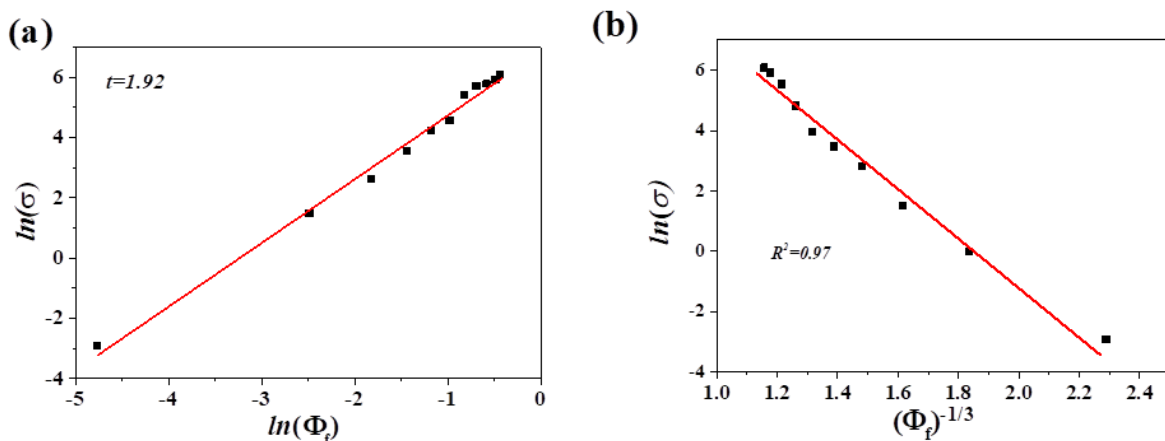


FIGURE 5. Comparison of experimental conductivity of JCTx (x from 10 to 96) with the theoretical values determined from the scaling law of (a) eqn (4) and (b) eqn (5)

The change in the electrical conductivity of the composite materials, when the EPT is reached in coincidence with the formation of a conductive path inside the material, can be interpreted in terms of electron tunneling. According to this model the electrons “jump” from a conductor to the closest stone over a small distance of the order of a few nanometers⁶¹. A method reported in literature^{62,63,55} to verify that the electron tunneling is the main electrical transport mechanism in nano filled resins is based on the occurrence of a linear relation (Fig. 5(b)) between the electrical conductivity (in natural logarithmic scale) and $p^{-1/3}$, valid for mass fraction (p) above EPT:

$$\ln(\sigma) \propto p^{-1/3} \quad (5)$$

The straight line is the fit curve of the experimental data: the value of R^2 here is close to 1, which confirms that the electrical conduction network in the composite materials is mainly achieved through the quantum tunneling effect. The current and therefore the electrical conductivity of the resulting composites are related to the intrinsic features of the adopted conductive filler. The conductive filler illustrates here covered the whole branch consisting of MWCNT core and JTA wall, which provides 3D conductive paths for fluent transport of electrons. The TEM and SEM images (Figure 3) suggested the presence of several conductive flaws, including boundary between the vertical MWCNT bundles and the surrounding parallel tubes, the interfacial region and the polymer insulator between branches, in the composites. At these conductive flaws, electrons had to “jump” from one MWCNT to the closest stone over a small distance of a few nanometers, resulting in the perfect fit of experimental data to equation (5).

IV. CONCLUSION

Through deliberate molecular engineering, we synthesized a TA-terminated JTA polymer with inherent aromatic phenolic rings and hydroxyl OH groups to promote the desired elasticity. The aromatic phenolic rings of JTA also bind to the surface carbon rings of MWCNTs, thus generating homogeneous JCTx composites with low (e.g. 10 wt%) and high (96 wt%) MWCNT contents.

Tree branches, constituted by inner MWCNT bundles and outer JTA walls, are interconnected with each other to form a 3 D crosslinked network of JCTx composites. With concentration well above percolation threshold, soft JCTx (x from 1 to 40 wt%) exhibited the elastic modulus correlated with theoretical Kolarix model based on All JCTx (x from 1 to 96) composites are conductive materials and the increase of MWCNT content largely promoted the composite conductivity to an ultimate excellent value of $1.2 \times 10^6 \text{ S m}^{-1}$ for the JCT96. The conductivity of the JCTx composites can be appropriately fitted by the scaling law of $\sigma \propto \rho^{-1.92}$ according to a 3D network model. The tree branches are responsible for the effective electron transfer and the ideal conductivity behaviors of the JCTx samples.

Dependent on the MWCNT content, the JCTx composite sensors can be highly stretchable or highly conductive. The highly conductive JCT96 is a sensitive sensor with keen response toward minor pulse beating. With good stretchability, the soft JCT40 is a stable sensor for the steady detection of large elbow bending motion. With the lowest MWCNT content, JCT10 is capable of repeatedly detecting a high strain of 220%. Through manipulating composite composition, JCTx sensors with the desired mechanical and conductive properties can be conveniently prepared and characterized. The developed JCTx composites in this study can also be applied to other practical application fields such as supercapacitor or lithium ion battery.

ACKNOWLEDGEMENTS

We appreciate the financial support from Ministry of Science and Technology (MOST), ROC, under the contract MOST 108-2221-E-110-015.

REFERENCES

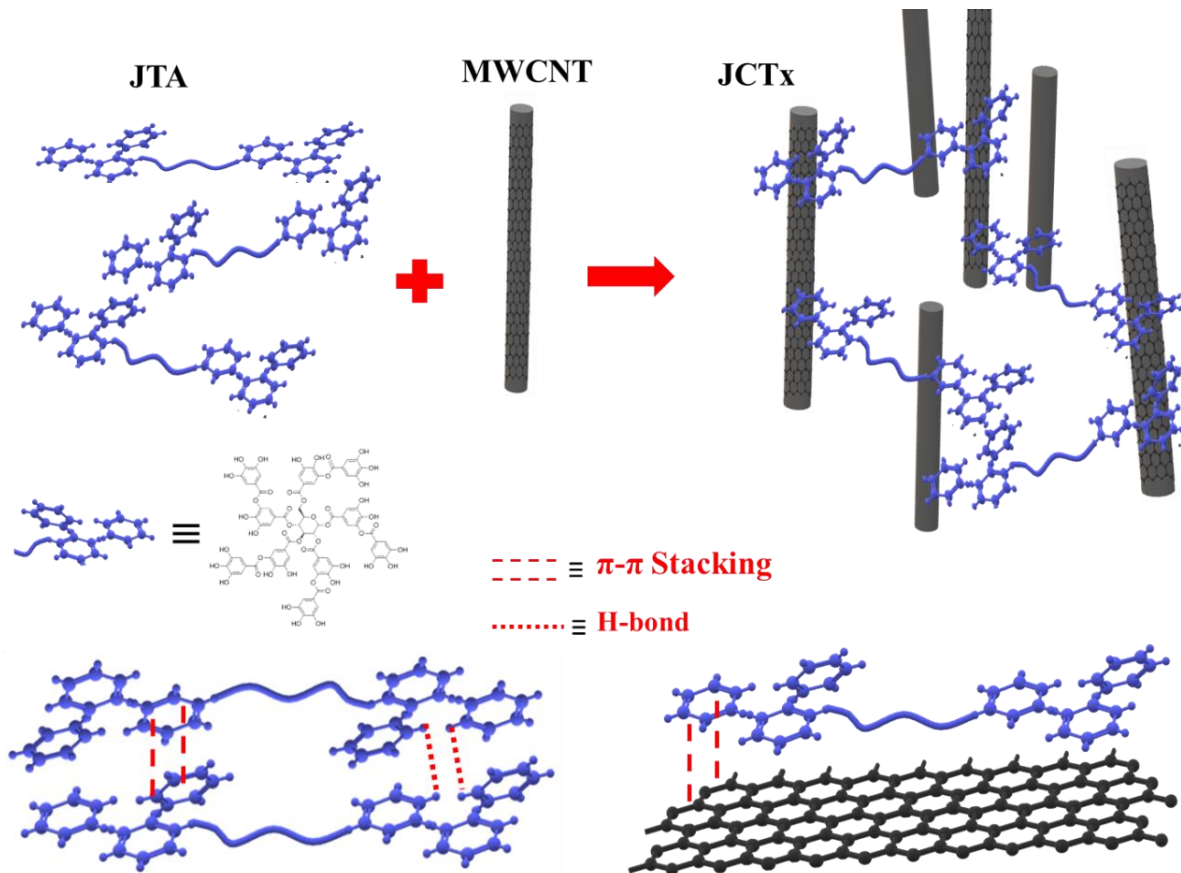
- [1] Ajayan, P. M., Nanotubes from carbon. Chemical reviews 1999, 99, 1787-1800.
- [2] Dresselhaus, G.; Riichiro, S., Physical properties of carbon nanotubes. World scientific: 1998.
- [3] Barraza, H. J.; Pompeo, F.; O'Rea, E. A.; Resasco, D. E., SWNT-filled thermoplastic and elastomeric composites prepared by miniemulsion polymerization. Nano letters 2002, 2, 797-802.
- [4] Du, F.; Fischer, J. E.; Winey, K. I., Coagulation method for preparing single-walled carbon nanotube/poly (methyl methacrylate) composites and their modulus, electrical conductivity, and thermal stability. Journal of Polymer Science Part B: Polymer Physics 2003, 41, 3333-3338.
- [5] Probst, O.; Moore, E. M.; Resasco, D. E.; Grady, B. P., Nucleation of polyvinyl alcohol crystallization by single-walled carbon nanotubes. Polymer 2004, 45, 4437-4443.
- [6] Hertel, T.; Walkup, R. E.; Avouris, P., Deformation of carbon nanotubes by surface van der Waals forces. Physical review B 1998, 58, 13870.

- [7] Heintz, A. M.; Risser, S. M.; Moore, B. P.; Elhard, J. D.; Cucksey, C. M., Carbon nanotube films and methods of forming films of carbon nanotubes by dispersing in a superacid. Google Patents: 2019.
- [8] Huang, Y. Y.; Terentjev, E. M., Dispersion of carbon nanotubes: mixing, sonication, stabilization, and composite properties. *Polymers* 2012, 4, 275-295.
- [9] Liang, Y.; Hilal, N.; Langston, P.; Starov, V., Interaction forces between colloidal particles in liquid: Theory and experiment. *Advances in colloid and interface science* 2007, 134, 151-166.
- [10] Israelachvili, J. N., Intermolecular and surface forces. Academic press: 2011.
- [11] Huang, J.-E.; Li, X.-H.; Xu, J.-C.; Li, H.-L., Well-dispersed single-walled carbon nanotube/polyaniline composite films. *Carbon* 2003, 41, 2731-2736.
- [12] Ma, P.-C.; Siddiqui, N. A.; Marom, G.; Kim, J.-K., Dispersion and functionalization of carbon nanotubes for polymer-based nanocomposites: a review. *Composites Part A: Applied Science and Manufacturing* 2010, 41, 1345-1367.
- [13] Qian, H.; Greenhalgh, E. S.; Shaffer, M. S.; Bismarck, A., Carbon nanotube-based hierarchical composites: a review. *J Mater Chem* 2010, 20, 4751-4762.
- [14] McLachlan, D.; Heaney, M. B., Complex ac conductivity of a carbon black composite as a function of frequency, composition, and temperature. *Physical Review B* 1999, 60, 12746.
- [15] Lafosse, X., Percolation and dielectric relaxation in polypyrrole-Teflon alloys. *Synthetic metals* 1995, 68, 227-231.
- [16] Ramdeen, F.; Hill, R., Scaling in the Region of the Percolation Threshold. *physica status solidi (b)* 1999, 213, 391-395.
- [17] Cai, W.; Li, M.; Wang, S.; Gu, Y.; Li, Q.; Zhang, Z., Strong, flexible and thermal-resistant CNT/polyarylacetylene nanocomposite films. *Rsc Adv* 2016, 6, 4077-4084.
- [18] Wu, T.; Chen, B., Autonomous self-healing multiwalled carbon nanotube nanocomposites with piezoresistive effect. *Rsc Adv* 2017, 7, 20422-20429.
- [19] Tsonos, C.; Soin, N.; Tomara, G.; Yang, B.; Psarras, G. C.; Kanapitsas, A.; Siores, E., Electromagnetic wave absorption properties of ternary poly (vinylidene fluoride)/magnetite nanocomposites with carbon nanotubes and graphene. *Rsc Adv* 2016, 6, 1919-1924.
- [20] Kaur, T.; Thirugnanam, A., Tailoring in vitro biological and mechanical properties of polyvinyl alcohol reinforced with threshold carbon nanotube concentration for improved cellular response. *Rsc Adv* 2016, 6, 39982-39992.
- [21] Marroquin, J. B.; Rhee, K.; Park, S., Chitosan nanocomposite films: enhanced electrical conductivity, thermal stability, and mechanical properties. *Carbohydrate polymers* 2013, 92, 1783-1791.
- [22] Tzounis, L.; Liebscher, M.; Tzounis, A.; Petinakis, E.; Paipetis, A.; Mäder, E.; Stamm, M., CNT-grafted glass fibers as a smart tool for epoxy cure monitoring, UV-sensing and thermal energy harvesting in model composites. *Rsc Adv* 2016, 6, 55514-55525.
- [23] Rostami, A.; Nazockdast, H.; Karimi, M., Graphene induced microstructural changes of PLA/MWCNT biodegradable nanocomposites: rheological, morphological, thermal and electrical properties. *Rsc Adv* 2016, 6, 49747-49759.
- [24] Zare, Y.; Garmabi, H.; Rhee, K. Y., Structural and phase separation characterization of poly (lactic acid)/poly (ethylene oxide)/carbon nanotube nanocomposites by rheological examinations. *Composites Part B: Engineering* 2018, 144, 1-10.
- [25] Zare, Y.; Rhee, K. Y., Prediction of tensile modulus in polymer nanocomposites containing carbon nanotubes (CNT) above percolation threshold by modification of conventional model. *Current Applied Physics* 2017, 17, 873-879.
- [26] Zhu, J.-M.; Zare, Y.; Rhee, K. Y., Analysis of the roles of interphase, waviness and agglomeration of CNT in the electrical conductivity and tensile modulus of polymer/CNT nanocomposites by theoretical approaches. *Colloids and Surfaces A: Physicochemical and Engineering Aspects* 2018, 539, 29-36.
- [27] Al-Saleh, M. H., Influence of conductive network structure on the EMI shielding and electrical percolation of carbon nanotube/polymer nanocomposites. *Synthetic Metals* 2015, 205, 78-84.
- [28] Logakis, E.; Pissis, P.; Pospiech, D.; Korwitz, A.; Krause, B.; Reuter, U.; Pötschke, P., Low electrical percolation threshold in poly (ethylene terephthalate)/multi-walled carbon nanotube nanocomposites. *Eur Polym J* 2010, 46, 928-936.
- [29] Li, H.-x.; Zare, Y.; Rhee, K. Y., The percolation threshold for tensile strength of polymer/CNT nanocomposites assuming filler network and interphase regions. *Materials Chemistry and Physics* 2018, 207, 76-83.
- [30] Razavi, R.; Zare, Y.; Rhee, K. Y., A model for tensile strength of polymer/carbon nanotubes nanocomposites assuming the percolation of interphase regions. *Colloids and Surfaces A: Physicochemical and Engineering Aspects* 2018, 538, 148-154.
- [31] Martin-Gallego, M.; Bernal, M.; Hernandez, M.; Verdejo, R.; López-Manchado, M. A., Comparison of filler percolation and mechanical properties in graphene and carbon nanotubes filled epoxy nanocomposites. *Eur Polym J* 2013, 49, 1347-1353.
- [32] Zare, Y.; Rhee, K. Y., Development of a conventional model to predict the electrical conductivity of polymer/carbon nanotubes nanocomposites by interphase, waviness and contact effects. *Composites Part A: Applied Science and Manufacturing* 2017, 100, 305-312.
- [33] Zare, Y.; Rhee, K. Y., Development of a model for electrical conductivity of polymer/graphene nanocomposites assuming interphase and tunneling regions in conductive networks. *Industrial & Engineering Chemistry Research* 2017, 56, 9107-9115.
- [34] Zare, Y.; Rhee, K. Y., Development and modification of conventional Ouali model for tensile modulus of polymer/carbon nanotubes nanocomposites assuming the roles of dispersed and networked nanoparticles and surrounding interphases. *Journal of colloid and interface science* 2017, 506, 283-290.
- [35] Almagableh, A.; Mantena, R.; Alostaz, A.; Rababah, M.; Aljarrah, M.; Awad, A. S., Modeling the elastic modulus of exfoliated graphite platelets filled vinyl ester: analytical predictions with consideration of filler percolation. *Journal of Composite Materials* 2015, 49, 1285-1290.

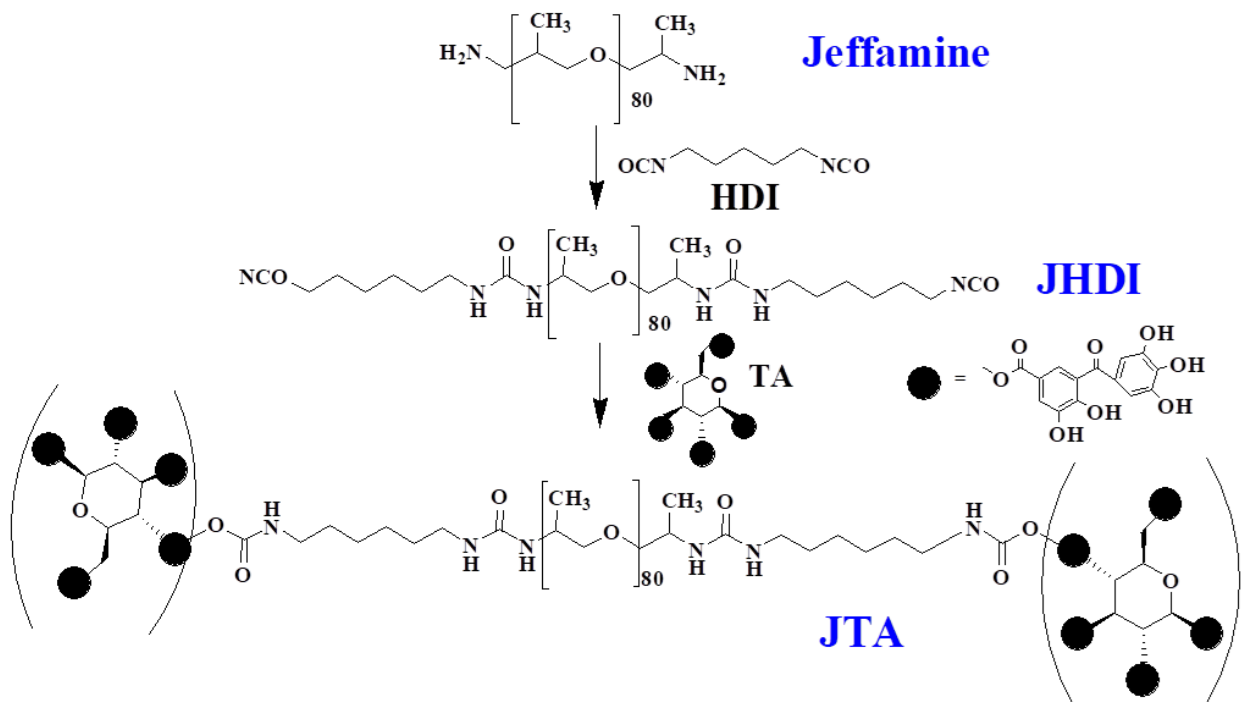
- [36] Kim, J. Y.; Park, H. S.; Kim, S. H., Multiwall-carbon-nanotube-reinforced poly (ethylene terephthalate) nanocomposites by melt compounding. *Journal of applied polymer science* 2007, 103, 1450-1457.
- [37] Heller, D. A.; Barone, P. W.; Swanson, J. P.; Mayrhofer, R. M.; Strano, M. S., Using Raman spectroscopy to elucidate the aggregation state of single-walled carbon nanotubes. *The Journal of Physical Chemistry B* 2004, 108, 6905-6909.
- [38] Bergman, S. D.; Wudl, F., Mendable polymers. *J Mater Chem* 2008, 18, 41-62.
- [39] Du, P.; Wu, M.; Liu, X.; Zheng, Z.; Wang, X.; Sun, P.; Joncheray, T.; Zhang, Y., Synthesis of linear polyurethane bearing pendant furan and cross-linked healable polyurethane containing Diels–Alder bonds. *New Journal of Chemistry* 2014, 38, 770-776.
- [40] Thostenson, E. T.; Chou, T. W., Carbon nanotube networks: Sensing of distributed strain and damage for life prediction and self healing. *Adv Mater* 2006, 18, 2837-3841.
- [41] Tee, B. C.; Wang, C.; Allen, R.; Bao, Z., An electrically and mechanically self-healing composite with pressure- and flexion-sensitive properties for electronic skin applications. *Nat Nanotechnol* 2012, 7, 825-832.
- [42] Benight, S. J.; Wang, C.; Tok, J. B. H.; Bao, Z. A., Stretchable and self-healing polymers and devices for electronic skin. *Prog Polym Sci* 2013, 38, 1961-1977.
- [43] Gao, Y.; Fang, X.; Tan, J.; Lu, T.; Pan, L.; Xuan, F., Highly sensitive strain sensors based on fragmented carbon nanotube/polydimethylsiloxane composites. *Nanotechnology* 2018, 29, 235501.
- [44] Yang, H.; Yao, X.; Yuan, L.; Gong, L.; Liu, Y., Strain-sensitive electrical conductivity of carbon nanotube-graphene-filled rubber composites under cyclic loading. *Nanoscale* 2019, 11, 578-586.
- [45] Cai, L.; Song, L.; Luan, P.; Zhang, Q.; Zhang, N.; Gao, Q.; Zhao, D.; Zhang, X.; Tu, M.; Yang, F.; Zhou, W.; Fan, Q.; Luo, J.; Zhou, W.; Ajayan, P. M.; Xie, S., Super-stretchable, transparent carbon nanotube-based capacitive strain sensors for human motion detection. *Sci Rep* 2013, 3, 3048.
- [46] Zhao, S. F.; Li, J. H.; Cao, D. X.; Gao, Y. J.; Huang, W. P.; Zhang, G. P.; Sun, R.; Wong, C. P., Percolation threshold-inspired design of hierarchical multiscale hybrid architectures based on carbon nanotubes and silver nanoparticles for stretchable and printable electronics. *Journal of Materials Chemistry C* 2016, 4, 6666-6674.
- [47] Mai, H.; Mutlu, R.; Tawk, C.; Alici, G.; Sencadas, V., Ultra-stretchable MWCNT–Ecoflex piezoresistive sensors for human motion detection applications. *Composites Science and Technology* 2019, 173, 118-124.
- [48] Liu, H.; Li, Y.; Dai, K.; Zheng, G.; Liu, C.; Shen, C.; Yan, X.; Guo, J.; Guo, Z., Electrically conductive thermoplastic elastomer nanocomposites at ultralow graphene loading levels for strain sensor applications. *Journal of Materials Chemistry C* 2016, 4, 157-166.
- [49] Liu, W. C.; Chung, C. H.; Hong, J. L., Highly Stretchable, Self-Healable Elastomers from Hydrogen-Bonded Interpolymer Complex (HIPC) and Their Use as Sensitive, Stable Electric Skin. *Acs Omega* 2018, 3, 11368-11382.
- [50] Lin, D.; Xing, B., Tannic acid adsorption and its role for stabilizing carbon nanotube suspensions. *Environ Sci Technol* 2008, 42, 5917-5923.
- [51] Zhang, X.; Liu, M.; Zhang, X.; Deng, F.; Zhou, C.; Hui, J.; Liu, W.; Wei, Y., Interaction of tannic acid with carbon nanotubes: enhancement of dispersibility and biocompatibility. *Toxicology Research* 2015, 4, 160-168.
- [52] San Biagio, P.; Bulone, D.; Emanuele, A.; Palma, M., Self-assembly of biopolymeric structures below the threshold of random cross-link percolation. *Biophysical journal* 1996, 70, 494-499.
- [53] Ezquerra, T. A.; Kuleszcza, M.; Cruz, C. S.; Baltá-Calleja, F. J., Charge transport in polyethylene–graphite composite materials. *Adv Mater* 1990, 2, 597-600.
- [54] Chen, S.; Sarafbidabad, M.; Zare, Y.; Rhee, K. Y., Estimation of the tensile modulus of polymer carbon nanotube nanocomposites containing filler networks and interphase regions by development of the Kolarik model. *Rsc Adv* 2018, 8, 23825-23834.
- [55] Kilbride, B. e.; Coleman, J.; Fraysse, J.; Fournet, P.; Cadek, M.; Drury, A.; Hutzler, S.; Roth, S.; Blau, W., Experimental observation of scaling laws for alternating current and direct current conductivity in polymer-carbon nanotube composite thin films. *Journal of applied physics* 2002, 92, 4024-4030.
- [56] Chen, X., Modeling of experimental adsorption isotherm data. *Information* 2015, 6, 14-22.
- [57] Chang, M.-Y.; Juang, R.-S., Adsorption of tannic acid, humic acid, and dyes from water using the composite of chitosan and activated clay. *Journal of Colloid and Interface Science* 2004, 278, 18-25.
- [58] Xing, B.; Pignatello, J. J., Dual-mode sorption of low-polarity compounds in glassy poly (vinyl chloride) and soil organic matter. *Environ Sci Technol* 1997, 31, 792-799.
- [59] Filletter, T.; Bernal, R.; Li, S.; Espinosa, H. D., Ultrahigh strength and stiffness in cross-linked hierarchical carbon nanotube bundles. *Adv Mater* 2011, 23, 2855-2860.
- [60] Nan, C.-W.; Shen, Y.; Ma, J., Physical properties of composites near percolation. *Annual Review of Materials Research* 2010, 40, 131-151.
- [61] De Vivo, B.; Lamberti, P.; Spinelli, G.; Tucci, V., A morphological and structural approach to evaluate the electromagnetic performances of composites based on random networks of carbon nanotubes. *Journal of Applied Physics* 2014, 115, 154311.
- [62] Connor, M. T.; Roy, S.; Ezquerra, T. A.; Calleja, F. J. B., Broadband ac conductivity of conductor-polymer composites. *Physical Review B* 1998, 57, 2286.
- [63] Mdarhri, A.; Carmona, F.; Brosseau, C.; Delhaes, P., Direct current electrical and microwave properties of polymer-multiwalled carbon nanotubes composites. *Journal of applied physics* 2008, 103, 054303.

ANNEXURE: SUPPORTING INFORMATION

1) Scheme



SCHEME 1. The complexation of JTA and MWCNT to form JCTx composites and the potential interactions between JTA and MWCNT.



SCHEME 2. Synthesis of JHDI precursor and TA-terminated JTA

2) Supplementary Figures:

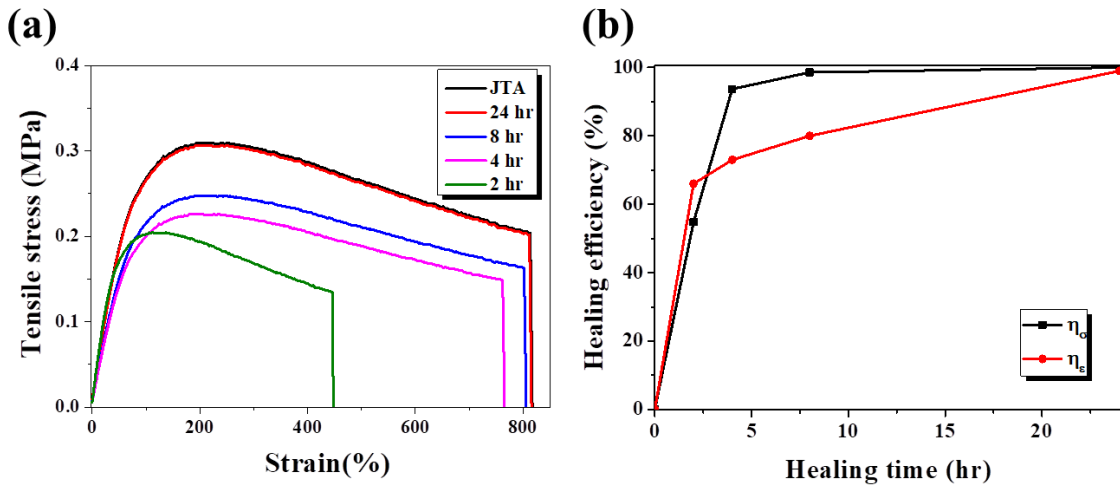


FIGURE S1. (a) Stress-strain curves and (b) the stress η_{σ} and strain η_{ϵ} healing efficiencies of the pristine and the healed JTA after different time of autonomous recovery.

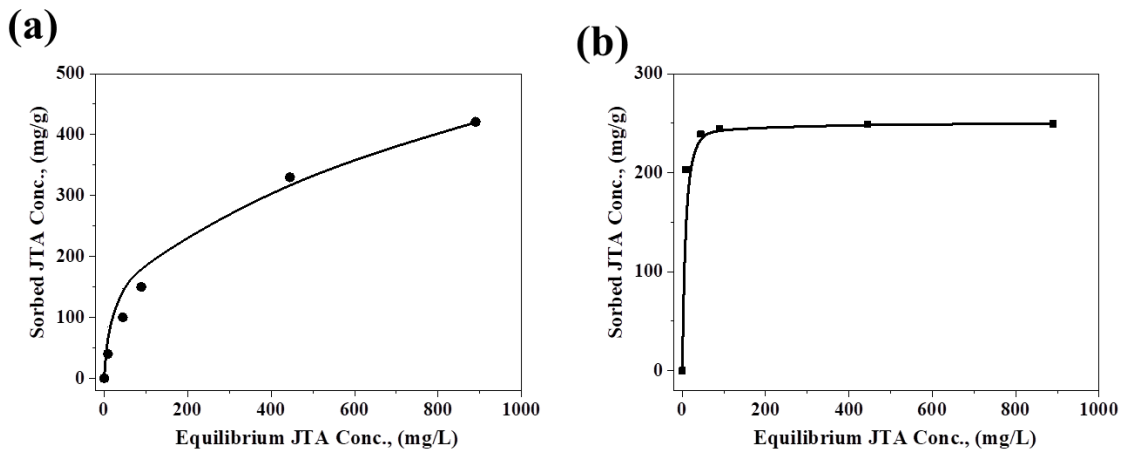


FIGURE S2. Model fits to the sorption data of JTA by carbon nanotubes (CNTs) by (a) Freundlich (FM) and (b) Dual-Langmuir (DLM) models.

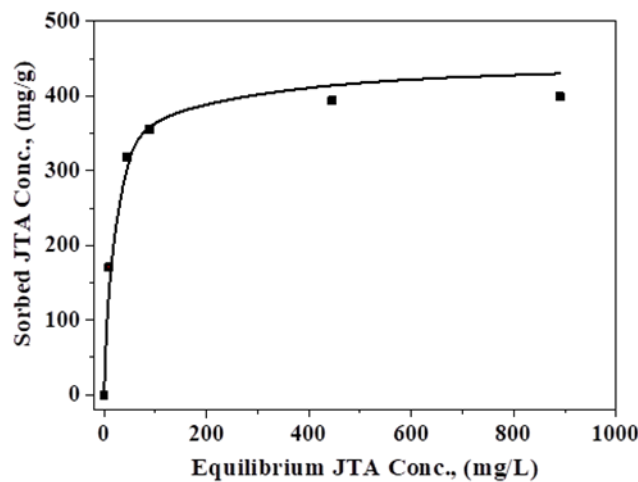


FIGURE S3. Model fits to the sorption data of JTA by carbon nanotubes (CNTs) by Langmuir model (LM).

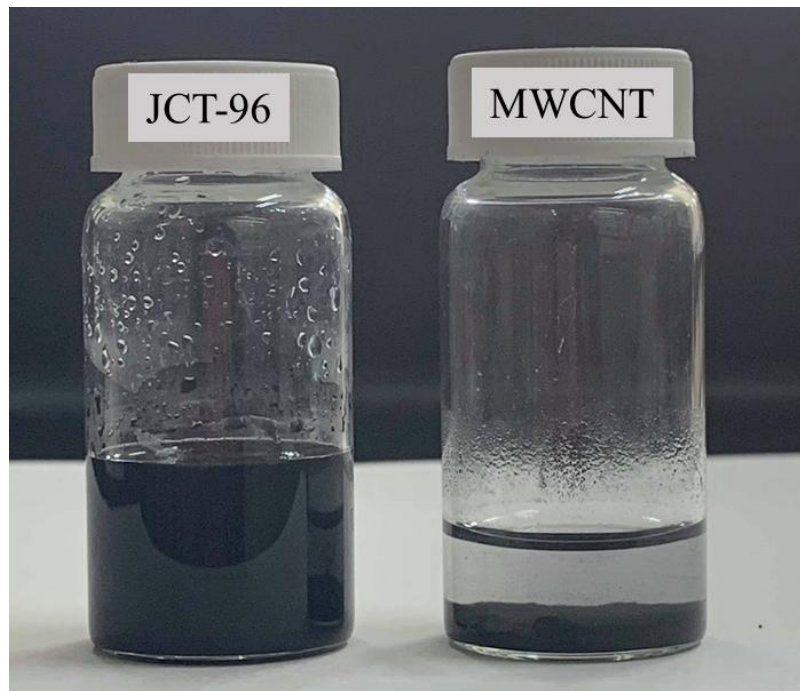


FIGURE S4. (a) Photo of JCT96/DMF (96 mg MWCNT/4 mg JTA /2 mL, left) MWCNT/DMF (100 mg/2 mL, right) solutions after settling for 30 days.

3) Supplementary Tables:

TABLE S1
MODEL EQUATION AND PARAMETER DEFINITION FITS TO SORPTION DATA

Langmuir model	$q_e = Q^0 b C_e / (1 + b C_e)$							
CNT	Q^0	p of Q^0	b	p of b				
MWCNT20	166	< 0.01	0.082	0.015				
Freundlich model	$q_e = K_f C_e^{1/n}$							
CNT	K_f	p of K_f	n	p of N				
MWCNT20	39	< 0.01	2.840	< 0.01				
Dual-model model	$q_e = Q^0 b C_e / (1 + b C_e) + K_d C_e$							
CNT	Q^0	p of Q^0	b	p of b	K_d	p of K_d		
MWCNT20	105	< 0.01	0.405	< 0.01	0.205	< 0.01		
Dual-langmuir model	$q_e = Q_1^0 b_1 C_e / (1 + b_1 C_e) + Q_2^0 b_2 C_e / (1 + b_2 C_e)$							
CNT	Q_1^0	p of Q_1^0	b_1	p of b_1	Q_2^0	p of Q_2^0	b_2	p of b_2
MWCNT20	99	< 0.01	0.486	< 0.01	307000	1	0.000	1.00

* q_e (mg/g) is equilibrium sorbed concentration; C_e (mg/L) is equilibrium solution phase concentration. Q^0 (mg/g) is the maximum monolayer adsorption capacity. b constant is related to the molar heat of adsorption. K_d (L/g) is partition coefficient

TABLE S2
EXPERIMENTAL AND THEORETICAL MODULI ES OF JCTx (X FROM 10 TO 40) AND THE PARAMETERS INVOLVED IN EQUATION (1).

	Experimental E (MPa)	Calculated ^a E (MPa)	Density ^b D (g/ml)	Volume fraction ^c ϕ_f (%)	Mass fraction p (%)	Parameter f^d
JTA	0.3	----	1.17	-----	----	-----
JCT10	1.15	0.69	1.20	0.08	0.1	0.17
JCT15	1.73	0.94	1.21	0.12	0.15	0.21
JCT20	2.01	1.52	1.24	0.16	0.2	0.25
JCT25	2.98	3.02	1.25	0.21	0.25	0.29
JCT30	3.9	5.07	1.27	0.25	0.3	0.33
JCT35	7.54	9.03	1.29	0.30	0.35	0.36
JCT40	13.5	13.5	1.30	0.34	0.4	0.39

^a modulus E was calculated from eqn (1) based on a E_f of 85.6 Mpa formulated from fitting modulus of JCT40 into eqn (1). calculated the tensile modulus of composites with co-continuous morphology.

^b densities of JTA was determined from the buoyancy method, by which JTA was placed in gradient of liquids of known density to approach the density. And the density of composites JCTx were from: $D=DJTA\rho_{JTA}+DCNT\rho_{CNT}$, where DCNT and DJTA are densities of MWCNT and JTA, respectively and PCNT and PJTA are mass fraction of MWCNT and JTA, respectively.

^c Volume fraction = $(WCNT/DCNT)/(WCNT/DCNT+WJTA/DJTA)$, where WCNT and WJTA are weights of MWCNT and JTA.

TABLE S3
EXPERIMENTAL AND THEORETICAL CONDUCTIVITIES OF JCTx (X FROM 1 TO 96) AND THE RELATED PARAMETERS USED IN FITTING EQN (4).

	Resistivity ($\Omega.m$)	Conductivity σ ($S.m^{-1}$)	$\ln\sigma$	volumn fraction ϕ_f (%)	$\ln\phi_f$
JTA	----	-----	-----	----	-----
JCT1	8.33×10^2	1.2×10^{-3}	-2.92	0.008	-4.76
JCT10	1.4×10^1	7.14×10^{-2}	-1.15	0.083	-2.49
JCT20	1.02	9.84×10^{-1}	-0.01	0.162	-1.82
JCT30	3.12×10^{-2}	3.2×10^1	1.51	0.236	-1.44
JCT40	1.53×10^{-3}	6.55×10^2	2.82	0.307	-1.18
JCT50	3.31×10^{-4}	3.02×10^3	3.48	0.375	-0.98
JCT60	1.10×10^{-4}	9.15×10^3	3.96	0.439	-0.82
JCT70	1.48×10^{-5}	6.76×10^4	4.83	0.499	-0.69
JCT80	2.89×10^{-6}	3.46×10^5	5.54	0.558	-0.58
JCT90	1.20×10^{-6}	8.31×10^5	5.91	0.613	-0.489
JCT96	8.26×10^{-7}	1.21×10^6	6.08	0.646	-0.44

Features of some interacting tropical cyclones in the Indian Ocean after the Mount Pinatubo eruption

Vladimir Kostin^{1*}, Gennady Belyaev², Olga Ovcharenko³, Elena Trushkina⁴

Institute of Terrestrial Magnetism, Ionosphere and Radio Wave Propagation of Russian Academy of Sciences, IZMIRAN, Moscow, Troitsk, Russia

Abstract— *The features of the impact of some tropical cyclones (TC) in the Indian Ocean on the environment after the eruption of Mount Pinatubo are considered. The 1992 North Indian Ocean cyclone season was unofficially the most active year on record for the basin, with 13 TC developing. It was shown that TC-05B, closing the chain of 10 TC before its destruction over the North Bay of Bengal, showed anomalous thunderstorm activity and contributed to the emergence of TC Aviona in South Indian Ocean. The strongest in season-92 TC-10B and TC Forrest, apparently, caused an earthquake in the Indian Ocean. At the same time, the strongest typhoons Hunt and Gay from 1979 to 2015 simultaneously developing in the Pacific Ocean caused the Burma Plate earthquake. Experimental data of anomalous features of the ionosphere during these events were obtained using the satellite Cosmos-1809.*

Keywords— *Indian Ocean, Tropical Cyclone, Pinatubo.*

I. INTRODUCTION

The problem of the movement of several interacting tropical cyclones and their impact on the environment is complex. It was previously shown that two tropical cyclones, at a distance of less than 1,400 km from one another, begin to rotate around a common center and converge [1]. Currently, meteorology typically uses a modified ETA model: North American Mesoscale Forecast System (NAM) [2] or Weather Research and Forecast Model (WAR) [3] to predict the development of tropical cyclones. Manipulating the vast datasets and performing the complex calculations necessary to modern numerical weather prediction requires some of the most powerful supercomputers in the world. Examples of such calculations and detailed references are presented in the series of works by the authors [4].

Further studies showed that the nonlinear dynamics of internal gravity wave (IGW) structures of the dissipative ionosphere in the presence of a heterogeneous zonal wind can create both monopole vortices in the form of a tropical cyclone and a vortex path along the zonal wind [5, 6]. IGW can occur both in multiple lightning discharges and in the structures of a developed tropical cyclone [7-9]. The flow of atmospheric air over obstacles such as islands or isolated mountains sometimes gives birth to von Karman vortex streets [10]. The significant role of the structure of the lower stratosphere in the development of a tropical cyclone was noted in [11] and in separate sections of the annual reports of the Joint Typhoon Warning Center (JTWC) by J.C. Sadler. The structure of the equatorial stratosphere is associated with the development phase of the quasi-biennial oscillation (QBO) [12, 13].

Analysis conducted by the authors according to the Cosmos-1809 satellite showed that a month after the eruption of Mount Pinatubo 12-Jun-91 [14], the plasma density of the upper ionosphere near the equator decreased approximately two times, and a continuous sequence of typhoons was observed in the western Pacific [15, 16].

In 1992, the cyclonic activity of the world's oceans, characterized by the Accumulated Cyclone Energy (ACE) index, increased by 50% [15]. TCs achieved the highest activity in September-November 92, when up to 10 TCs simultaneously developed. At this time the eastern phase of QBO was observed in the lower stratosphere [12]. IGW acoustic effects from numerous strong aftershocks of the Landers-92 earthquake and from underground nuclear tests (UNT) on the Nevada Test Site (NTS) on the atmosphere contributed to the development of a chain of interacting TCs in accordance with the theoretical conclusions of Aburjania [16-18].

One of the authors' research results was the detection of the dependence of the earthquake occurrence during the intensification of TCs of the fifth category: Andrew (August), Bonnie and Charley (September) in the Atlantic Ocean, and Gay and Hunt (November) in the Pacific Ocean. Earthquakes occurred on the southern border of the American Plate in the South Sandwich Islands on August 24 ($M = 6.1$), September 24 ($M = 5.5$ and 5.6) and November 21 ($M = 6.6$) (Table 1). A possible mechanism for the occurrence of earthquakes is associated with the raising of tectonic plates in the zone of the "eye" of TC and lowering the opposite edge of the plate, what is suggested in the presentation of the report [18].

The effects of the development of the Indian Ocean TCs in 1992, interacting with Pacific typhoons in the eastern wind phase of the lower stratosphere are considered in this paper as well as individual earthquakes, the occurrence of which may be associated with TC 10B and Forrest impact on the Indian Plate.

II. FEATURES OF THE HIGH IONOSPHERE OVER THE INDIAN OCEAN 24-SEP-92

In the middle of September, 92 tropical cyclones were observed only in the Pacific Ocean and nowhere more [19]. The names of these tropical cyclones were Typhoon Ted and Hurricane Roslin. September 17, before the autumnal equinox when the eastern zonal wind occurred in the lower stratosphere three Tropical Depression (TD) Bonnie, Seymour and Tina were formed near the American continent [11]. Bonnie formation was associated with a deep invasion of a cold front along the east coast of America. Tropical waves after crossing the Americas were upgraded into TD Seymour and Tina. TD Seymour reached hurricane strength on the 19th. TD Tina was alive from September 17 to October 11. This is the record for the eastern Pacific Ocean.

The further development of TCs is in good agreement with the ideas of Aburjania [5, 6] about the formation of the Rossby-Aburjania wave from the TC chain diverging from the San Andreas Fault. The additional acoustic impact from the nuclear test experiment (NTE) Hunter Trophy on September 18 led to an increase of Bonnie, Seymour, Tina and Ted intensity, as well as to the organization of TC Val in the western Pacific Ocean. September 21, with further self-organization of the Rossby-Aburjania wave TC Charley and Danielle arose in the Atlantic Ocean to the east of the San Andres fault, and TC 05B appeared in Indian Ocean on the other side of the wave. Fig. 1 shows the dynamics of the TC development in the Indian Ocean and the western Pacific Ocean. Moments of the NTE are marked by arrows in Fig. 1.

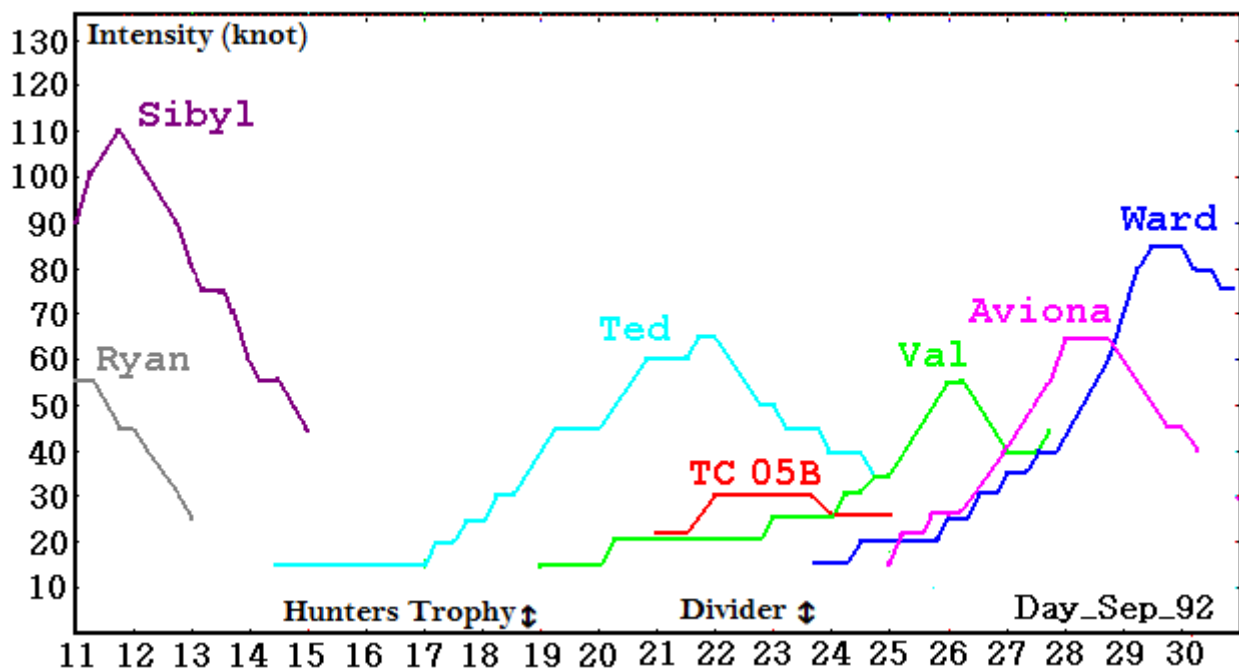


FIGURE 1. Dynamics of TCs in the western Pacific and Indian Oceans in September 1992.

After the next NTE Divider held on September 23, the trajectories of five tropical cyclones in eastern Pacific and Atlantic oceans changed dramatically, TC 05B and typhoon Ted dissipated, and a new TC Ward was born in the western Pacific [18]. TC 05B moved westward over the northern Bay of Bengal. It hit near the Indian/Bangladesh coastline on the 23rd as a depression, and dissipated 2 days later over India [19]. The India Meteorological Department report does not contain information on TC 05B [20].

Cosmos-1809 satellite measurements 24-Sep-92 revealed an abnormally large thunderstorm activity over India and the emergence of a new TC Aviona in the South Indian Ocean. The satellite had an altitude of about 960 km, a period of ~ 104.1 min, an inclination of $\sim 82^\circ$, a shift in the next orbit in longitude of $\sim 26.1^\circ$, and a change in local time of ~ 36 sec. Satellite in the passive mode measured: electron density N_e and its fluctuation dN_e , electron temperature T_e , two components of a large-scale electric field, amplitudes of electromagnetic plasma oscillations in frequency channels $f = 140, 450, 850, 4600$ Hz

and 15 kHz with a width $\Delta f = f / 8$. All this made it possible, by comparing the measurement data at neighboring orbits, to determine local and global sources of ionosphere disturbances.

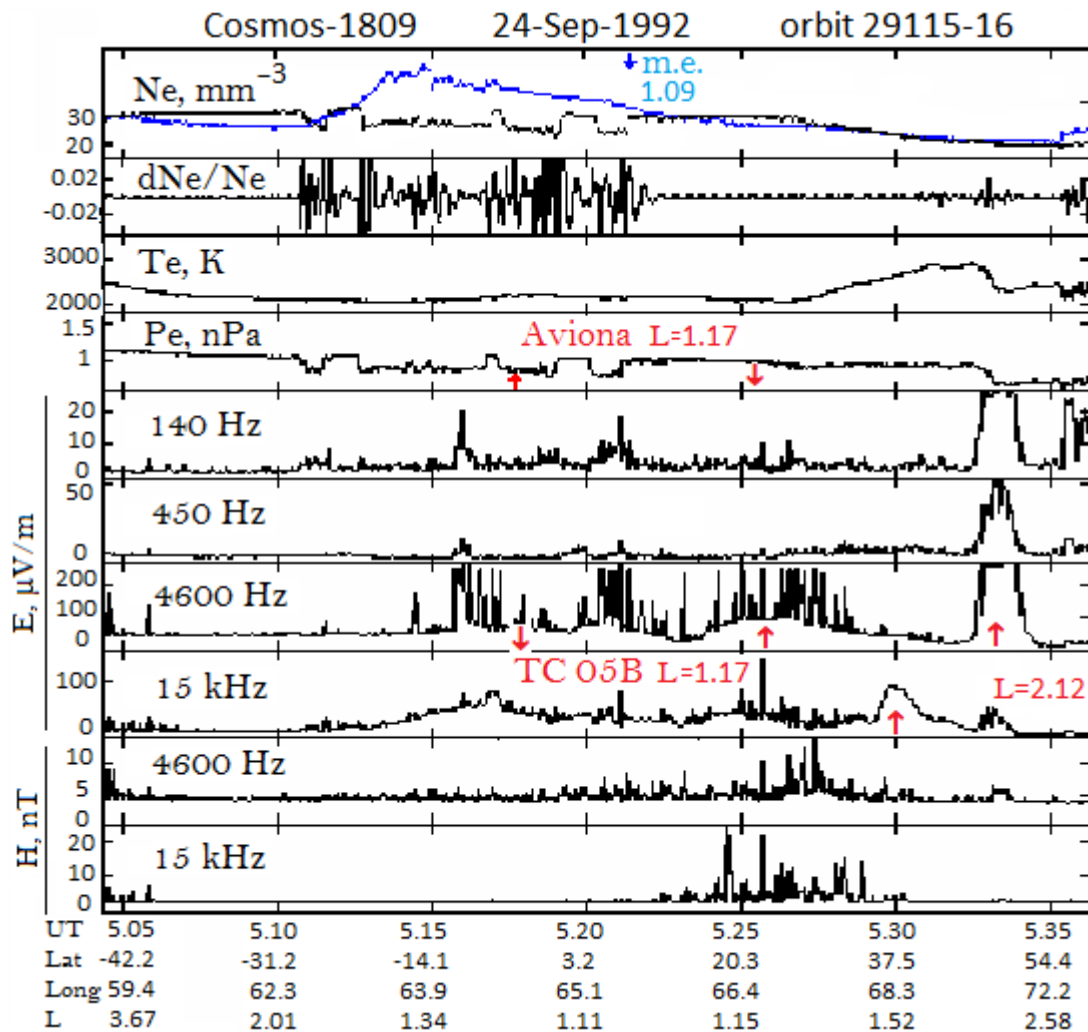


FIGURE 2. Cosmos-1809 measurement data in the morning sector ($LT \approx 10$) west of the Indian peninsula and near the Aviona TC origin center (73 E, 5 S).

In Fig. 2, the satellite's passage through the latitude of the TC 05B center (21.7 N, 89.0 E) is marked on the E4600 panel with the up arrow and the same path in the magnetically conjugated region ($L = 1.17$) is indicated by the down arrow. Narrow peaks in the channels of 4600 Hz register the magnetosphere passage of whistles from lightning discharges. The maximum intensity of these signals is located near the lower hybrid frequency (LHR), which is usually located in the channel band of 4600 Hz. The magnetosphere passage of VLF signals from the VLF transmitters was studied jointly with the Cosmos-1809 and DE-1 satellites [21]. Usually, signals in the whistle mode deviate from the magnetic field from the region of entry into the ionosphere to the caustic with large L – shells. And if a duct is formed along a magnetic field with a lower density, then the signal is captured. Above the TC 05B (the zone of whistlers entering the ionosphere), both electric and magnetic components were observed. When the whistle propagates beyond the magnetic equator (indicated by a blue down arrow in Fig. 2), it has only the E component near the LHR, which is perpendicular to the magnetic field. September 24, the high density of whistling signals was observed only at this orbit. At the previous orbit passing between TC 05B and Ted only ascending whistlers were observed and the density was 2-3 times less.

The appearance of individual Ne cavities with dNe fluctuations of up to 4–5% over the incipient TC at the stage of amplification of the tropical disturbance (TD) was observed from the Cosmos-1809 satellite in several cases [8]. However, there are several such caverns south of the magnetic equator and above TD Aviona. They are filled with descending whistlers that displaced part of the plasma to the east. The blue curve on the Ne panel shows the plasma density distribution along 29114-15 orbit on the same L-shells.

Additionally Fig. 2 shows the electron gas pressure $P_e = N_e k T_e$, where k is the Boltzmann constant (panel No. 4). The equilibrium of P_e in the cavities is established due to the interaction of electrons with developed Langmuir turbulence where N_e fluctuations reach 4% (panel No. 2). At 5:33 UT, the satellite entered the region of strong oscillations in the vicinity of the LHR (channel 4600 Hz) near the cyclotron frequency of hydrogen (channel 450 Hz) and the cyclotron frequency of helium (channel 140 Hz). Sharp decrease in P_e also occurs here. This region is associated with a traveling ionospheric disturbance (TID) from an earthquake in Iran (29.8 N, 51.1 E; $M = 5.1$) September 23 at about 22 UT. The development of disturbances in the ionosphere in the low-frequency range was considered in detail by M. Hayakawa [22]. The Cosmos-1809 satellite recorded the dynamics of similar disturbances from the acoustic effects of underground nuclear explosions [23].

It should be noted that at 5:30 UT a strong signal only in the 15 kHz channel is associated with the satellite passing over the zone of influence of one of the Radio Engineering Navigation Range finder (RSDN-20; 39.5 N, 62.7 E) transmitters on the ionosphere, one of whose frequencies $f = 14.88$ kHz falls into the channel band. The Russian RSDN-20 stations are nicknamed ALPHA.

The features discussed in this section did not stand out after 11 hours on orbit 29122, passing in the unlit ionosphere along the west coast of India.

III. TC 10B AND FORREST ENVIRONMENTAL EFFECTS

In autumn 1992 El Niño-Southern oscillation is formed in the Pacific Ocean. In November, a short-term anomaly of the east wind arose in the lower stratosphere [12]. In this period the strongest TCs are observed which are shown in Fig. 3. Intensity and trajectory of movement of the TCs show that:

1. TC Forrest and TC 10B interacted under the influence of the monsoon on November 12-16.
2. Typhoons Gay, Hant and Forrest interacted on November 16-22.

Only one (TC10B of November 11-17) of the 12 cyclones formed over the North Indian Ocean affected the weather over Indian peninsula [20]. Under the influence of this weather system, wide spread very heavy rainfall occurred in the coastal districts of Tamilnadu and Kerala. Forrest was the only TC of 1992 to track from the western North Pacific, across the South China Sea, and into the Bay of Bengal. It reached a maximum intensity of 125 kt (230 km/h) in the Bay of Bengal over a day after it had recurved. Hunt was part of a three storm outbreak with Forrest and Gay. As Hunt intensified, it brushed by Guam, moved into the Philippine Sea, and later recurved. After recurvature, the typhoon played an important role in the extremely rapid weakening of Gay which was approaching the southern Mariana Islands. Typhoon Gay was the most intense TC since Typhoon Tip in 1979 to Hurricane Patricia in 2015. JTWC estimated its peak winds of 295 km/h (160 knot) and a minimum barometric pressure of 872 mb [19].

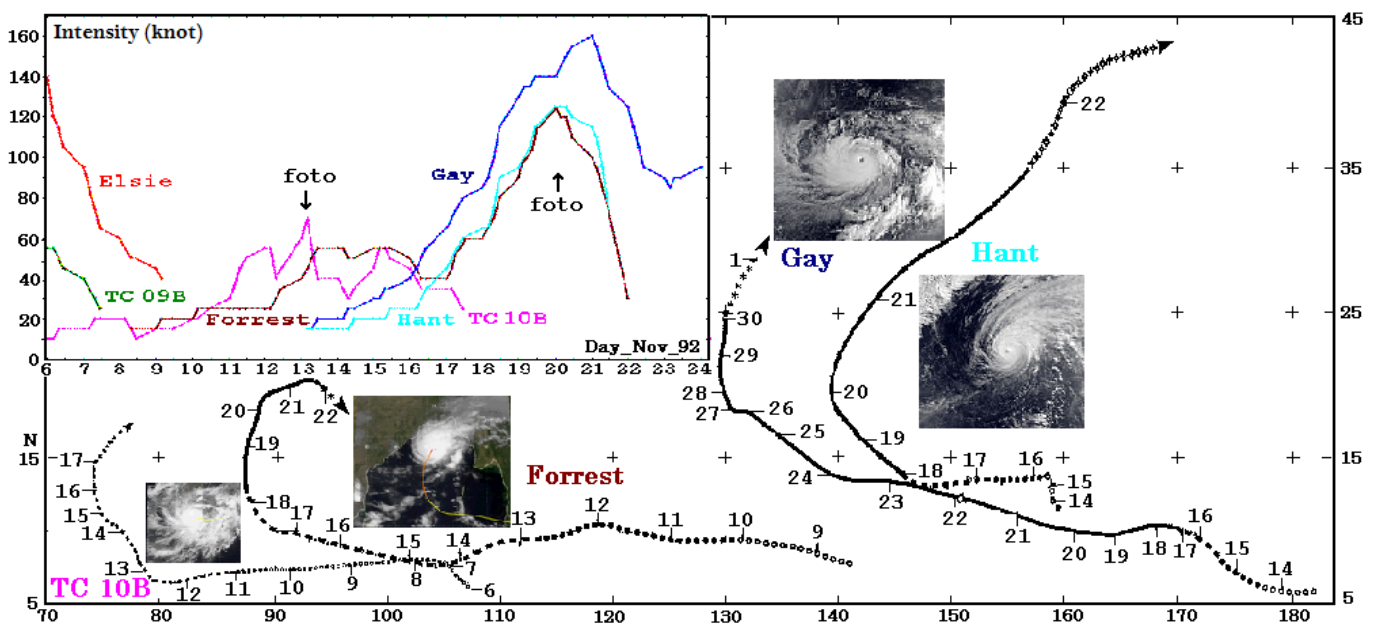


FIGURE 3. Trajectories and intensity of tropical cyclones in November 1992.

Two maps are shown in Fig. 4 on which measurements of the amplitude of the electric (green curve) and magnetic (blue) components of the plasma oscillations obtained from the Cosmos-1809 satellite in the frequency channels of 4600 Hz in the morning sector on November 14 and 16 are plotted. The ordinate axis of the first curve on the left is aligned with the 123.4 E meridian, whose plane at the equator crosses the 29816 orbit at 21:33:22 UT 13-Nov. The subsequent curves are shifted by 26.1 in longitude and 104.1 minutes in time. Correspondingly, the ordinate axis is aligned with the 84.0 E meridian, whose plane at the equator crosses orbit 29845 at 23:54:26 UT on November 15. Due to the inclination of the orbit the descending orbits at a latitude of 45 N pass of about 4.8 west of the longitude of the equator, and at a latitude of 45 S pass east of about 4.8. All curves are plotted in the same scale, which is shown at the top right.

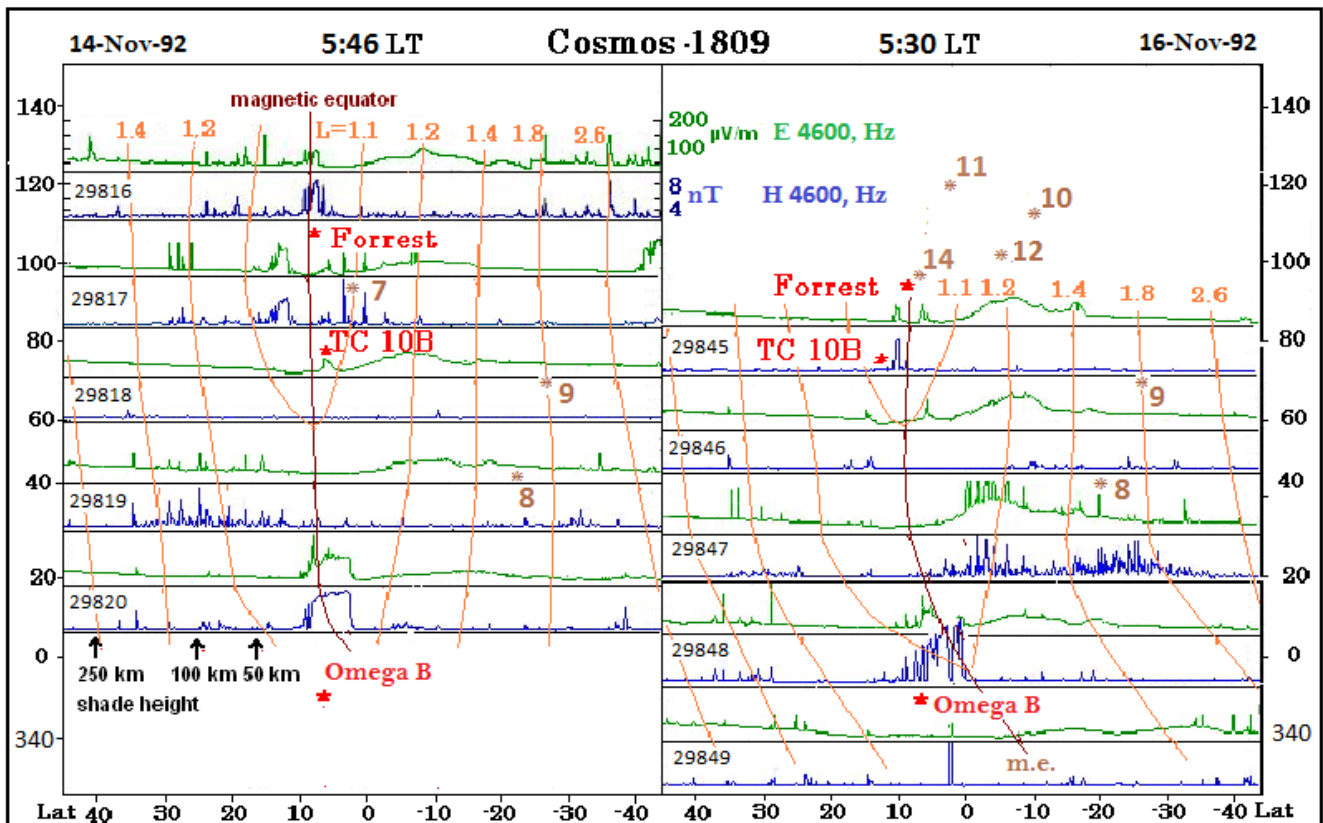


FIGURE 4. Measurement data of the amplitudes of the electric (green) and magnetic (blue) components of the plasma oscillations recorded in the frequency channels of 4600 Hz at 5 consecutive downward orbits. The horizontal axis of the E-component coincides with the longitude of the orbit at the equator. The brown stars with the number mark the centers of earthquakes from Table 1. The orange lines on the maps with the number at the top are the magnetic L-shells at the height of the satellite.

Cosmos-1809 satellite data at 4600 Hz channels most representatively illustrate, taking into account measurements by other instruments, the features of the upper ionosphere over powerful natural and technogenic sources [23]. A comparison of the signals on November 14 and 16 over Forrest, the intensity of which did not change, and the TC 10B indicates:

1. The intensity of plasma oscillations near LHR is highly dependent on the height of the solar shadow. On November 14, the shadow whose height below the satellite, shown in Fig. 4, November 16, shifted ~ 15 degrees latitude south. Therefore, in a less illuminated ionosphere, the signal is weaker.
2. The strong electric and magnetic component in orbit 29816 which passed 15 degrees east of Forrest, is associated with LHR excitation in the perturbed ionosphere above the TC similarly to the situation considered in [8]. In orbit 29817 which passed 18 degrees to the east from the TC 10B which was located 2 degrees south of the magnetic equator a stronger LHR perturbation was observed in the magnetically conjugated ionosphere due to the action of the terminator. On orbit 29845 passing between Forrest and TC 10B the formation of a magnetosphere channel which contains e^-/m oscillations of the whistling mode and electrostatic oscillations in the conjugated ionosphere is observed. In orbit 29846 west of the TCs over the TIDs, which arose after the terminator passed over the TCs, a well-formed cavity was observed.

3. Two spaced peaks in orbit 29817 near the equator are associated with earthquake No. 7 of Table 1. Ten hours before the earthquake, the TC 10B increased to 70 kt into the Bay of Bengal, while Forrest increased to 55 kt into South China Sea. The combined impact of TCs on the Indian Plate and Philippine Plate was transmitted to the Burma Plate where an earthquake occurred in the southeast ledge under East Sameule, Sinabang. Exactly the same earthquake occurred 2-Nov (No. 6, Table 1) while TC 09B passing into the Bay of Bengal and Super Typhoone Elsie passing into South China Sea. These earthquakes did not have a pre-shock and aftershocks this indicates a sharp change in the impact on seismic plates.
4. Another TCs geometry was observed on November 22, when Forrest (85 kt) was in the north of the Bay of Bengal and Gay (to 145 kt) crossed the Marinas Trench and entered the Philippine Sea. The result was a deep earthquake in the middle of the eastern border of the Burma Plate (middle of the Nicobar Islands arc). Earlier on 16 November Forrest was near this fault but there was no earthquake.
5. On November 15, TC 10B into the Arabian Sea and Forrest into the Andaman Sea synchronously intensified to 55 kt (100 km / h) and an earthquake occurred in the Indian Ocean Triple Junction of 4.7 M_w .
6. On November 14, a satellite in orbit 29819 passed over the focal point of an earthquake in Madagascar. According to the entire set of satellite instruments, 3 hours before the earthquake, precursors stood out here, examples of which are considered in the monograph [22]. On November 16, after an earthquake in orbit 29847, a highly disturbed region stands out to the west of the earthquake source. Indonesian earthquakes under No. 10-12 in Table 1, the centers of which are indicated on the right half of Fig. 4 belong to the class of ordinary earthquakes.
7. The lower part of Fig. 4 shows the change in the ionosphere parameters depending on the position of the terminator above the Omega B transmitter, which effectively affects the E-layer of the ionosphere. Each Omega station transmitted a sequence of three very low frequency (VLF) signals (10.2 kHz, 13.6 kHz, 11.333... kHz in that order) plus a fourth frequency which was unique to each of the eight stations. The duration of each pulse (ranging from 0.9 to 1.2 seconds, with 0.2 second blank intervals between each pulse) differed in a fixed pattern, and repeated every ten seconds. These features are in good agreement with the parameters of the perturbed lower ionosphere from the occurrence of acoustic pulses during earthquakes and the development of the TC.

TABLE 1
SPECIFIC NUCLEAR TEST EXPERIMENTS AND EARTHQUAKES IN SEPTEMBER – NOVEMBER 1992.

No.	Date 1992	UT h : m	Epicenter N / E	M_w	Depth km	Area / Name
1	18-Sep	17:00	37.2 / -116.2	3.8	2.3	NTS / Hunters Trophy
2	23-Sep	15:04	37.0 / -116.0	4.2	1.83	Nevada Test Site / Divider
3	23-Sep	21:59	29.8 / 51.1	5.1	35.0	Southern Iran
4	24-Sep	00:52	-59.5 / -26.0	5.5	21.2	South Sandwich Islands region
5	24-Sep	21:49	9.8 / 92.8	4.3	72.9	Nicobar Islands, India region
6	02-Nov	01:41	2.1 / 95.7	4.7	33.0	Simeulue, Indonesia
7	13-Nov	16:01	2.4 / 96.3	5.3	33.0	Simeulue, Indonesia
8	14-Nov	05:55	-23.0 / 45.8	5.0	22.9	Madagascar
9	15-Nov	07:02	-26.2 / 70.9	4.7	10.0	Indian Ocean Triple Junction
10	15-Nov	15:57	-11.5 / 115.0	5.0	33.0	South of Bali, Indonesia
11	18-Nov	00:36	1.6 / 118.0	4.9	33.0	Kalimantan, Indonesia
12	18-Nov	21:26	-7.3 / 106.2	5.3	48.2	Java, Indonesia
13	21-Nov	22:40	-56.7 / -26.4	6.6	20.1	South Sandwich Islands region
14	22-Nov	07:48	7.1 / 94.1	4.5	96.1	Nicobar Islands, India region

IV. CONCLUSION

1. After the Pinatubo eruption, TC enhancement in the Indian Ocean correlated with the development of Pacific typhoons was observed with an east wind in the lower stratosphere.

2. The earthquakes in Simeulue, Indonesia were caused by the joint intensification of TCs into the Bay of Bengal and into South China Sea on November 02 and 13.
3. Earthquakes in Nicobar Islands, India region occurred after August 4, Super Hurricanes Janis and November 22 Gay crossed Marinas Trench and entered the Philippine Sea. Earthquakes in this area also occurred after intensification of the global TCs chain September 24 and intensification of TCs in the South Pacific Ocean and South Indian Ocean December 8, 10 and 27.
4. The earthquake in Indian Ocean Triple Junction November 15 occurred after the synchronous amplification of TC 10B into the Arabian Sea and Forrest into the Andaman Sea. According to the Centennial Earthquake Catalog, it was the only earthquake with $M_w > 2.5$ in the region during the period of November 11-22. It is assumed that it was associated with the rise of the Indian Plate in the zone of development of two TC and the lowering of the edge of the Indian Plate in a node with two adjacent plates.
5. Probably December 25, 2004, the intense tropical cyclone Chambo to 80 kt (150 km / h) in central South Indian Ocean lifted the southern edge of the Indian Plate. The eastern edge of the Indian Plate plummeted beneath the Burma Plate, the mega earthquake of 9.1 M_w and the Boxing Day Tsunami occurred. This situation requires further detailed consideration and refinement of the forecast of such events [24].

CONFLICT OF INTEREST STATEMENT

The authors declare that the research was conducted in the absence of any commercial or financial relationships that could be construed as a potential conflict.

ACKNOWLEDGEMENTS

Many thanks to our colleges at project of Cosmos-1809, especially to Ya.P. Sobolev[†] (IZMIRAN), who was working with Analyzer low frequency e/m fluctuations in the band of 20 Hz – 20 kHz device; to G.P. Komrakov (FGBNU RRI) – Impedance probe measurements for Ne and dNe device; to V.V. Afonin (IKI RAN) – Electron temperature measurements in the range of 600 – 5000 K device.

REFERENCES

- [1] S. Fujiwhara, "The natural tendency towards symmetry of motion and its application as a principle in meteorology," *Quart. J. Roy. Meteorol. Soc.*, vol. 47, pp. 287-292, October 1921.
- [2] <http://www.ncdc.noaa.gov/data-access/model-data/model-datasets/north-american-mesoscale-forecast-system-nam>.
- [3] <http://www.meteo.psu.edu/~wrf/rt/>.
- [4] A.E. Pokhil, E.S. Glebova and A.V. Smirnov, "Studying an interaction between tropical cyclones and jet streams using the numerical simulation data," *Russian meteorology and hydrology*, vol. 38, pp. 141-149, 2013.
- [5] G.D. Aburjania, "Self-localization of planetary wave structures in the ionosphere upon interaction with nonuniform geomagnetic field and zonal wind," *Izvestiya, Atmospheric and Oceanic Physics*, vol. 47 (4), pp. 533-546, 2011.
- [6] G.D. Aburjania, O.A. Kharshiladze and K.Z. Chargazia, "Self-organization of IGW structures in an inhomogeneous ionosphere: 2. Nonlinear vortex structures," *Geomagn. Aeron.*, vol. 53 (6), pp. 750-760, 2013.
- [7] R.L. Walterscheid, G. Schubert and D.G. Brinkman, "Acoustic waves in the upper mesosphere and lower thermosphere generated by deep tropical convection," *J. Geophys. Res.*, vol. 108 (A11), p. 1392, doi: 10.1029/2003JA010065, 2003.
- [8] V.M. Kostin, G.G. Belyaev, B. Boychev, E.P. Trushkina and O.Ya. Ovcharenko, "Ionospheric precursors of the intensification of isolated tropical cyclones according to the IKB-1300 and Cosmos-1809 satellite data," *Geomagn. Aeron.*, vol. 55 (2), pp. 246-260, doi: 10.1134/S0016793215020127, 2015.
- [9] G. Belyaev, B. Boychev, V. Kostin, E. Trushkina and O. Ovcharenko, "Modification of the ionosphere near the terminator due to the passage of a strong tropical cyclone through the large Island," *SunGeo*, vol. 10 (1), pp. 31-38, 2015.
- [10] D. Etling, "Mesoscale vortex shedding from large islands: A comparison with laboratory experiments of rotating stratified flows," *Meteorology and Atmospheric Physics*, vol. 43 (1), pp. 145-151, doi:10.1007/BF01028117, 1990.
- [11] J.C. Sadler, "A role of the Tropical Upper Tropospheric Trough in early season typhoon development," *Monthly weather review*, vol. 104, pp. 1266-1278, 1976.
- [12] A.S. Huesmann and M.H. Hitchman, "The stratospheric quasi-biennial oscillation in the NCEP reanalyses: Climatological structures," *J. Geophys. Res.*, vol. 106 (D11), pp. 11859-11874, 2001.
- [13] I.P. Gabis and O.A. Troshichev, "The quasi-biennial oscillation in the equatorial stratosphere: Seasonal regularity in zonal wind changes, Discrete QBO-cycle period and prediction of QBO-cycle duration," *Geomagn. Aeron.*, vol. 51 (4), pp. 501-512, 2011.

- [14] J. Hampson, C. Claud, P. Keckhut and A. Hauchecorne, "The dynamical influence of the Pinatubo eruption in the subtropical stratosphere," *J. Atm. Sol.- Terr. Phys.*, vol. 68 (14), pp. 1600-1608, 2006.
- [15] V.M. Kostin, G.G. Belyaev, O.Ya. Ovcharenko and E.P. Trushkina, "Influence of cyclones on the plasma parameters of the upper ionosphere in the two-year period after the Mounts Pinatubo and Hudson eruptions," *Astronomy-2018. Solar-Terrestrial physics – the current state and prospects*, Proceedings, vol. 2, pp. 110-113, doi: 10.31361/eaas.2018-2.029, 2018.
- [16] B. Boychev, G. Belyaev, V. Kostin, O. Ovcharenko and E. Trushkina, "Ionosphere parameters changing by interactive tropical cyclones according to Cosmos-1809 and Intercosmos Bulgaria-1300 satellite data," *SunGeo*, vol. 13 (1), pp. 31-39, 2018.
- [17] G. Belyaev, B. Hotinov, V. Kostin, E. Trushkina and O. Ovcharenko, "On the possibility of powerful underground explosions impact to release of the earth's crust stresses and on the development of hurricanes," *Fourteenth International Scientific Conference Space, Ecology, Safety – SES 2018. Sofia. Bulgaria. Proceedings*, pp. 403-409, 2018.
- [18] V.M. Kostin, G.G. Belyaev, O.Ya. Ovcharenko and E.P. Trushkina, "Parameters of the upper Ionosphere over Tropical Cyclones during changes in the stratosphere wind after the eruption of Mount Pinatubo," *Pushkov readings, IZMIRAN, Proceedings*, pp. 95-98, doi:10.31361/pushkov2019.022, 2019.
- [19] D.A. Mautner and C.P. Guard, "Annual tropical cyclone report," *Joint typhoon warning center, Guam, Mariana islands*, 269 p. 1992.
- [20] India Meteorological Department, "Report on cyclonic disturbances over north Indian Ocean in 1992," *Regional Specialized Meteorological Centre – Tropical Cyclones, New Delhi*, 48 p., 1993.
- [21] V. S. Sonwalkar, U.S. Inan, T.F. Bell, R.A. Helliwell, V.M. Chmyrev, Ya.P. Sobolev, O.Ya. Ovcharenko and V. Selegej, "Simultaneous observations of VLF ground transmitter signals on the DE 1 and COSMOS 1809 satellites: Detection of a magnetospheric caustic and a duct," *J. Geophys. Res.*, vol. 99 (A9), pp.17511-17522, 1994.
- [22] M. Hayakawa, "Earthquake Prediction with Radio Techniques," *John Wiley & Sons, Singapore Pte. Ltd.*, 294 p., doi: 10.1002/9781118770368, 2015.
- [23] G.G. Belyaev and V.M. Kostin, "Effects of powerful natural and anthropogenic processes in the ionosphere and on Earth," in V.D. Kuznetsov (ed.). *Electromagnetic and Plasma Processes from the Solar to the Earth's Interior*, IZMIRAN, pp. 170-184. 2015. www.izmiran.ru/IZMIRAN75/IRP/Belyaev.pdf.
- [24] K. Satake and B.F. Atwater, "Long-Term Perspectives on Giant Earthquakes and Tsunamis at Subduction Zones," *Annual Review of Earth and Planetary Sciences*, vol. 35, pp. 349-374, doi: 10.1146/annurev.earth.35.0311306.140302, 2007.

Novel Combinative Structure of High-Performance Solar Steam Device derived from Areca Nut

Tzu-min Chou¹, Jin-Long Hong^{2*}

Department of Materials and Science, National Sun Yat-sen University, Kaohsiung 80424, Taiwan, ROC

Abstract—A novel combinative structure, consisting of lateral hydrophobic pontoon oAN and central hydrophilic evaporator iAN, was designed for high-performance solar steam device. Both oAN and the iAN were derived from areca nut (AN), through different thermal and surface chemical treatments. With inferior water absorption and evaporation efficiency, the pontoon oAN nevertheless provides footage for the entire device, in contrast, although being efficient in water adsorption and evaporation, iAN requires the supporting oAN to keep its buoyancy. We therefore combined advantages of oAN and iAN to assemble a solar steam device with long-term stability and high solar thermal efficiency of ~82% under 1-sun illumination. The idea using combinative structure as efficient solar steam device can be further extended to other potential systems, therefore, this study provided foundation for future development of novel solar steam devices. importance.

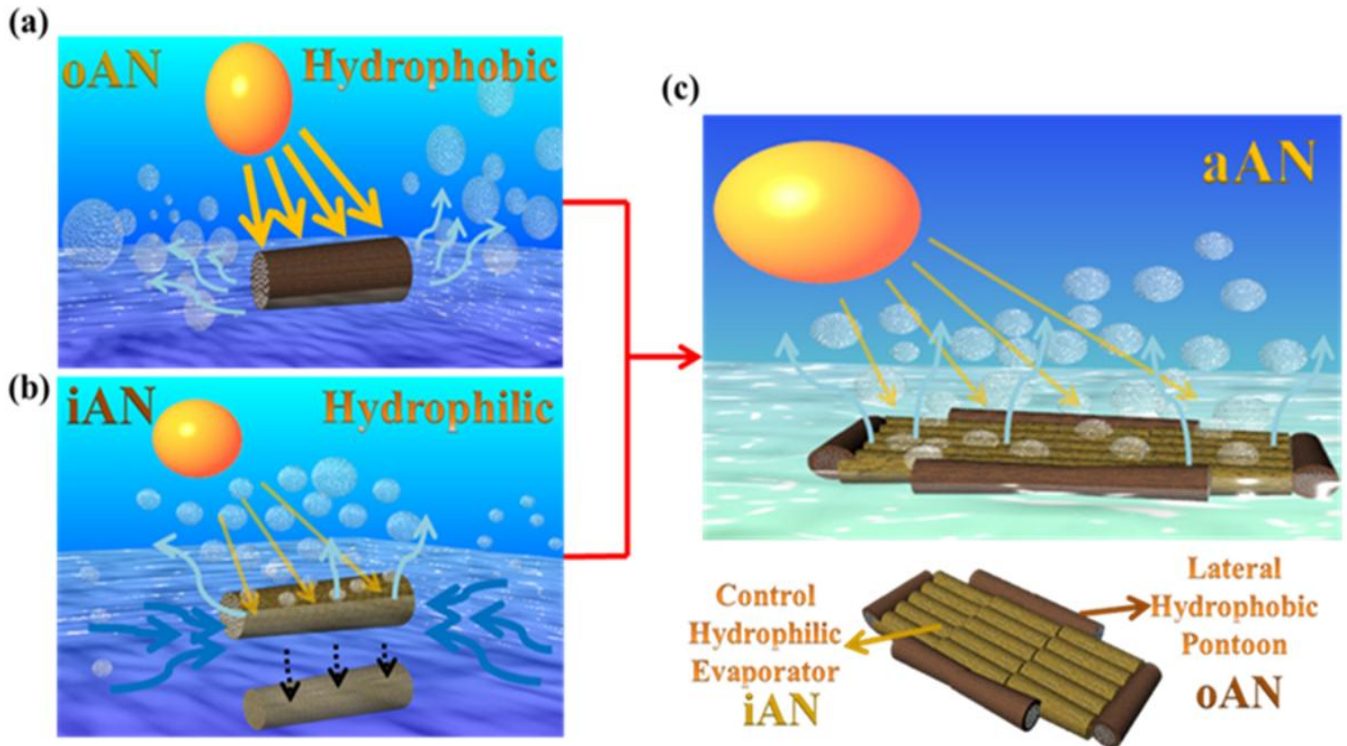
Keywords—Solar steam generation, areca nut, pontoon, supporter, combinative structure.

I. INTRODUCTION

Solar-driven water evaporation¹⁻⁸, which utilizes sunlight as a renewable energy source, is a promising approach to provide clean water with minimized environmental impact. Recently, an interfacial evaporation route using non submersible solar steam devices, has been proposed to improve heat localization at the liquid surface, which has successfully achieved high evaporation efficiency⁹⁻¹⁷. In this system, the confined thermal energy selectively heated up the water at the surface, thus minimizing heat loss to bulk water. Moreover, the surface temperature of the absorber is low due to effective evaporation, lowering radiation and convection heat losses at the absorber surface. With this scheme, solar-to-vapour conversion efficiencies can be as high as 90 this aspect, several natural materials, such as plants¹⁸⁻²¹, green leaf of *Scindapsus aureus*²² and trees²³, had been subjected to different surface treatments to result in interfacial evaporation systems for study.

In general, interfacial system can be classified into direct and indirect contact systems according to the relative position of the solar steam devices to the water surface. Direct contact configuration used self-floating hydrophobic absorbers derived from various materials, such as nanoparticles^{24,25} monolithic aerogel and foams^{6,26,27}, which are all capable of converting light into heat to vaporize the adsorbed water. However, this direct contact system is generally inferior in vaporizing the water, e.g. porous polymer-coding inorganic sheets²⁵ exhibited a solar thermal conversion efficiency of 63.6% under 1-sun irradiation. Aside from the self-floating means, films consisting of the absorber materials coating on light-weight and hydrophobic scaffolds, such as stainless steel (SS) mesh³, polypropylene (PP) mesh²⁸, gauze²⁹, and carbon fabric³⁰, were also reported. All these direct contact systems utilized hydrophobic absorbers, which have limited water vaporization routes and are therefore low in photo thermal conversion efficiency.

In contrast, indirect contact system involved a bilayered structure, with the top absorber layer absorbing the solar flux without contacting the bulk water and the bottom supporting layer offering stable support for the top solar steam devices. In general, the bottom layers referred to microporous structure with interconnected channels for efficient water supply, for which carbonized mushroom³¹ and basswood³² were previously used as hydrophilic components containing microporous channels for facile water absorption and vaporization, These carbonized mushroom and basswood exhibited a high conversion efficiency of 78% and 75%, respectively, but their long-term stability needed to be justified as we consider that the water adsorbed by the hydrophilic supporting materials would overload and sink the whole device eventually. The long-term stability problem may be reasonably improved by using hydrophobic supporting system, instead. Previously, polypryrrrole was used as the absorbent layer³⁰ on top of the supporting polypropylene (PP) membrane. This served as insulating layer minimizing the heat loss of the device to the bulk water, however, the reverse effect of the hydrophobic PP in preventing the water adsorption should just the conversion efficiency (58%) of the device.

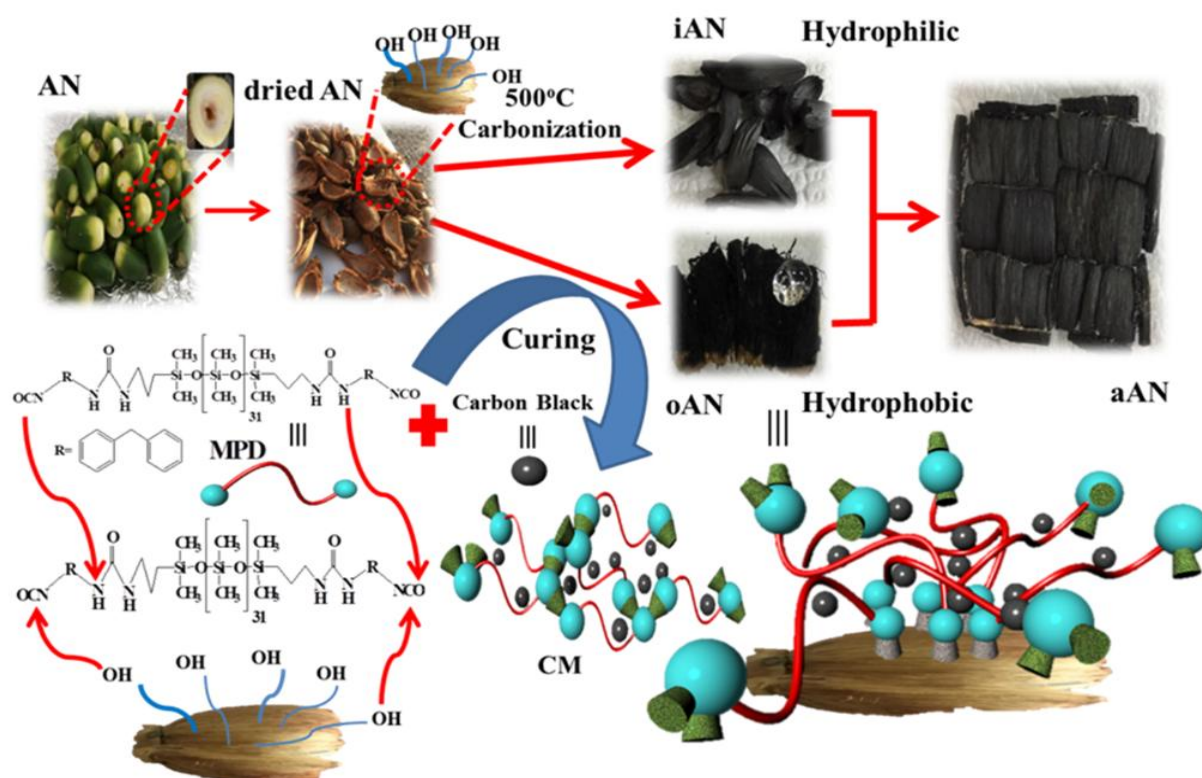


SCHEME 1: Illustrations of shortcomings of hydrophobic oAN (upper left) and iAN (lower left), and the combinative solar steam device of aAN (right) containing the lateral oAN pontoons and central iAN evaporator.

Rather than a bilayered structure mentioned above, this paper imparts new idea of using lateral pontoon (upper left, Scheme 1) as efficient supporting component to lift the central evaporator (lower left) over the water surface for a long time. Through surface thermal and chemical modifications of the natural areca nut (AN), both hydrophobic oAN pontoon and hydrophilic iAN evaporator can be successfully prepared and combined to fabricate a solar steam device of aAN (right) with separate supporting and evaporating components. Supposedly, water-resistant oAN is a perfect pontoon capable of floating whole device over the water surface but the vapors produced by sun heat would bypass the oAN, which prohibits the potential of using oAN as water evaporator, due to the water-repellency of the hydrophobic oAN. On the other hand, hydrophilic iAN enables the efficient water absorption and vaporization but along the process, the infiltrated water inside iAN would eventually overload and sink the whole device into the cold underwater, at which place iAN is unable to function properly as water evaporator. Nevertheless, shortcomings of oAN and iAN can be smartly avoided by assembling both components into one single aAN device, which contains both the lateral oANs and the central iAN as the supporting and steam-generation parts (lower left), respectively.

II. RESULTS AND DISCUSSION

Taking advantage of the unique structure of the integrated aAN device (Scheme 2), functions of solar steam-generation, water pumping and evaporation as well as supporting pontoon are decoupled into two components, with central hydrophilic iAN for water pumping and evaporation and the lateral hydrophobic carbon black nanoparticles CM-coated oAN for lifting the whole device over water surface. The central iAN and the lateral oAN prepared from different thermal and chemical surface treatment procedures were then glued together to result in the aAN-based solar steam device capable of standing over water surface for long enough time (> 1 month). To prepare iAN and oAN, we needed to peel off the green shell of AN and cut it into two pieces. The enriched vascular bundle structure (magnified part of the upper leftmost) of the cut piece is beneficial for water adsorption and transport. The cut pieces were then dried under vacuum for 24 hr to obtain the dried AN for different treatments to result in iAN and oAN, respectively.



SCHEME 2: Preparation process of aAN-based solar steam device.

Direct carbonization of the dried AN in a horizontal tubular reactor at 500°C for 2 hr provided hydrophilic iAN (Scheme 2) for use. In contrast, preparation of oAN required delicate chemical modification using a methylene diphenyl diisocyanate (MDI)-terminated poly(dimethyl siloxane) (MPD, cf. Experimental section for synthesis) as the multi-functional reagent, which enabled the facile crosslinking reactions between isocyanate groups of MPD and phenolic functions over the surface of the dried AN and also, served as excellent dispersant of carbon black (CB). End-capping of an amine-terminated poly(dimethyl siloxane) (PD) with hexamethyl diisocyanate (HDI) afforded MPD with urea linkages and isocyanate functional groups at the ends. Previous study³³ in our lab already verified the facile self-reaction of MPD that its urea linkages can attack its isocyanate terminals (lower) to result in hydrophobic crosslinking network. In the presence of dried AN, additional inter-reaction between isocyanate terminals of MPD and the surface phenolic OH functions of AN acted to reinforce the interfacial adhesion between the resulting crosslinked network and dried AN. Moreover, the MPD can be an excellent dispersant for CB, which can mix with equal weight of CB in tetrahydrofuran (THF) solvent to result in homogenous solution with long term stability. The hydrogen bond interactions between the urea NH and urea C=O of MPD and the COOH of CB are responsible for the homogeneous dispersion of CB by MPD. The homogenous THF solution was then applied over the surfaces of the dried ANs before being heated at 120 °C for 3 hr to result in homogenous CB-included CM composite. Large amounts of CB in CM composite should be gripped firmly by the crosslinked network since we see no sign of CB leakage after the whole aAN component had been placed on water for a long time (>1 month).

Scanning electron microscopy (SEM) images of iAN (Fig. 1(a)-(b)) revealed its unique structure beneficial for the water adsorption, transport and vaporization. SEM morphology of iAN (Fig. 1(a)) is similar with AN (Fig. 1(e)), which suggests that the enriched water paths in the pristine survive after high-temperature carbonization at 500°C. The enriched water paths of iAN were ensured by the abundant macro (red circle, Fig. 1(b)) and micro (blue circle) pores in the xy plane, as well as the macro (blue circle, Fig. 1(c)) and micro (red circle) cylindrical channels in the yz plane. All the pores and channels with few to several micrometers in sizes formed a continuous 3D porous network, which provides versatile routes for the water adsorption and transport. Under the assistance of capillary force and additional driving force induced by water evaporation, water transported fluently from the bottom of bulk water to the top surface of iAN. In addition, the peeling of surface layer during preparation step left a plethora of broken channels (Fig. 1(d)) on the surface of iAN, which are open to the air and under sunlight illumination, the open channels provide facile vaporization paths to the air.

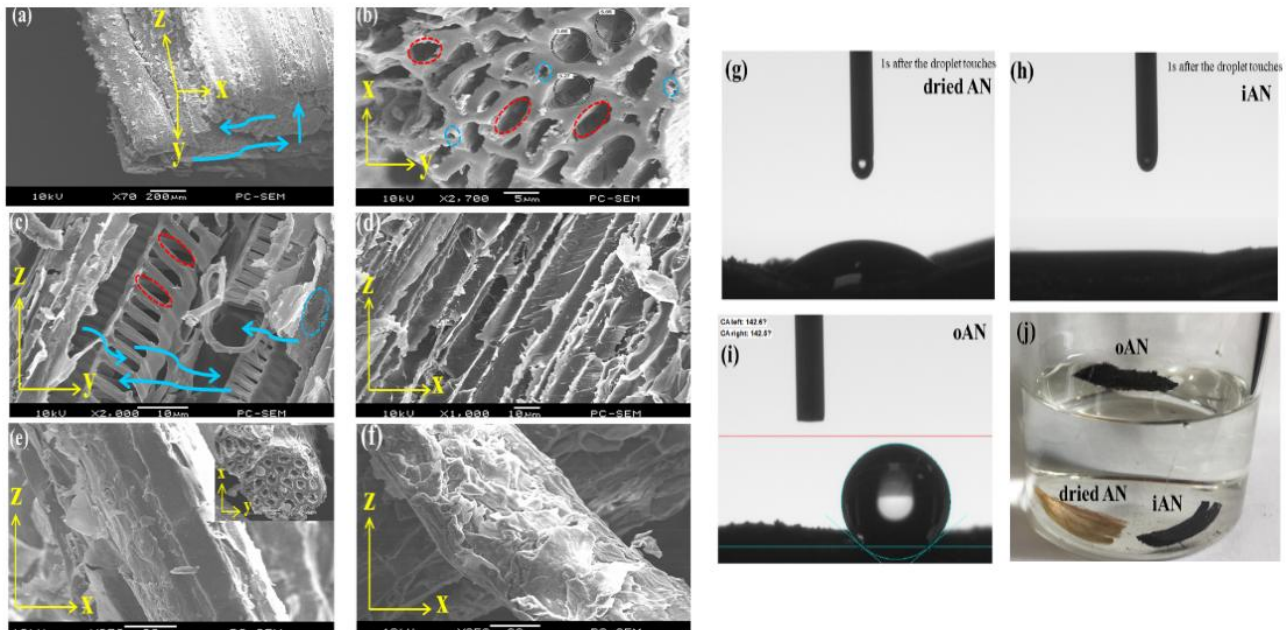


FIG. 1. SEM images of (a) iAN with the x, y, and z directions, (b) iAN with the macro (red circle) and micro (blue circle) pores in spherical shape, (c) iAN with the macro (blue circle) and micro (red circle) channels in cylindrical shape, (d) surface view of iAN with the broken vessels, (e) dried AN and (i) oAN with the rough surfaces. Absorptions of water droplets by the surfaces of (g) dried AN and (h) iAN, and (i) AN and (j) optical images of the floating oAN and the sunken AN and iAN.

Moreover, SEM can identify the morphological difference between dried AN (Fig. 1(e)) and oAN (Fig. 1(f)). Except the broken channels, surface of dried AN is relatively smooth compared to the rough, wrinkled surface of oAN. The rough surface of oAN is full of the CB-included CM composite, which is hydrophobic layer with repulsion to the incoming water. This rough, wrinkled surface of oAN is of great importance in view that such morphology dramatically raised the surface roughness to provide a composite interface in which air became trapped within the grooves under water, therefore inducing hydrophobicity with phenolic OH groups and the enriched porous structure, dried AN can absorb water readily. After carbonization, the enriched pores and channels of iAN provided the fluent water absorption and transport paths and therefore, the hydrophilicity of the sample. Surface wetting is another important parameter, which influences interfacial solar membrane performance. The round water droplet deposited on the surface of the dried AN was still elliptical in shape within 1 s (Fig. 1(g)), in contrast, the round water droplet was completely absorbed by the hydrophilic iAN (Fig. 1(h)) within the same 1 s period. A hydrophobic surface with excellent water droplet roll-off is the desired property of oAN, which depends not only on the chemical nature on the hierarchical structure of the surface. Due to the nanoscale roughness and the hydrophobic nature of the CM coating, the modified oAN is hydrophobic in nature and the water droplet, dropped on the surface of oAN, immediately rolled off (Fig.1(i)) and yet, kept the spherical shape with a high contact angle ($> 140^\circ$). Even when pressed into the water, the black hydrophobic oAN can spontaneously float again (Fig.1(j)) because of the air “cushion” of the hydrophobic surface. In comparison, the dried AN and the carbonized iAN would sink into the bottom of the beaker as time goes by. Because the hydrophobic oAN can float on the air-water interface for a long time, it should serve well as pontoon to float the aAN device.

We chose CB as the light-absorbing material, because CB is a natural light absorber with a rich source of raw materials, together with very mature and low-cost industrial production. The incorporation of crosslinked network with CB resulted in stable light absorber of CM, which can be seen from comparing the optical properties of iAN with other light-absorbing materials (Fig. 2(a)), such as CM-coated wood and paper. The absorbance (A), reflectance (R) and transmittance (T) in the wavelength range from 190 nm to 2250 nm can be easily detected and analyzed with the simple relationship of $A = 1 - R - T$. As shown in Fig. 2(b) and (c), iAN is low in reflectance (less than 5% in the visible light region and less than 10% in the whole measurement region) and exhibits a near-zero transmittance. Accordingly, the absorbance of iAN ($> 92\%$, Fig. 2(d)) is superior to CM-coated wood and paper throughout the whole measurement region, which provides foundation for using iAN as the water evaporator in this study.

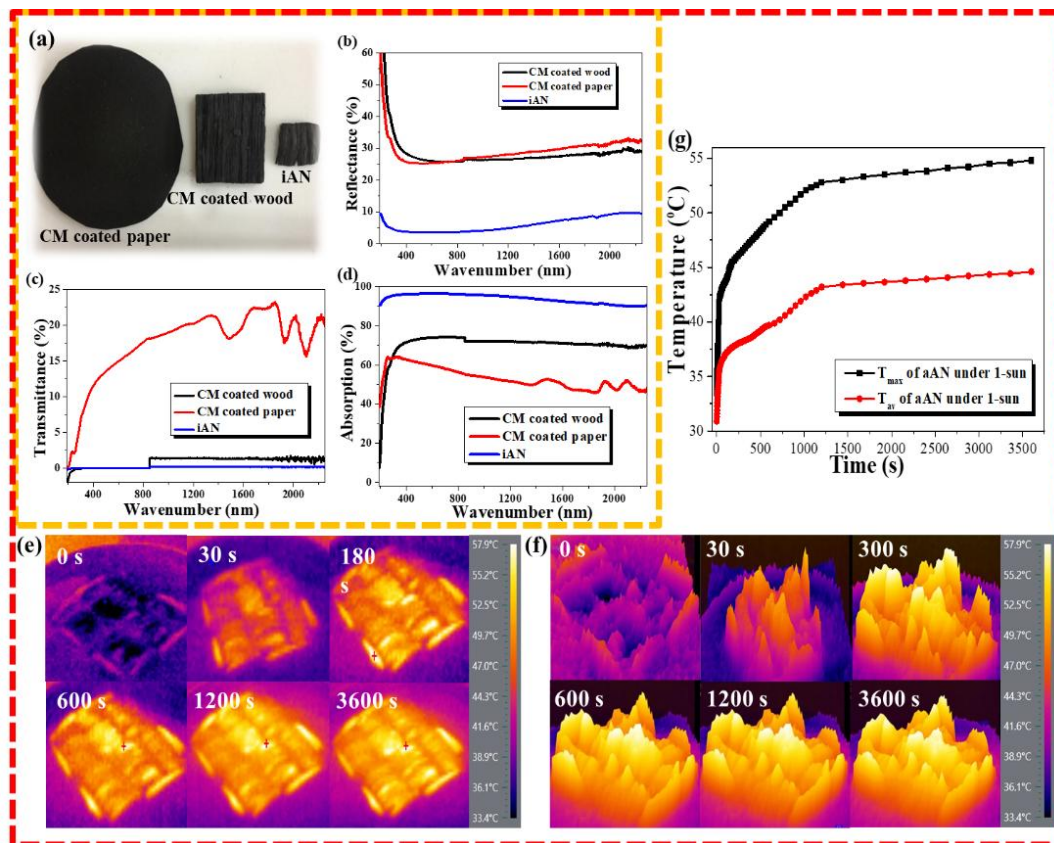


FIG. 2. (a) The appearance of oAN and the CM-coated wood and paper, and the UV-Vis spectra to trace the (b) reflectance, (c) transmittance and (d) absorbance in the wavelength range from 190 nm to 2250 nm, (e) Infrared photos of the aAN surfaces, (f) 3D display of infrared photos of the aAN surfaces, in order from left to right, correspond to $t = 0, 30, 180, 600, 1200,$ and 3600 s after illumination and (g) maximum and average temperatures of the surfaces of aAN as a function of time.

To evaluate the enhanced water vaporization of the free-floating aAN device, infrared thermal images (Fig. 2(e)) along with the 3D display (Fig. 2(f)) under 1-sun intensity were captured and the temperature profiles of aAN and the surrounding water were detected and analyzed. Temperature of aAN was relatively low (34°C) initially, indicating strong intrinsic evaporation as expected. The maximum (T_{max}) and average (T_{av}) temperatures plotted in Fig. 2(g) give clear view on temperature variation as a function of illumination time that both T_{max} and T_{av} rose rapidly once the illuminating light was turned on. Within 20 min of light irradiation, both T_{max} and T_{av} reached steady values and after 1 hr of illumination, T_{max} and T_{av} both reached 54°C and 44°C , respectively, which are high due to the high absorbance ($> 92\%$) of the iAN evaporator.

We then compared the evaporation rates and energy conversion efficiencies of the integrated aAN with CM-coated paper and wood by accurate examination of the corresponding weight changes (Fig. 3(a)) of all samples under 1-sun illumination. The aAN exhibited the largest mass changes among all samples, including pure water, oAN, iAN and CM-coated wood and paper. The evaporation rates here were calculated from the slope of the resolved curves, which gave relative evaporation rates of all samples under illumination. Here, because of the larger evaporating areas endowed by high fraction of pores and channels, the aAN exhibited a high evaporation rate of $1.31 \text{ kg m}^{-2} \text{ h}^{-1}$, which is comparatively higher than those of CM-coated paper ($0.83 \text{ kg m}^{-2} \text{ h}^{-1}$) and wood ($0.38 \text{ kg m}^{-2} \text{ h}^{-1}$) as well as oAN ($0.18 \text{ kg m}^{-2} \text{ h}^{-1}$) and iAN ($0.54 \text{ kg m}^{-2} \text{ h}^{-1}$). The hydrophobic CM coating tends to repel water to result in inferior water evaporation rates of the CM-coated paper, wood and oAN. The inferior evaporation rate of oAN and iAN indicates that both components are essential parts for aAN and cannot serve alone as efficient solar steam device. As the concepts illustrated in Scheme 1, the limited water absorption of the hydrophobic oAN and the inferior water evaporation of the submersible iAN are responsible for the low efficiencies of iAN and oAN, respectively. The energy conversion efficiency (η) is defined $\eta = \dot{m}h_{lv}/P_{in}$, where \dot{m} is the mass flux of steam, denotes the liquid-vapor phase change enthalpy, and P_{in} is the received power density of light illumination. In our instance, the efficiency of aAN was calculated to be 82% (Fig. 3(b)), which is higher than those of oAN (11%), iAN (34%), CM-coated paper (52%) and wood (24%).

The real durability of aAN in seawater needed to be considered for practical application and in this aspect, simulated sea water (a 3.5 wt% NaCl aqueous solution) under a simulated solar light intensity of 1-sun was applied and the desalination results were summarized in Fig. 3(e)-(f). Over the seawater for 2 hr, the wetted aAN was weighted to determine the weight change and dried in oven before next cyclization measurement. It is found that the performance is maintained for at least 5 cycles, with each cycle being over 2 hr. The resolved weight changes (Fig. 3(c)) over 5 cycles are almost the same and the calculated efficiency changes followed the same pattern that the initial efficiency curve versus time (Fig. 3(d) increased rapidly before becoming flatten, similar with the efficiency curve of sea water. According to the result, the efficiency retentions (Fig. 3(e)) over 5 cycles are almost the same, all with the resolved straight line paralleling to the X-axis, which points out that the solar steam device of aAN with a combinative structure is excellent in durability. It is curious to know the salt deposition situation, which can be evaluated from the SEM images of the samples after 5 cycles of 1-sun illumination, on the hydrophobic oAN (left, Fig. 3(f)) as well as the hydrophilic iAN (right). For oAN, few NaCl particles (yellow arrows) were deposited on the external surfaces, which suggested that adsorption of the saltwater was blocked by the hydrophobic surface of oAN. In contrast, the large amounts of salts were deposited over the outside and inside of the pores present in iAN sample, which clearly demonstrated the capability of iAN in adsorbing, transporting and vaporizing seawater. The NaCl salts in saltwater resulted in an evaporation efficiency (76%) slightly lower than that (82%) from the pure water, nevertheless, the resolve value of 76% is still higher than most of the reported data. Conductivity from LCR meter can be used to measure NaCl concentration in the saltwater before and after desalination. The concentration of sodium ion collected from the water in the condensation chamber was significantly decreased by at least four orders of magnitude after desalination, which was far below the salinity levels defined by World Health Organization (WHO), i.e. 1000 mg L⁻¹ and the US Environmental Protection Agency, i.e. L⁻¹, respectively. The successful solar desalination process of NaCl solution (3.5 wt%) further proves that our aAN exhibits good salt resistant property.

III. CONCLUSION

In summary, we have introduced a novel solar steam device aAN, with lateral hydrophobic oAN as supporting pontoon and central hydrophilic iAN as evaporator, for highly efficient solar steam device. With the hydrophobic CB-coated CM outer layer, oAN acted as efficient supporting material, in contrast, owing to the natural vessel structure and hydrophilicity, the iAN formed an ideal water adsorption, transport and vaporization system for solar steam device. In our instance, the efficiency of aAN was calculated to be 82%, which is higher than those of oAN (11%), iAN (34%), CM-coated paper (52%) and wood (24%). Although the evaporation of seawater by aAN is lower than that of pure water system, the desalination process still maintained a high conversion efficiency of 76% and showed a high value of 72% after 5 experiment cycles. Importantly, we had demonstrated that AN, a low-cost material (\$1.1 per kg), which can be easily obscured in the street corners of Asian cities, can be used to derive efficient solar steam device, through ingenious design idea using pontoon as separate supporting component. The idea of using pontoon as separate component of an efficient device can be extended to other existing or potential hydrophilic light absorbers, e.g. paper and wood.

IV. EXPERIMENTAL SECTION

4.1 Materials

Good-quality AN was purchased from a betel nut stand in Kaohsiung city, Taiwan. Amino-terminated poly(dimethyl siloxane) (PD, $M_w \sim 2,500$ g/mol), MDI and CB were all purchased from Sigma-Aldrich. Tetrahydrofuran (THF) was refluxed with benzophenone and sodium for 2 days in prior to distillation for use.

4.1.1 Preparation of hydrophilic carbonized areca nut (iAN)

Before carbonization, AN was dried under sun light at least 24 hr after thorough washing to remove any greasy or dust materials. The sun-dried AN was then heated in an oven at 120°C for 24 hr to remove moisture. Carbonization was carried out in a horizontal tubular reactor at 500°C for 2hr under nitrogen flow. The heating rate and nitrogen flow rate were 5°C/min and 200 mL/min, respectively. The sample was cooled down to room temperature under nitrogen atmosphere and was labeled as iAN (yield = 78%).

4.1.2 Preparations of MPD

MPD was required to be prepared first by the reported procedures³³. Before reaction, PD needed to be dried under vacuum at 80°C for 1 hr. Then, into an argon-blanketed, vigorously-stirred solution of PD (0.5 g, 0.1 mmol) in THF (10 mL), solution of MDI (55 mg, 0.2 mmol) in THF (5 mL) was added dropwise. The resultant mixture was then heated at 60°C for 5 hr under

argon atmosphere. Then the reaction mixtures were subjected to vacuum distillation at 70°C to remove most of the residual THF to obtain the desired MPD.

4.1.3 Preparation of hydrophobic MPD/CB (CM)-coated oAN

The unmodified AN was dried under sunlight for at least 24 hr after thorough washing to remove any greasy or dust materials. The sun-dried AN was then heated in an oven at 120°C for 24 hr to remove moisture. The dried AN was then immersed into a solution of MPD and CB in THF and the whole solution mixtures were stirred for another 2 hr for maximizing the absorption of MPD and CB. The MPD can be an excellent dispersant for CB, which can mix with equal weight of CB in tetrahydrofuran (THF) solvent to result in homogenous solution with long term stability. Then, the MPD/CB (CM) - coated AN was heated to cure at 120°C for 3 hr to obtain the desired oAN.

4.2 Characterization

Scanning electron microscope (SEM) images were recorded using a Jeol JSM-6700F microscope operated at 10 kV. A Krüss GH-100 goniometer interfaced to image-capture software was used to measure the static WCA. For the contact angle of water droplet (5 μ L) over surface of AN, iAN and oAN were measured using an FDSA MagicDroplet-100; each reported contact angle represents the average of six measurements. The simulated solar irradiation was provided by a MFS-PV BASIC (Hong-Ming Technology Co., Ltd.). Solar and the light intensity was adjusted to 1000 W m⁻². The UV-v is absorption, transmittance and reflectance spectra were recorded with a JASCO V-770 spectrophotometer. IR images of infrared photos were taken by IR Thermographic Camera (Sonel KT-80). The 3D display of infrared photos is draw using the Sonel ThermoAnalyze2 software. The electric properties were determined at room temperature by an LCR meter (Tonghui TH2829) at 1 kHz with taking five points for each data to average. The measurement distance of the two resistance measurers is fixed at 1 cm. The 1H NMR spectra were recorded by a Varian Unity VXR-500 MHz instrument. FTIR spectra were recorded from a Bruker Tensor 27 FTIR spectrophotometer; 32 scans were collected at a spectral resolution of 1cm⁻¹. The solid powders were homogeneously blended with KBr before pressed to make pellets for measurement.

ACKNOWLEDGEMENTS

This work is supported by the Ministry of Science and Technology (MOST), Republic of China (ROC), under the contract MOST107-2221-E-110 -015.

REFERENCE

- [1] M. Gao, L. Zhu, C. K. Peha and G. W. Ho, Solar absorber material and system designs for photothermal water vaporization towards clean water and energy production. *Energy Environ.Sci.*2019, pp. 841–864
- [2] J. Huang, Y. He, L. Wang, Y. Huang and B. Jiang, Bifunctional Au@ TiO₂ core–shell nanoparticle films for clean water generation by photocatalysis and solar evaporation. *Energy Convers. Manag.*2017, 132, 452-459.
- [3] J. Lou, Y. Liu, Z. Wang, D. Zhao, C. Song, J. Wu, N.Dasgupta, W. Zhang, D. Zhang, P. Tao, W. Shang and T.Deng, Bioinspired multifunctional paper-based rGO composites for solar-driven clean water generation. *ACS Appl. Mater. Interfaces*2016, 8, 14628-14636.
- [4] Y. Liu, J. Chen, D. Guo, M. Cao and L. Jiang, Floatable, self-cleaning, and carbon-black-based superhydrophobic gauze for the solar evaporation enhancement at the air–water interface. *ACS Appl. Mater. Interfaces*, 2015, 7, 13645-13652.
- [5] P. Zhang, J. Li, L. Lv, Y. Zhao and L. Qu, Vertically aligned graphene sheets membrane for highly efficient solar thermal generation of clean water. *ACS Nano* 2017,11, 5087-5093.
- [6] L. Zhu, C. F. Tan, M. Gao and G. W. Ho, Design of a Metal Oxide–organic framework (MoOF) foam microreactor: solar-induced direct pollutant degradation and hydrogen generation. *Adv. Mater.*2015, 27, 7713-7719.
- [7] L. Zhu, M. Gao, C. K. N. Peh, X. Wang and G. W. Ho, Self-contained monolithic carbon sponges for solar-driven interfacial water evaporation distillation and electricity generation. *Adv. Energy Mater.* 2018, 8, 1702149.
- [8] L. Zhu, M. Gao, C. K. N. Peh and G. W. Ho, Solar-driven photothermal nanostructured materials designs and prerequisites for evaporation and catalysis applications. *Mater. Horizons* 2018, 5, 323-343.
- [9] P. Tao, G. Ni, C. Song, W. Shang, J.Wu, J. Zhu, G. Chen and T. Deng, Solar-driven interfacial evaporation. *Nature Energy* 2018, 3, 1031–1041.
- [10] Z. Wang, Y. Liu, P. Tao, Q. Shen, N. Yi, F. Zhang, Q. Liu, C. Song, D. Zhang, W. Shang, and T. Deng, Bio-inspired evaporation through plasmonic film of nanoparticles at the air–water interface. *Small*. **2014** Aug 27; 10(16):3234-9.
- [11] H.Ghasemi, G. Ni, A. Marie Marconnet, J. Loomis, S.Yerci, N.Miljkovic and G. Chen, Solar steam generation by heat localization. *Nature Commun.*2014, 5, 4449.
- [12] Zhang P, Li J, Lv L, Zhao Y and Qu L, Vertically aligned graphene sheets membrane for highly efficient solar thermal generation of clean water. *ACS Nano* 2017, 11, 5087-5093.

- [13] P. Yang, K. Liu, Q. Chen, J. Li, J. Duan, G. Xue, Z. Xu, W. Xie and J. Zhou, Solar-driven simultaneous steam production and electricity generation from salinity. *Energy Environ. Sci.* 2017, 10, 1923-1927.
- [14] L. Zhou, Y. Tan, B. Zhu, P. Zhang, J. Xu, Q. Gan, Z. Yu and J. Zhu, Self-assembly of highly efficient, broadband plasmonic absorbers for solar steam generation. *Sci. Adv.* **2016**, 2, e1501227.
- [15] L. Zhou, Y. Tan, J. Wang, W. Xu, Y. Yuan, W. Cai, S. Zhu and J. Zhu, 3D self-assembly of aluminium nanoparticles for plasmon-enhanced solar desalination. *Nat. Photonics.* 2016, 10, 393-398.
- [16] J. Wang, Y. Li, L. Deng, N. Wei, Y. Weng, S. Dong, D. Qi, J. Qiu, X. Chen and T. Wu, High-performance photothermal conversion of narrow-bandgap Ti_2O_3 nanoparticles. *Adv. Mater.* 2017, 29, 1603730.
- [17] H. Ren, M. Tang, B. Guan, K. Wang, J. Yang, F. Wang, M. Wang, J. Shan, Z. Chen, D. Wei, H. Peng and Z. Liu, Hierarchical graphene foam for efficient omnidirectional solar-thermal energy conversion. *Adv. Mater.* 2017, 29, 1702590.
- [18] J. Song, C. Chen, C. Wang, Y. Kuang, Y. Li, F. Jiang, Y. Li, E. Hitz, Y. Zhang, B. Liu, A. Gong, H. Bian, J. Zhu, J. Zhang, J. Li and L. Hu, High-performance solar steam device with layered channels: artificial tree with a reversed design. *ACS Appl. Mater. Interfaces* 2017, 9, 23520.
- [19] C. Jia, T. Li, C. Chen, J. Dai, I. M. Kierzewski, J. Song, Y. Li, C. Yang, C. Wang and L. Hu, Scalable, anisotropic transparent paper directly from wood for light management in solar cells. *Nano Energy* 2017, 36, 366.
- [20] C. Chen, Y. Zhang, Y. Li, Y. Kuang, J. Song, W. Luo, Y. Wang, Y. Yao, G. Pastel, J. Xie, L. Hu, Rich mesostructures derived from natural woods for solar steam generation. *Adv. Energy Mater.* 2017, 7, 1700595.
- [21] K.-K. Liu, Q. Jiang, S. Tadepalli, R. Raliya, P. Biswas, R. R. Naik, S. Singamaneni, Wood-graphene oxide composite for highly efficient solar steam generation and desalination. *ACS Appl. Mater. Interfaces* 2017, 9, 7675-7681.
- [22] S. Zhuang, L. Zhou, W. Xu, N. Xu, X. Hu, X. Li, G. Lv, Q. Zheng, S. Zhu, Z. Wang, and J. Zhu, Tuning transpiration by interfacial solar absorber-leaf engineering. *Adv. Sci.* 2018, 5, 1700497.
- [23] C. Chen, Y. Zhang, Y. Li, J. Dai, J. Song, Y. Yao, Y. Gong, I. Kierzewski, J. Xie and L. Hu, All-wood, low tortuosity, aqueous, biodegradable supercapacitors with ultra-high capacitance. *Energy Environ. Sci.* 2017, 10, 538-545.
- [24] Z. Wang, Y. Liu, P. Tao, Q. Shen, N. Yi, F. Zhang, Q. Liu, C. Song, D. Zhang, W. Shang and T. Deng, Bio-inspired evaporation through plasmonic film of nanoparticles at the air-water interface. *Small* 2014, 10, 3234-3239.
- [25] Z. Hua, B. Li, L. Li, X. Yin, K. Chen and W. Wang, Designing a novel photothermal material of hierarchical microstructured copper phosphate for solar evaporation enhancement. *J. Phys. Chem. C* 2017, 121, 60-69.
- [26] X. Hu, W. Xu, L. Zhou, Y. Tan, Y. Wang, S. Zhu and J. Zhu, Tailoring graphene oxide-based aerogels for efficient solar steam generation under one sun. *Adv. Mater.* 2017, 29, 1604031.
- [27] Y. Fu, G. Wang, T. Mei, J. Li, J. Wang and X. Wang, Y. Fu, G. Wang, T. Mei, J. Li, J. Wang and X. Wang, Accessible graphene aerogel for efficiently harvesting solar energy. *ACS Sustain. Chem. Eng.* 2017, 5, 4665-4671.
- [28] M. Ye, J. Jia, Z. Wu, C. Qian, R. Chen, P. G. O'Brien, W. Sun, Y. Dong and G. A. Ozin, Synthesis of black TiO_x nano particles by Mg reduction of TiO_2 nanocrystals and their application for solar water evaporation. *Adv. Energy Mat.* 2017, 7, 1601811.
- [29] M. W. Higgins, A. R. Shakeel Rahman, R. R. Devarapalli, M. V. Shelke and N. Jha, Carbon fabric based solar steam generation for waste water treatment. *Sol. Energy*, **2018**, 159, 800-810.
- [30] X. Huang, Y.-H. Yu, O. de Llergo, S. M. Marquez and Z. Facile, Facile polypyrrole thin film coating on polypropylene membrane for efficient solar-driven interfacial water evaporation. *RSC Adv.* 2017, 7, 9495-9499.
- [31] N. Xu, X. Hu, W. Xu, X. Li, L. Zhou, Mushrooms as efficient solar steam-generation devices. *Adv. Mater.* **2017**, 29, 1606762.
- [32] Y. Kuang, C. Chen, S. He, E. M. Hitz, Y. Wang, W. Gan, R. Mi, and L. Hu, A High-performance self-regenerating solar evaporator for continuous water desalination. *Adv. Mater.* 2019, 1900498
- [33] C. H. Chung, W. C. Liu and J. L. Hong, Superhydrophobic melamine sponge modified by cross-linked urea network as recyclable oil absorbent materials. *Ind. Eng. Chem. Res.* 2018, 57, 25, 8449-8459.

Discussion on Inexact Optimal Solution under Fuzzy Environment

Pei-Chun Feng

Department of Administrative Management, Central Police University, Taiwan

Abstract—The purpose of this paper is to explain that a convex combination of several partial solutions using a new criterion which did not solve the fuzzy problem. The main feature of this paper is twofold. First, we prepare a simple optimization problem to explain the previously proposed approach that considered criteria separately. Consequently, we conclude, previous results are partial solutions. Secondly, we study the same optimization problem as the one that appears in a previously published paper. After his new criterion is added, we solve the new fuzzy optimization problem to demonstrate that the previous solution is not the optimal one. Hence, the previously proposed approach is questionable and then his assertion of the meaninglessness of the exact optimal solution for the fuzzy problem cannot be treated as a valid statement. At last, we cite a paper that had referred to the questionable approach which had been improved by another published article to support our argument.

Keywords—Fuzzy set, decision making, optimization, genetic algorithms, linear programming.

I. INTRODUCTION

Zadeh [1] introduced the concept of fuzzy set theory, and then Bellman and Zadeh [2] proposed the decision-making problem in a fuzzy environment. Zimmermann [3] applied the fuzzy set theory with proper membership functions to solve linear programming problems with several objective functions. Fuzzy set theory not only provided a mathematical way of representing imprecision or vagueness but also fuzzy linear programming has been applied to many practical areas such as production planning, resources allocation, transportation problems, and so on. Based on Zimmermann's method, the fuzzy objective functions, and fuzzy constraints and transferred to crisps ones by membership functions with the max-min operator. Hence, a unique exact optimal solution with the highest membership degree is derived. However, Wang [5] assumed that the exact optimal solution may not be desired by the decision-maker, owing to there being another criterion that is preferred by the decision-maker. He first found a family of inexact solutions, with an acceptable membership degree, that is obtained by a genetic algorithm with mutation along the weighted gradient direction. These solutions developed a convex set in the neighborhood of the exact optimal solution. Next, under the new criterion, he considered human-computer interaction to derive his *fuzzy optimal solution*. There are ten papers (e.g., Tang and Wang [6]; He et al. [8]; Ma et al. [9]; Tang et al.[10]; Van Hop [11]; Chiu et al. [13]; Lu et al. [14]; Baykasoglu and Gocken [15]) which have referred to Wang [5] in their references. However, none of them discovered the questionable results of Wang [5] that will be explained and revised in this paper. In this paper, we will carefully examine Wang's approach. After we add the new criterion preferred by the decision-maker into the fuzzy optimization problem, the result is that Wang's method will derive an unwarranted solution. We will demonstrate that his approach has a severe logic fault and that his assertion of "exact optimal solution in the fuzzy environment is meaningless" should be treated as invalid.

II. MATERIALS AND METHODS

The detailed description of Wang's approach, please refer to his paper. In the following, we just provide a very brief introduction. He mentioned that "However, the exact optimal solution may not be desired by the decision maker, because the membership function is not the preference criterion of the decision-maker. In general, the data are imprecise in a fuzzy environment, thus, it is meaningless to calculate an exact solution."

It means that there are two fuzzy optimization problems. We explicitly define as

- a) The original fuzzy optimization problem, before the new criterion is added.
- b) The new fuzzy optimization problem, after the new criterion, is added.

In the beginning, without the new criterion, Wang [5] considered the original fuzzy optimization problem to use a genetic method to obtain a family of acceptable solutions. Those solutions are in the neighborhood of the exact optimal solution for the original fuzzy optimization problem.

Next, a new criterion is added, so that Wang tried to solve the new fuzzy optimization problem. He studied the convex combination of two points in the family that satisfies the new criterion, and then he claimed that his solution is the fuzzy optimal solution.

III. RESULTS

3.1 Discussion of Wang's approach

Wang's solution is a convex combination of several solutions in the neighborhood of the original exact optimal solution (before the new criterion is added), different genetic computation will produce different results to constitute the family of inexact solutions with acceptable membership degree. Therefore, researchers following Wang's method will derive different fuzzy optimal solution depending on the results of the genetic algorithm. For fuzzy optimization problems, different researchers applied the same method to derive different results that seem quite suitable under imprecise condition. However, let us consider the following problem:

$$\max x - y \quad (1)$$

$$\text{s.t. } x \geq 0, x \geq y, \text{ and } x^2 + y^2 \leq 1.$$

The new criterion preferred by decision-maker is

$$y = 0 \quad (2)$$

We will follow Wang's method to solve the above problem. If we assume that the acceptable solution has to satisfy $x - y \geq 0.5$. Next, we check the convex property of the constraint

$$x \geq y \quad (3)$$

That is, if (x_1, y_1) and (x_2, y_2) satisfy equation (3), then the convex combination $\lambda(x_1, y_1) + (1 - \lambda)(x_2, y_2)$ with $0 \leq \lambda \leq 1$ also satisfies equation (3).

The convex property of the constraint

$$x^2 + y^2 \leq 1, \quad (4)$$

can be verified as follows. We assume that (x_1, y_1) and (x_2, y_2) satisfy equation (4), then the convex combination is

$$\lambda(x_1, y_1) + (1 - \lambda)(x_2, y_2) = (\lambda x_1 + (1 - \lambda)x_2, \lambda y_1 + (1 - \lambda)y_2) \quad (5)$$

We evaluate that

$$\begin{aligned} & (\lambda x_1 + (1 - \lambda)x_2)^2 + (\lambda y_1 + (1 - \lambda)y_2)^2 \\ &= \lambda^2(x_1^2 + y_1^2) + (1 - \lambda)^2(x_2^2 + y_2^2) + 2\lambda(1 - \lambda)(x_1x_2 + y_1y_2). \end{aligned} \quad (6)$$

We can consider $x_1x_2 + y_1y_2$ as the inner product of (x_1, y_1) and (x_2, y_2) , the owing to Schwarz's inequality, with $x_1^2 + y_1^2 \leq 1$ and $x_2^2 + y_2^2 \leq 1$, we know that

$$x_1x_2 + y_1y_2 \leq \sqrt{x_1^2 + y_1^2} \sqrt{x_2^2 + y_2^2} \leq 1 \quad (7)$$

so that we may rewrite equation (6) as

$$(\lambda x_1 + (1 - \lambda)x_2)^2 + (\lambda y_1 + (1 - \lambda)y_2)^2 \leq \lambda^2 + (1 - \lambda)^2 + 2\lambda(1 - \lambda) = 1 \quad (8)$$

Hence, the convex combination also satisfies equation (4). Similarly, the constrain, $x_1, x_2, x \geq 0$, also has convex property.

Before the new criterion, equation (2) is added, for the original fuzzy optimization problem, applying some iterative process, among many results, for examples, we select $(x_1, y_1) = (0.995, 0.1)$ and $(x_2, y_2) = (0.954, -0.3)$ to create the family of inexact solutions.

Next, the new criterion, equation (2) is added, following Wang's approach, we need to solve the convex combination that satisfies the new criterion, that is

$$\lambda(x_1, y_1) + (1 - \lambda)(x_2, y_2) = (x, 0) \quad (9)$$

to find that $\lambda = 0.75$ and

$$\lambda(x_1, y_1) + (1 - \lambda)(x_2, y_2) = (0.985, 0) \quad (10)$$

Wang [5] believed that $(0.985, 0)$ is the fuzzy optimal solution by his approach.

We must point out that the new criterion of equation (2) should be obeyed by every researcher who tried to solve the original problem of equation (1). It is independent of the solution method. Hence, after the new criterion of equation (2) is given, then the optimization problem already changed to

$$\max x - y \quad (11)$$

$$\text{s.t. } x \geq 0, x \geq y, y = 0 \text{ and } x^2 + y^2 \leq 1.$$

We may rewrite equation (10) as follows

$$\max x \quad (12)$$

$$\text{s.t. } x \geq 0 \text{ and } x^2 \leq 1, \text{ to derive the exact optimal solution}$$

$$x^* = 1 \text{ and } y = 0 \quad (13)$$

Wang [5] claimed that the result of equation (10) is the fuzzy optimal solution. However, the exact optimal solution of equation (13) is meaningless.

We have to say that Wang [5] forgot to realize that the new constraint must be used by every practitioner so the optimization problem already changed from equation (1) to equation (11), or simplified version, equation (12). Wang [5] insisted on using some partial solutions for the equation (1), and then considered the new criterion later to obtain his result. It means that in Wang's approach, criteria can be considered separately.

In the following, we will demonstrate in detail that this separate consideration of constraints will produce chaos. We will consider the previous problem in four steps.

First, we only consider

$$\max x - y \quad (14)$$

$$\text{s.t. } x \geq 0 \text{ and } x^2 + y^2 \leq 1.$$

And then under some complicated computation to select two initial solutions, for examples, $(x_1, y_1) = (0.6, 0.8)$ and $(x_2, y_2) = (0.6, -0.8)$.

Second, we consider the new criterion, $y = 0$ to find $\lambda = 0.5$ and

$$\lambda(x_1, y_1) + (1 - \lambda)(x_2, y_2) = (0.6, 0) \quad (15)$$

Third, we check whether or not the constraint, $x \geq y$ is satisfied, and then discover that $0.6 - 0 = 0.6 \geq 0$.

Fourth, we check the acceptable solution that has to satisfy $x - y \geq 0.5$. It shows that $0.6 - 0 = 0.6 \geq 0.5$.

According to the above discussion, a fuzzy optimal solution, $(0.6, 0)$, proposed by Wang [5] is obtained.

Before the convex combination, both $(x_1, y_1) = (0.6, 0.8)$ and $(x_2, y_2) = (0.6, -0.8)$ are not satisfy the criterion of $x \geq y$ and $x - y \geq 0.5$. However, afterward, the convex combination, $(0.6, 0)$ accidentally satisfies their two criteria. It indicates that by Wang's approach, some illogical solution can be the cornerstone of the next step derivation. It reveals that Wang's approach is not inexact but arbitrary.

The above example illustrates that Wang [5] committed a severe logic mistake in separately considering those constraints. Those constraints should be examined simultaneously.

3.2 A numerical example

In this section, we reconsider the numerical example of Wang [5], and we will point out the questionable aspects of the results of Wang [5].

A plant tries to produce two kinds of products, A and B, and the net profit of A and B are 6 and 4. The production of A and B needs labor time and a kind of main material. The labor and material requirements of each A are 2 labor unit time and 4 units, separately. Those of B are 3 labor unit time and 2 units. The available labor time is 70 units. By using overtime work, the plant can have an additional 30 units of labor time. The available material amount is 100 units, and there are 20 units safety storage of the material which is controlled by the general manager of this plant. The decision maker hopes that the objective profit reaches 200, at least not less than 160, and the overtime work and consumption of safety storage are not used too much. Hence, Wang [5] tries to consider the following fuzzy objective/resource optimization problem:

$$\max \quad \alpha \quad (16)$$

$$\text{s.t. } g_0(x_1, x_2) = 6x_1 + 4x_2 \geq 200 - (1 - \alpha)40 \quad (17)$$

$$g_1(x_1, x_2) = 2x_1 + 3x_2 \leq 70 + (1 - \alpha)30 \quad (18)$$

$$g_2(x_1, x_2) = 4x_1 + 2x_2 \leq 100 + (1 - \alpha)20 \quad (19)$$

$$x_1, x_2 \geq 0, \alpha \in [0, 1].$$

By the Zimmermann's tolerance approach, Wang mentioned that the exact optimal solution is $(x_1^*, x_2^*) = (20, 15)$, $\mu_{\tilde{z}}(x_1^*, x_2^*) = 0.5$ and the optimal value is 180. Wang [5] tried to use a genetic method with the mutation along the weighted gradient direction. The population size is $NG = 100$, the acceptable membership degree is $\alpha = 0.3$ to solve this problem. After 228 generations, Wang [5] claimed that the solutions $z2(0)$ and $z2(1)$ are better, and then he selected the labor constraint as the comparison criterion for $z2(0)$ and $z2(1)$. He mentioned that if the combination coefficient $\lambda = 0.9116$ then there is no overtime. Wang [5] derived the combined solution

$$z = \lambda z2(1) + (1 - \lambda)z2(0) = (25.1715, 6.5523) \quad (20)$$

the objective value, $g_0(z) = 177.2383$, the membership function, $\mu_{\tilde{z}}(z) = 0.31047$, and the constraints, $g_1(z) = 70$, $g_2(z) = 113.7907$.

Following Wang's [5] descriptions, the new condition is that there is no overtime. Therefore, practitioners should consider the following new fuzzy objective/resource optimization problem:

$$\max \quad \alpha \quad (21)$$

$$\text{s.t. } g_0(x_1, x_2) = 6x_1 + 4x_2 \geq 200 - (1 - \alpha)40 \quad (22)$$

$$g_2(x_1, x_2) = 4x_1 + 2x_2 \leq 100 + (1 - \alpha)20 \quad (23)$$

$$x_1, x_2 \geq 0, \alpha \in [0, 1].$$

IV. DISCUSSION

4.1 Our approach for the numerical example of Wang [5]

Our simple way to solve the above optimization is to assume that. $2x_1 + 3x_2 = A$, with $A \leq 70$. Hence, we replace x_2 by $(A - 2x_1)/3$ to rewrite the fuzzy objective/resource optimization problem:

$$\max \alpha \quad (24)$$

$$\text{s.t. } 5x_1 + 2A \geq 240 + 60\alpha \quad (25)$$

$$4x_1 + A \leq 180 - 30\alpha \quad (26)$$

$$A \leq 70, 0 \leq x_1 \leq 35, \alpha \in [0, 1].$$

From the restriction of x_1 , it yields that

$$\frac{240 + 60\alpha - 2A}{5} \leq x_1 \leq \frac{180 - 30\alpha - A}{4} \quad (27)$$

It follows that

$$20 + 130\alpha \leq A \leq 70 \quad (28)$$

and then

$$\alpha \leq \frac{5}{13} \approx 0.385 \quad (29)$$

We find the maximum possible of α under the new criterion.

It implies that if we take $\alpha = \frac{5}{13}$ and then solve the inequality of equation (28), then $A = 70$ so that it rewrites equations (27) as

$$\frac{320}{13} \leq x_1 \leq \frac{320}{13} \approx 24.615 \quad (30)$$

Hence g_0 and g_2 are both active, and then we obtain that $x_2 = 6.923$, $g_0(z) = 175.385$, $g_1 = 70$, $g_2(z) = 112.308$ and $\mu_{\tilde{g}}(z) = 0.385$.

Our solution attains the maximum value of α . On the other hand, Wang's [5] result, $\mu_{\tilde{g}}(z) = 0.31047$ did not attain the maximum value of α .

Our work reveals that Wang's approach did not solve the fuzzy objective/resource optimization problem under his new conditions. Consequently, based on Wang's inexact approach his claim of the meaninglessness of the exact optimal solution for fuzzy problems is questionable.

4.2 Our patchwork for another problem in Wang [5]

For completeness, we will prepare a patchwork to show another problem in Wang's inexact approach to finding the fuzzy optimal solution.

In our demonstration example, before the new criterion, equation (2), is added into the system, for the original fuzzy optimization problem (applying some iterative process, among many results), we select $(x_1, y_1) = (0.995, 0.1)$ and $(x_2, y_2) = (0.954, 0.3)$ to create the family of inexact solutions.

Next, the new criterion, equation (2) is added, following Wang's approach, we need to solve the convex combination that satisfies the new criterion, that is

$$\lambda(x_1, y_1) + (1 - \lambda)(x_2, y_2) = (x, 0) \quad (31)$$

Under the condition $0 \leq \lambda \leq 1$, it yields that there is no solution for λ .

This illustrates an implicit problem in Wang's approach: Why are there points on the convex combination that satisfy the new criterion?

Next, we return to the example of Wang [5]. If the decision-maker hopes to achieve a big profit and more product B, then he will select the labor constraint as the comparison criterion for $z_2(0)$ and $z_2(2)$.

It means $z_2(0) = (20.0293, 16.8886)$ and $z_2(2) = (15.4291, 19.9664)$, with the convex combination

$$\lambda(z_2(0)) + (1 - \lambda)(z_2(2)) = (15.4291 + 4.6001\lambda, 19.9664 - 3.0778\lambda) \quad (32)$$

with $0 \leq \lambda \leq 1$. However none of them satisfies the new criterion, that is

$$2(15.4291 + 4.6001\lambda) + 3(19.9664 - 3.0778\lambda) = 70 \quad (33)$$

Equation (33) has only one solution at $\lambda = 625.223$ that is not in the domain of $[0, 1]$.

We may raise another question: if there are two solutions, λ_1 and λ_2 , with $0 \leq \lambda_1 < \lambda_2 \leq 1$ so that both $\lambda_1(x_1, y_1) + (1 - \lambda_1)(x_2, y_2)$ and $\lambda_2(x_1, y_1) + (1 - \lambda_2)(x_2, y_2)$ satisfy the new criterion, then which one will be selected by Wang [5]?

The above example illustrates that in Wang's family of the preferred solutions for selection, if the decision-maker selects $z_2(0)$ and $z_2(2)$, then none of the convex combinations satisfy the new criterion. Wang did not tell us what the next step is when he failed to find $\lambda \in [0, 1]$.

V. CONCLUSION

This paper has carefully examined Wang's [5] approach to solve a fuzzy optimization problem when a new criterion preferred by the decision-maker is added to the fuzzy optimization problem. The consequence is that Wang's method derives an unwarranted solution. Furthermore, it demonstrates that Wang's [5] approach has a severe logic fault, and did not solve the fuzzy problem under the new conditions. Moreover, we have shown how, when the new criterion is added to Wang's example, one can derive the correct optimal solution. At last, we recall that Van Hop [12] referred to Wang [5] to develop his solution process to solve linear programming problems under fuzziness and randomness environment. Chou et al. [16] pointed out that there are questionable results in the solution process of Van Hop [12] and then Chou et al. [16] provided a revision for Van Hop [12].

REFERENCES

- [1] L.A. Zadeh, Fuzzy sets, Information Control, vol. 8, 1965, pp.338-353.

-
- [2] R.E. Bellman and L.A. Zadeh, "Decision-making in a fuzzy environment," *Management Science*, vol. 17, 1970, pp. 141-164.
- [3] H.J. Zimmermann, "Description and optimization of fuzzy system," *International Journal of General Systems*, vol. 2, 1976, pp. 209-216.
- [4] H.J. Zimmermann, "Fuzzy programming and linear programming with several objective functions," *Fuzzy Set and System*, vol. 1, 1978, pp. 45-55.
- [5] D. Wang, "An inexact approach for linear programming problems with fuzzy objective and resources," *Fuzzy Set and System*, vol. 89, 1997, pp. 61-68.
- [6] J. Tang, D. Wang, "An interactive approach based on a genetic algorithm for a type of quadratic programming problems with fuzzy objective and resources," *Computer and Operation Research*, vol. 24, 1997, pp. 413-422.
- [7] J. Tang, D. Wang, "A nonsymmetric model for fuzzy nonlinear programming problems with penalty coefficients," *Computers and Operations Research*, vol. 24, 1997, pp. 717-725.
- [8] S. He, R. Song, S.S. Chaudhry, "Fuzzy dispatching model and genetic algorithms for rail yards operations," *European Journal of Operations Research*, vol. 124, 2000, pp. 307-331.
- [9] R. Ma, X. Tan, X. Li, "Multi-objective fuzzy optimization model for daily active power dispatch," *Automation of Electric Power System*, Vol. 18, 2000, pp. 34.
- [10] J. Tang, D. Wang, R.Y.K. Fung, "Formulation of general probabilistic linear programming problems for complex industrial systems," *Fuzzy Set and System*, vol. 119, 2001, pp. 41-48.
- [11] N. Van Hop, "Solving fuzzy (stochastic) linear programming problems using superiority and inferiority measures," *Information Science*, vol. 177, 2007, pp. 1977-1991.
- [12] N. Van Hop, "Solving linear programming problems under fuzziness and randomness environment using attainment values," *Information Science*, vol. 177, 2007, pp. 2971-2984.
- [13] Y.-C. Chiu, L.C. Chang, F.J. Chang, "Using a hybrid genetic algorithm-simulated annealing algorithm for fuzzy programming of reservoir operation," *Hydrological Processes*, vol. 21, 2007, pp. 3162-3172.
- [14] H.-W. Lu, G.H. Huang, L. Liu, L. He, "An interval-parameter fuzzy-stochastic programming approach for air quality management under uncertainty," *Environmental Engineering Science*, vol. 25, 2008, pp. 895-909.
- [15] A. Baykasoglu and T. Gocken, "A review and classification of fuzzy mathematical programs," *Journal of Intelligent Fuzzy System*, vol. 19, 2008, pp. 205-229.
- [16] S. Y. Chou, J. S.J. Lin, P. Julian, "Solving linear programming problems under fuzziness and randomness environment using attainment values," *Information Science*, vol. 179, 2009, pp. 4083-4088.

Discussion of two motivations provided by Sphicas 2006

Pei-Chun Feng

Department of Administrative Management, Central Police University, Taiwan

Abstract—We discuss two motivations proposed by Sphicas (2006). First, after Lin (2019), we provide another partition for the feasible domain to show that there are at least three partitions to point out that the first motivation of Lin (2019) is not sufficient to support his solution procedure. For the second motivation of Sphicas (2006), we provide a detailed examination from the algebraic point of view to claim that his second motivation containing severe questionable results. We suggest researchers presenting a primitive algebraic method for inventory models with fixed and linear backorder costs.

Keywords—Inventory models, algebraic method, fixed backorder cost, linear backorder cost.

I. INTRODUCTION

Sphicas[1] is the first paper to use the algebraic method to solve inventory models with fixed and linear backorder costs. Sphicas [1] applied a genuine method to partition the domain into two cases and then derived the optimal solution by algebraic methods. However, his genuine method is too sophisticated that is beyond imagined of ordinary practitioners, such that Cárdenas-Barrón[2], Chung and Cárdenas-Barrón[3], and Sphicas [4] provided further discussions for the same inventory models. Recently, Lin [5] mentioned that the algebraic approach provided by Sphicas [1] is too complicated for ordinary readers to absorb the motivation explained by Sphicas [1]. Consequently, Cárdenas-Barrón[2], Chung and Cárdenas-Barrón [3], and Sphicas [4] provided different algebraic to solve the same inventory model with linear and fixed backorder costs. Lin [5] pointed out Cárdenas-Barrón[2] containing several severe problems and then Lin [5] claimed that a primitive approach will be an interesting research topic for future researchers. In this paper, we will provide further discussion for the motivation proposed by Sphicas [1] for his algebraic method.

II. NOTATION AND ASSUMPTIONS

Our paper is focused on discussion with Sphicas [1]. To be compatible with Sphicas [1], we will adopt the same notation and assumptions that were used in his paper.

Notation

D is the demand rate per unit of time.

h is the holding cost per unit, per unit of time.

K is the ordering cost (setup cost) per order.

p is the backorder cost per unit, per unit of time (linear backorder cost).

Q is the order quantity.

$Q - S$ is the beginning inventory level, after backlogged quantity S .

r is an auxiliary expression, with $r = (h/p)$.

S is the backlogged amount.

TC is the total cost per unit of time.

π is the backorder cost per unit (fixed backorder cost).

Assumptions

1. The model is developed for only one product.
2. The inventory model is developed for an infinite planning horizon such that the goal is to minimize the first (and repeated) replenishment cycle.

3. The demand rate is constant over the entire planning horizon.
4. The shortages are allowed and fully backlogged.
5. There are two types of backorder costs: a linear backorder cost that is applied to average backorders per unit of time and a fixed cost that is applied to maximum backorder level without considering the backlogged waiting period.

III. A REVIEW FOR THE PARTITION OF THE DOMAIN OF SPHICAS [1]

In the following, we will provide a detailed discussion for the partition of the domain into $D\pi \geq \sqrt{2hDK}$ and $D\pi < \sqrt{2hDK}$.

If we observe the optimal solution derived by Sphicas [1] for the ordering quantity, EOQ_2^* , as

$$EOQ_2^* = \sqrt{\frac{2DK(h+p) - \pi^2 D^2}{hp}} \quad (3.1)$$

to imply a positive solution for EOQ_2^* , then we will imply the following condition:

$$2DK(h+p) > \pi^2 D^2 \quad (3.2)$$

In Sphicas [1], he divided the solution procedure into two cases: Case (A):

$$D^2 \pi^2 \geq 2DKh \quad (3.3)$$

and Case (B):

$$2DKh > D^2 \pi^2 \quad (3.4)$$

Here, we must point out that for Case (A), under the restriction $D^2 \pi^2 \geq 2DKh$, Sphicas [1] mentioned that backlog is too expansive such that $S^* = 0$ and $Q^* = \sqrt{2DK/h}$ which is the traditional EOQ model without shortages.

For Case (B), under the restriction $2DKh > D^2 \pi^2$, Sphicas [1] derived

$$S = \frac{hQ - \pi D}{h + p} \quad (3.5)$$

then he plugged the finding of (3.1) into (3.5) to ensure $S > 0$ that is $Q > (\pi D/h)$ to find that the condition of (3.2), to guarantee $Q > 0$, is not enough to imply the backorder quantity is positive. A stronger the condition

$$2DKh > \pi^2 D^2 \quad (3.6)$$

Appears that is the Case (B) proposed by Sphicas [1].

For ordinary readers to accept the $2DK(h+p) > \pi^2 D^2$ after (3.1) already derived that is reasonable, since from the numerator $2DK(h+p) - \pi^2 D^2$, to guarantee the numerator is positive to derive the condition of (3.2) will be understandable by researchers.

However, it is too difficult for ordinary readers to predict that $2DKh > D^2 \pi^2$ of (3.4) in advance as proposed by Sphicas [1]. In Sphicas [1], he provided the first motivation for his approach as follows.

Based on Sphicas [1], the objective function for inventory models with two backorder costs: linear and fixed, is denoted as

$$TC(Q, S) = \frac{DK}{Q} + \frac{h(Q-S)^2}{2Q} + \frac{pS^2}{2Q} + \frac{DS\pi}{Q} \quad (3.7)$$

From (3.7), Sphicas [1] executed the following the derivation [1],

$$TC(Q, S) = \frac{h}{2Q} \left[(Q-S)^2 + \frac{2DK}{h} \right] + \frac{pS^2}{2Q} + \frac{DS\pi}{Q} \quad (3.8)$$

To complete the square of $(Q-S)^2 + \frac{2DK}{h}$, Sphicas [1] derived that

$$(Q-S)^2 + \frac{2DK}{h} = \left[(Q-S) - \sqrt{\frac{2DK}{h}} \right]^2 + 2(Q-S)\sqrt{\frac{2DK}{h}} \quad (3.9)$$

such that (3.8) is rewritten as follows

$$TC(Q, S) = \frac{h}{2Q} \left[(Q-S) - \sqrt{\frac{2DK}{h}} \right]^2 + \frac{pS^2}{2Q} + \frac{(D\pi - \sqrt{2DKh})S}{Q} + \sqrt{2DKh} \quad (3.10)$$

Sphicas [1] mentioned that if $D^2\pi^2 \geq 2DKh$, then all terms in (3.10), with non-negative coefficient such that the optimal solution for S should be zero, as $S^* = 0$, with $Q^* = \sqrt{2DK/h}$.

IV. A REVIEW FOR THE PARTITION OF THE DOMAIN OF LIN [5]

In Lin [5], he demonstrated that the rewriting of (3.7) is not unique. We recall the derivation of Lin (2009) since he rewrote (3.7) as follows

$$TC(Q, S) = \frac{1}{2Q} [pS^2 + 2DK] + \frac{h(Q-S)^2}{2Q} + \frac{DS\pi}{Q} \quad (4.1)$$

To complete the square of $pS^2 + 2DK$, Lin (2009) derived that

$$pS^2 + 2DK = \left[\sqrt{p}S - \sqrt{2DK} \right]^2 - 2\sqrt{2DKp}S \quad (4.2)$$

Such that (3.8) is rewritten as follows

$$TC(Q, S) = \frac{1}{2Q} \left[\sqrt{p}S + \sqrt{2DK} \right]^2 + \frac{h(Q-S)^2}{2Q} + \frac{(D\pi - \sqrt{2DKp})S}{Q} \quad (4.3)$$

If we observe (4.3), to make sure all coefficients are non-negative, then the next condition is derived,

$$D^2\pi^2 \geq 2DKp \quad (4.4)$$

V. OUR EXAMPLE TO PARTITION THE FEASIBLE DOMAIN

In this section, we will show another partition for the feasible domain to indicate there are at least three partitions for the feasible domain. We rewrite (3.7) as

$$TC(Q, S) = \frac{1}{2Q} \left[hQ^2 + (h+p)S^2 + 2DK - 2(hQ - \pi D)S \right] \quad (5.1)$$

under the restriction of $0 \leq S \leq Q$ and $0 < Q$.

If $hQ - \pi D \leq 0$, since $Q > 0$, $S \geq 0$ and $-2(hQ - \pi D) \geq 0$, all terms in (5.1) are non-negative such that we derive $S = 0$. The inventory model $TC(Q, S)$ is degenerated to the classical no shortage inventory model.

Based on the above discussion, we can divide the solution procedure into two cases: Case (i) $hQ \leq \pi D$, and Case (ii) $hQ > \pi D$. Hence, we construct another partition for the feasible domain. Owing to the partition for the feasible domain is not unique, the first motivation proposed by Sphicas [1] is not valid to convince researchers to accept his partition of (3.3) and (3.4).

VI. OUR DISCUSSION FOR THE SECOND MOTIVATION PROPOSED BY SPHICAS [1]

Lin [5] provided a comment on the second motivation for the solution approach of Sphicas [1]. However, Lin [5] considered the partial derivations in his discussion. Hence, we will not review the discussion mentioned by Lin [5] for the second motivation. In the following, we will provide our comments for the second motivation from an algebraic point of view.

We will present a further discussion for the second motivation proposed by Sphicas [1]. Sphicas [1] converted the objective function from

$$TC(Q, S) = \frac{DK}{Q} + \frac{h(Q-S)^2}{2Q} + \frac{pS^2}{2Q} + \frac{DS\pi}{Q} \quad (6.1)$$

to an indefinite expression,

$$TC = a_0 + a_1(Q-A)^2 + a_2(S-B)^2 \quad (6.2)$$

And Sphicas [1] claimed that "If it can be established that this can be done, if the coefficients are all nonnegative, and A and B are valid values for Q and S , then we can reach an immediate conclusion."

We recall that under the restriction $\pi D < \sqrt{2DKh}$, Sphicas [1] derived

$$TC = \frac{h}{h+p}(pK + \pi D) + \frac{hp}{2(h+p)Q} \left[Q - \sqrt{\frac{2DK(h+p) - \pi^2 D^2}{hp}} \right]^2 + \frac{h+p}{2Q} \left[S - \frac{hQ - \pi D}{h+p} \right]^2, \quad (6.3)$$

such that we point out that

$$a_0 = \frac{h}{h+p}(pK + \pi D) \quad (6.4)$$

$$a_1 = \frac{hp}{2(h+p)Q} \quad (6.5)$$

$$a_2 = \frac{h+p}{2Q} \quad (6.6)$$

$$A = \sqrt{\frac{2DK(h+p) - \pi^2 D^2}{hp}} \quad (6.7)$$

and

$$B = \frac{hQ - \pi D}{h + p} \quad (6.8)$$

Based on our observation of (6.2-6.8), we can say that the motivation of Sphicas [1] is to transform TC from (3.1) to

$$TC = a_0 + \frac{a_1}{Q}(Q - A)^2 + \frac{a_2}{Q}(S - f(Q))^2 \quad (6.9)$$

where $f(Q)$ is an expression only in a variable Q , that will be $f(Q) = (hQ - \pi D)/(h + p)$.

Now, we assume that we know the final result of (6.9) in advance. We rewrite (6.9) as

$$\begin{aligned} TC &= a_0 + \frac{a_1}{Q}(Q^2 - 2AQ + A^2) + \frac{a_2}{Q}(S^2 - 2f(Q)S + (f(Q))^2), \\ &= a_0 + a_1Q - 2a_1A + a_1\frac{A^2}{Q} + a_2\frac{S^2}{Q} - 2a_2f(Q)\frac{S}{Q} + \frac{a_2}{Q}(f(Q))^2. \end{aligned} \quad (6.10)$$

On the other hand, we rewrite (6.1) as

$$TC = \frac{DK}{Q} + \frac{h}{2} - hS + \frac{p+h}{2Q}S^2 + \pi D\frac{S}{Q} \quad (6.11)$$

We compare (6.10) and (6.11) to imply that

$$a_2 = \frac{h+p}{2} \quad (6.12)$$

For those terms containing S , we obtain

$$-h + \frac{\pi D}{Q} = -2\left(\frac{h+p}{2}\right)\frac{f(Q)}{Q} \quad (6.13)$$

Based on (6.13), we derive the desired result of $f(Q)$ as

$$f(Q) = \frac{hQ - \pi D}{h + p} \quad (6.14)$$

We plug (6.12) and (6.14) into (6.1) to find

$$TC = \frac{h\pi D}{h+p} + \frac{2DK(h+p) - \pi^2 D^2}{2(h+p)Q} + \frac{hp}{2(h+p)}Q + \frac{h+p}{2Q}\left[S - \frac{hQ - \pi D}{h+p}\right]^2 \quad (6.15)$$

We rewrite the second and third terms of (6.15) to obtain

$$\begin{aligned} TC &= \frac{h\pi D}{h+p} + \left(\sqrt{\frac{2DK(h+p) - \pi^2 D^2}{2(h+p)Q}}\right)^2 + \left(\sqrt{\frac{hp}{2(h+p)}}Q\right)^2 + \frac{h+p}{2Q}\left[S - \frac{hQ - \pi D}{h+p}\right]^2 \\ &= \frac{h\pi D}{h+p} + \left\{\left(\sqrt{\frac{2DK(h+p) - \pi^2 D^2}{2(h+p)Q}}\right) - \left(\sqrt{\frac{hp}{2(h+p)}}Q\right)\right\}^2 \end{aligned}$$

$$\begin{aligned}
& + 2 \left(\sqrt{\frac{2DK(h+p) - \pi^2 D^2}{2(h+p)Q}} \right) \left(\sqrt{\frac{hp}{2(h+p)Q}} Q \right) + \frac{h+p}{2Q} \left[S - \frac{hQ - \pi D}{h+p} \right]^2 \\
& = \frac{h(pK + \pi D)}{h+p} + \left\{ \left(\sqrt{\frac{2DK(h+p) - \pi^2 D^2}{2(h+p)Q}} \right) - \left(\sqrt{\frac{hp}{2(h+p)Q}} Q \right) \right\}^2 \\
& \quad + \frac{h+p}{2Q} \left[S - \frac{hQ - \pi D}{h+p} \right]^2, \\
& = \frac{h}{h+p} (pK + \pi D) + \frac{hp}{2(h+p)Q} \left[Q - \sqrt{\frac{2DK(h+p) - \pi^2 D^2}{hp}} \right]^2 + \frac{h+p}{2Q} \left[S - \frac{hQ - \pi D}{h+p} \right]^2 \quad (6.16)
\end{aligned}$$

Our derivation of (6.16) is the result of (6.3) proposed by Sphicas [1].

If researchers know the final result of TC as (6.3) in advance, then following our above derivation, then the algebraic method proposed by Sphicas [1] becomes crystal clear.

The expression of (6.2) proposed by Sphicas [1] looks reasonable and intuitively acceptable. However, in fact, Sphicas [1] really needed the expression that should be expressed as (6.9).

However, for ordinary practitioners, unless you know the final result of (6.16) in advance, to accept the expression of (6.9) is questionable.

Therefore, the motivation of (6.2) provided by Sphicas [1] is not proper, the exact motivation should be revised to (6.9). Hence, we point out the second motivation provided by Sphicas [1] which is not sufficient to support the solution procedure in Sphicas [1].

VII. CONCLUSIONS

Even after Sphicas [1] provided two motivations for his algebraic approach, ordinary researchers still cannot understand the algebraic approach proposed by Sphicas [1]. Consequently, Cárdenas-Barrón[2], Chung and Cárdenas-Barrón [3], and Sphicas [4] provide further discussions for inventory models with fixed and linear backorder costs. Lin [5] discussed one motivation provided by Sphicas [1] and then we improve a typo in the discussion of Lin [5]. Moreover, we show that the second motivation proposed by Sphicas [1] containing more severe questionable results. Hence, we can claim that a primitive derivation for inventory models with fixed and linear backorder costs should be a hot research issue for academic society.

REFERENCES

- [1] G.P.Sphicas, "EOQ and EPQ with linear and fixed backorder costs: Two cases identified and models analyzed without calculus," International Journal of Production Economics, vol. 100, 2006, pp. 59-64.
- [2] L.E.Cárdenas-Barrón, "The derivation of EOQ/EPQ inventory models with two backorders costs using analytic geometry and algebra," Applied Mathematics Model, vol. 35, 2011, pp. 2394-2407.
- [3] K. Chung, L. E. Cárdenas-Barrón, "The complete solution procedure for the EOQ and EPQ inventory models with linear and fixed backorder costs," Mathematical and Computer Modeling, vol. 55, 2012, pp. 2151-2156.
- [4] G.P.Sphicas, "Generalized EOQ formula using a new parameter: Coefficient of backorder attractiveness," International Journal of Production Economics, Vol. 155, 2014, pp. 143-147.
- [5] S.C.Lin, "Note on The derivation of EOQ/EPQ inventory models with two backorders costs using analytic geometry and algebra," Applied Mathematics Model, vol. 73, 2019, pp. 378-386.

Discussion on Weighted Similarity Measure under Intuitionistic Fuzzy Sets Environment

Edward Lin¹, Daniel Schaeffer²

¹Chaminade College Preparatory, USA

²Department of Mathematics, National Tsing Hua University, Taiwan

Abstract— We analytically show that the findings of pattern recognition problems with weighted similarity measures under intuitionistic fuzzy sets environment that is dominated by relative weights of elements in the universe of discourse for the discrete case and the weighted function for the continuous case. In the past, researchers focus on constructing new similarity measures or developing new algorithms applying their similarity measures. Hence, previous results depended on a special weight to decide the pattern of the sample that may be required further considerations. How to select a proper weight will be an important issue for researchers in the future when deal with pattern recognition problems.

Keywords— Pattern recognition, intuitionistic fuzzy sets, similarity measure.

I. INTRODUCTION

More and more business had being developed in the real world, so it is hard for a company to get accurate market data. Therefore, fuzzy set data may be a kind of data that can be obtained more easily to explain the market and managerial situation. If the data is a traditional fuzzy set, there are some methods to be applied to solve the fuzzy problem. Recently, many similarity measures have been proposed, for examples, Hung and Lin [1], Julian et al. [2], Hung and Lin [3], Tung et al. [4], Yen et al. [5], Hung and Wang [6], Chu and Guo [7], Hung et al. [8], and Tung and Hopscotch [9], for measuring the degree of similarity between fuzzy sets, under a kind of special fuzzy sets, which is called Intuitionistic Fuzzy Sets (IFSs) that were initiated presented by Atanassov [10, 11]. Since Atanassov originated the idea of IFSs, many different similarity measures between IFSs have been proposed in the literature. Atanassov and Ranganamy[12] and Kuppannan et al. [13] provided practical applications for IFSs. The importance of suitable distance measures between IFSs takes place because they play an important role in the theoretical development and implication problem. Two existing similarity measures for IFSs were proposed by Li and Cheng [14] to indicate the dominated factor for the selection of pattern recognition problems. This paper is a detailed analysis for the similarity measure of intuitionistic fuzzy sets (IFSs) in Li and Cheng [14]. Mitchell [15] already provided an example to demonstrate that the similarity measure proposed by Li and Cheng [14] may lead to counter-intuitive result. However, there are 373 papers continuously referred to Li and Cheng [14]. Owing to the high citation, it deserves a detailed study of their paper. To be compatible with previous results, we directly study the examples of Li and Cheng [14] to show that their weighted similarity measures contained inherent problems that is their results are dependent on weights of elements in the universe of discourse for the discrete case and the weighted function for the continuous case. Hence, how to derive the weights or the weighted function should be the crucial issue in the future research. Our consideration will offer a patch work to enhance the operational development of similarity measure for pattern recognition under IFSs. Recently, there is a trend to improve published papers, for example, Hung et al. [16], Lin et al. [17], Tung [18], and Chao et al. [19]. Following this trend, we will provide improvements for Li and Cheng [14]. In this paper, based on the same numerical examples of Li and Cheng [14], we will demonstrate that the proposed measures of Li and Cheng [14] performs dependent on the relative weight in pattern recognition. Our findings presented here could arouse attention to take care of the decision of relative weights in the selection and applications of similarity measures for IFSs and vague sets in practice.

II. MATERIALS AND METHODS

Let X be a fixed set. An IFS A in X is an object having the form $A = \{ \langle x, t_A(x), f_A(x) \rangle | x \in X \}$ where the function $t_A : X \rightarrow [0,1]$ and $f_A : X \rightarrow [0,1]$ define the degree of membership and degree of non-membership, respectively, and for every $x \in X$, $0 \leq t_A(x) + f_A(x) \leq 1$. Let $IFSS(X)$ denote the set of all IFSs in X . Next, we define the order relation. $A, B \in IFSS(X)$, $A \subseteq B$ is defined as $t_A(x) \leq t_B(x)$ and $f_A(x) \geq f_B(x)$ for every $x \in X$.

For a pattern recognition problem, if a pattern A_{i_0} satisfies $S(A_{i_0}, B) = \max_{1 \leq i \leq m} S(A_i, B)$, and $S(A_{i_0}, B) > \max_{1 \leq i \leq m, i \neq i_0} S(A_i, B)$ according to the principle of the maximum degree of similarity between IFSs, researchers can decide that the sample B belongs to the pattern A_{i_0} .

In the following two numerical examples, we will show that the similarity measures of Li and Cheng [14] will dependent on the relative weights of IFS so their approach may cause different results for pattern recognition problems when the relative weights are arbitrary selected.

For the discrete case with the universe of discourse $X = \{x_1, x_2, \dots, x_n\}$, Li and Cheng [14] assumed the similarity measure between two IFSs A and B as

$$S_d^p(A, B) = 1 - \frac{1}{\sqrt[p]{n}} \sqrt[p]{\sum_{i=1}^n (\varphi_A(i) - \varphi_B(i))^p} \quad (1)$$

Where

$$\varphi_A(x_i) = \frac{t_A(x_i) + 1 - f_A(x_i)}{2} \quad (2)$$

Which was introduced originally in Tanev [20].

2.1 Example 1 of Li and Cheng [14].

There are three patterns in IFSs of

$$X = \{x_1, x_2, x_3\},$$

$$A_1 = \{\langle 1, 0 \rangle, \langle 0.8, 0 \rangle, \langle 0.7, 0.1 \rangle\}, A_2 = \{\langle 0.8, 0.1 \rangle, \langle 1, 0 \rangle, \langle 0.9, 0 \rangle\}, A_3 = \{\langle 0.6, 0.2 \rangle, \langle 0.8, 0 \rangle, \langle 1, 0 \rangle\},$$
 respectively,

where $t_{A_1}(x_1) = 1$ and $f_{A_1}(x_1) = 0$ for pattern A_1 . Consider a sample $B \in IFSs(X)$ which will be recognized, with

$$B = \{\langle 0.5, 0.3 \rangle, \langle 0.6, 0.2 \rangle, \langle 0.8, 0.1 \rangle\}. \text{ We referred their findings in the next table.}$$

➤ Notation

D is the demand rate per unit of time.

h is the holding cost per unit, per unit of time.

K is the ordering cost (setup cost) per order.

p is the backorder cost per unit, per unit of time (linear backorder cost).

Q is the order quantity.

$Q - S$ is the beginning inventory level, after backlogged quantity S .

r is an auxiliary expression, with $r = (h/p)$.

S is the backlogged amount.

TC is the total cost per unit of time.

π is the backorder cost per unit (fixed backorder cost).

➤ Assumptions

1. The model is developed for only one product.

2. The inventory model is developed for an infinite planning horizon such that the goal is to minimize the first (and repeated) replenishment cycle.
3. The demand rate is constant over the entire planning horizon.
4. The shortages are allowed and fully backlogged.
5. There are two types of backorder costs: a linear backorder cost that is applied to average backorders per unit of time and a fixed cost that is applied to maximum backorder level without considering the backlogged waiting period.

TABLE 1
SUMMARY OF THEIR FINDINGS IN LI AND CHENG [14]

				$S_d^p(A_1, B)$	$S_d^p(A_2, B)$	$S_d^p(A_3, B)$
$x_1 = 1/3$	$x_2 = 1/3$	$x_3 = 1/3$	$p = 1$	0.78	0.80	0.85
$x_1 = 1/3$	$x_2 = 1/3$	$x_3 = 1/3$	$p = 2$	0.74	0.78	0.84
$x_1 = 0.5$	$x_2 = 0.3$	$x_3 = 0.2$	$p = 2$	0.696	0.779	0.853

Based on the similarity measure on the above table, Li and Cheng [14] concluded that the sample B belongs to the pattern A_3 .

For the continuous case, Li and Cheng [14] assumed the similarity measure of two IFSs A and B as

$$S(A, B) = 1 - \int_a^b w(x) [\varphi_A(x) - \varphi_B(x)] dx \quad (3)$$

where $w(x)$ is the weight function. For the continuous case, they applied the uniform distribution with weight $\omega(t): [a, b] \rightarrow [0, 1]$, $\int_a^b \omega(t) dt = 1$ so that they used $\omega(t) = 1/(b-a)$, for $a \leq t \leq b$.

2.2 Example 2 of Li and Cheng [14].

They assumed that two patterns, A_1 and A_2 with a sample, B are represented by IFSs, where

$$t_{A_1}(x) = \begin{cases} 0.8(x-1), & 1 \leq x < 2, \\ 4(5-x)/15, & 2 \leq x \leq 5, \end{cases} \quad (4)$$

$$f_{A_1}(x) = \begin{cases} 1.9 - 0.9x, & 1 \leq x < 2, \\ 0.3x - 0.5, & 2 \leq x \leq 5, \end{cases} \quad (5)$$

$$t_{A_2}(x) = \begin{cases} 0.2(x-1), & 1 \leq x < 4, \\ 0.6(5-x), & 4 \leq x \leq 5 \end{cases} \quad (6)$$

$$f_{A_2}(x) = \begin{cases} 1.3 - 0.3x, & 1 \leq x < 4, \\ 0.9x - 3.5, & 4 \leq x \leq 5, \end{cases} \quad (7)$$

$$t_B(x) = \begin{cases} 0.3(x-1), & 1 \leq x < 3, \\ 0.3(5-x), & 3 \leq x \leq 5 \end{cases} \quad (8)$$

$$f_B(x) = \begin{cases} 1.4-0.4x, & 1 \leq x < 3, \\ 0.4x-1, & 3 \leq x \leq 5. \end{cases} \quad (9)$$

We recall their findings of $S(A_1, B) = 0.85$ and $S(A_2, B) = 0.86$ such that Li and Cheng [14] claimed that sample B should belong to the pattern A_2 .

III. RESULTS

3.1 Our discussion for Example 1 of [14]

Based on equation (2), we derive that $\varphi_{A_1} = (1.0, 0.9, 0.8)$, $\varphi_{A_2} = (0.85, 1.0, 0.95)$, $\varphi_{A_3} = (0.7, 0.9, 1.0)$ and $\varphi_B = (0.6, 0.7, 0.85)$. For the discrete case, we assume that the weight is $(\omega_1, \omega_2, \omega_3)$ under the condition $p = 1$, and then we recall the 1-norm distance, say $d(A_i, B)$ with $d(A_i, B) = 1 - S_d^1(A_i, B)$. Hence, we know that to have the maximum similarity is equivalent to have the minimum distance. We find that

$$d(A_1, B) = 0.4\omega_1 + 0.2\omega_2 + 0.05\omega_3, \quad (10)$$

$$d(A_2, B) = 0.25\omega_1 + 0.3\omega_2 + 0.1\omega_3, \quad (11)$$

and

$$d(A_3, B) = 0.1\omega_1 + 0.2\omega_2 + 0.15\omega_3. \quad (12)$$

From the above derivation, if we select that $\omega_1 = 0.1$, $\omega_2 = 0.1$ and $\omega_3 = 0.8$, then it yields that

$$d(A_1, B) = 0.1 < d(A_2, B) = 0.135 < d(A_3, B) = 0.15 \quad (13)$$

then the sample B belongs to the pattern A_1 .

On the other hand, if $\omega_1 = 0.3$, $\omega_2 = 0.1$ and $\omega_3 = 0.6$, then it yields that

$$d(A_3, B) = 0.14 < d(A_2, B) = 0.165 < d(A_1, B) = 0.17 \quad (14)$$

then the sample B belongs to the pattern A_3 .

In the following, we will develop a theoretical result to show that sample B cannot be classified to the pattern A_2 .

Lemma 1.

$$S(A_2, B) = \max \{S(A_i, B) : i = 1, 2, 3\} \text{ if and only if } w_1 = 0.25, w_2 = 0 \text{ and } w_3 = 0.75.$$

(Proof of Lemma 1) We assume $\omega_1 = x$, $\omega_2 = y$ and $\omega_3 = 1 - x - y$ to simplify the expression. It yields that

$$d(A_2, B) \leq d(A_1, B) \text{ if and only if}$$

$$0.2x \geq 0.05y + 0.05. \quad (15)$$

On the other hand, we know that $d(A_2, B) \leq d(A_3, B)$ if and only if

$$0.2x + 0.15y \leq 0.05 \quad (16)$$

If we want $d(A_2, B)$ is the smallest distance, then from equations (15) and (16), it follows that

$$0.2x \geq 0.25y + 0.05 \geq 0.2x + 0.2y \quad (17)$$

By equation (17), it implies that $y = 0$, $x = 0.25$ and

$$d(A_2, B) = d(A_1, B) = d(A_3, B) \quad (18)$$

Therefore, under the usual condition, three weights, w_1 , w_2 and w_3 are all positive so we cannot construct an example in which the sample B belongs to the pattern A_2 such that we derive the next theorem.

Theorem 1.

Under the conditions $w_i > 0$, for $i = 1, 2, 3$ and $w_1 + w_2 + w_3 = 1$ then sample B cannot be decided belonging to pattern A_2 .

Based on above discussion, different relative weights will imply different patterns for the given sample. Our work demonstrates that the weights of IFSs are the most essential factor to decide the sample B belongs to which pattern.

3.2 Our discussion for Example 2 of [14]

According to equation (2), we follow Li and Cheng [14] approach to transfer three IFSs into ordinary fuzzy sets as

$$\varphi_{A_1}(x) = \begin{cases} 0.85(x-1), & 1 \leq x < 2, \\ 17(5-x)/60, & 2 \leq x \leq 5, \end{cases} \quad (19)$$

$$\varphi_{A_2}(x) = \begin{cases} 0.25(x-1), & 1 \leq x < 4, \\ 3(5-x)/4, & 4 \leq x \leq 5, \end{cases} \quad (20)$$

and

$$\varphi_B(x) = \begin{cases} 0.35(x-1), & 1 \leq x < 3, \\ 0.35(5-x), & 3 \leq x \leq 5. \end{cases} \quad (21)$$

We will show that different weight function $\omega(x)$ will influence the results for the pattern selection. We assume that

$$\omega(x) = \begin{cases} \lambda_1, & 1 \leq x < 3, \\ \lambda_2, & 3 \leq x \leq 5, \end{cases} \quad (22)$$

under the condition that $0 \leq \lambda_1$, $0 \leq \lambda_2$, and $\lambda_1 + \lambda_2 = 0.5$.

Remark. The restriction of $\lambda_1 + \lambda_2 = 0.5$ is our special treatment such that the uniform weighted function, where $\omega(x) = 0.25$, for $1 \leq x \leq 5$, proposed by Li and Cheng [14] contains in our design of Equation (22).

We will develop next two lemmas to help us to decide the similarity measure for the continuous case.

Lemma 2. We show that

$$S(A_1, B) = 1 - \lambda_1 a_1 - \lambda_2 b_1, \quad (23)$$

$$\text{where } a_1 = \frac{\varphi_{A_1}(2)}{2} + \left(\frac{\varphi_{A_1}(2) + \varphi_{A_1}(3)}{2} \right) + \varphi_B(3) - 2 \left[\left(\varphi_{A_1}(3) + \varphi_{A_1}(c_1) \right) \frac{3-c_1}{2} + \varphi_{A_1}(c_1) \frac{c_1-1}{2} \right],$$

$$b_1 = \left(\varphi_B(3) - \varphi_{A_1}(3) \right) \left(\frac{5-3}{2} \right)$$

with c_1 is the x-coordinate of the intersection of $\varphi_{A_1}(x)$ and $\varphi_B(x)$ for $1 < x < 5$.

(Proof of Lemma 2) We know that $\frac{\varphi_{A_1}(2)}{2}$ is the area of the triangle from φ_{A_1} and the area of the trapezoid is $\frac{\varphi_{A_1}(2) + \varphi_{A_1}(3)}{2}$ from φ_{A_1} . Moreover, $\varphi_B(3)$ is the area of the triangle from φ_B , $\left[\varphi_{A_1}(3) + \varphi_{A_1}(c_1) \right] \frac{3-c_1}{2}$ is the area of the area of a trapezoid from φ_{A_1} , and $\varphi_{A_1}(c_1) \frac{c_1-1}{2}$ is an area of a triangle by φ_{A_1} . Hence, the integration of $\lambda_1 \int_1^3 [\varphi_{A_1}(x) - \varphi_B(x)] dx$ can be simplify as $\lambda_1 a_1$.

Consequently, we can derive the same result for the similarity measure between pattern A_2 and sample B .

Lemma 3. We show that

$$S(A_2, B) = 1 - \lambda_1 a_2 - \lambda_2 b_2, \quad (24)$$

$$\text{where } a_2 = \left(\varphi_B(3) - \varphi_{A_2}(3) \right) \left(\frac{3-1}{2} \right)$$

$$b_2 = \frac{\varphi_{A_2}(4)}{2} (5-4) + \left(\frac{\varphi_{A_2}(4) + \varphi_{A_2}(3)}{2} \right) + \varphi_B(3) - 2 \left[\left(\varphi_{A_2}(3) + \varphi_{A_2}(c_2) \right) \frac{c_2-3}{2} + \varphi_{A_2}(c_2) \frac{5-c_2}{2} \right]$$

with c_2 is the x-coordinate of the intersection of $\varphi_{A_2}(x)$ and $\varphi_B(x)$, for $1 < x < 5$.

If we consider the same data as the second example of Li and Cheng [14], based on the assumptions in Lemma 2 for a_1 and b_1 , we derive that $a_1 = 0.461404$ and $b_1 = 0.133333$. By the same argument, based on the assumptions in Lemma 3 for a_2 and b_2 , we derive that $a_2 = 0.2$ and $b_2 = 0.366667$. Hence, we know that

$$S(A_1, B) = 1 - 0.461404\lambda_1 - 0.133333\lambda_2, \quad (25)$$

and

$$S(A_2, B) = 1 - 0.2\lambda_1 - 0.366667\lambda_2. \quad (26)$$

We list some possible combination of different λ_1 and λ_2 , under the restriction $\lambda_1 + \lambda_2 = 0.5$ in the next table.

TABLE 2
NUMERICAL EXAMPLE OF [14] UNDER CONTINUOUS CASE

	$\lambda_1 = 0.1$	$\lambda_1 = 0.2$	$\lambda_1 = 0.25$	$\lambda_1 = 0.3$	$\lambda_1 = 0.4$
$S(A_1, B)$	0.900526	0.867719	0.851316	0.834912	0.802105
$S(A_2, B)$	0.833333	0.85	0.858333	0.866667	0.883333

First, we observe that the findings of Li and Cheng [14] with $S(A_1, B) = 0.85$ and $S(A_2, B) = 0.86$ that is consistent with our derivations in Table 2, where our results are $S(A_1, B) = 0.851316$ and $S(A_2, B) = 0.858333$, after we round off the second decimal place, then the findings of Li and Cheng [14] are derived.

Motivated by the numerical examples for similarity measure of the table 2, we will derive a theoretical result to clearly point out that the pattern recognition is strongly influence by the weighted function $\omega(t)$.

Lemma 4. There is a unique point, say λ_0 such that

(1) if $0 \leq \lambda_1 \leq \lambda_0$, then $S(A_1, B) \geq S(A_2, B)$, and

(2) if $\lambda_0 \leq \lambda_1 \leq 0.5$, then $S(A_1, B) \leq S(A_2, B)$.

(Proof of Lemma 4)

Motivated by $a_1 = 0.461404 > a_2 = 0.2$ and $b_1 = 0.133333 < b_2 = 0.366667$, we will abstractly express equations (25) and (26) as follows:

$$S(A_1, B) = 1 - \alpha_1 \lambda_1 - \beta_1 \lambda_2, \quad (27)$$

and

$$S(A_2, B) = 1 - \alpha_2 \lambda_1 - \beta_2 \lambda_2, \quad (28)$$

where

$$\alpha_1 = \frac{\varphi_{A_1}(2)}{2} + \left(\frac{\varphi_{A_1}(2) + \varphi_{A_1}(3)}{2} \right) + \varphi_B(3) - 2 \left[\left(\varphi_{A_1}(3) + \varphi_{A_1}(c_1) \right) \frac{3-c_1}{2} + \varphi_{A_1}(c_1) \frac{c_1-1}{2} \right], \quad (29)$$

$$\beta_1 = \left(\varphi_B(3) - \varphi_{A_1}(3) \right) \left(\frac{5-3}{2} \right), \quad (30)$$

$$\alpha_2 = \left(\varphi_B(3) - \varphi_{A_2}(3) \right) \left(\frac{3-1}{2} \right) \quad (31)$$

and

$$\beta_2 = \frac{\varphi_{A_2}(4)}{2} + \left(\frac{\varphi_{A_2}(4) + \varphi_{A_2}(3)}{2} \right) + \varphi_B(3) - 2 \left[\left(\varphi_{A_2}(3) + \varphi_{A_2}(c_2) \right) \frac{c_2-3}{2} + \varphi_{A_2}(c_2) \frac{5-c_2}{2} \right], \quad (32)$$

under the condition of $\alpha_1 > \alpha_2$ and $\beta_2 > \beta_1$.

We derived that $S(A_1, B) \geq S(A_2, B)$ is equivalent to

$$0.5(\beta_2 - \beta_1) \geq [(\beta_2 - \beta_1) + (\alpha_1 - \alpha_2)]\lambda_1. \quad (33)$$

Hence, we knew that there is a point, say λ_0 , with

$$\lambda_0 = 0.5(\beta_2 - \beta_1) / [(\beta_2 - \beta_1) + (\alpha_1 - \alpha_2)], \quad (34)$$

and then if $0 \leq \lambda_1 \leq \lambda_0$, then $S(A_1, B) \geq S(A_2, B)$, and if $\lambda_0 \leq \lambda_1 \leq 0.5$, then $S(A_1, B) \leq S(A_2, B)$.

For completeness, for the Example 2 of Li and Cheng [14], we find the value of λ_0 as $\lambda_0 = 0.235816$. From our previous discussion, it points out that the selection of pattern for the given sample is dependent on the weight function $\omega(x)$. Li and Cheng [14] asserted that the sample B always belonging to pattern A_2 is questionable.

Theorem 2.

If the weighted function $\omega(x)$ is expressed as equation (22), then

(a) If $0 \leq \lambda_1 < 0.235816$, then sample B belongs to pattern A_1 ;

(b) If $0.235816 < \lambda_1 \leq 0.5$, then sample B belongs to pattern A_2

IV. CONCLUSION

A similarity measure is a useful tool for determining the similarity of two objects. Based on the same numerical examples of Li and Cheng [14], we demonstrated that their proposed similarity measures are dominated by the relative weight of the domain for IFS in pattern recognition problems. In the past, researchers focus on developing new similarities to replace previous established similarity measures, moreover, Yen et al. [5], Hung et al. [8], Chu et al. [21] and Chou [22] constructed algorithms that is related to the size of universe of discourse for the discrete cases to repeatedly applied their proposed similarity measures. However, Yen et al. [4], Hung et al. [8], Chu et al. [21] and Chou [22] did not pay attention to how to decide relative weights for elements in the universe of discourse. Based on our discussion, we show that applying the same similarity measure with different relative weights will result in different finding for pattern recognition problems. Consequently, we point out their proposed measures to analyze the behavior of decision making that should be put more attention to the relative weight of the domain for an IFS.

REFERENCES

- [1] K.Hung, K. Lin, "A new intuitionistic fuzzy cosine similarity measures and its application," IEEE International Conference on Industrial Engineering and Engineering Management, 2012, pp. 2194-2198.
- [2] P. Julian, K. Hung, S. Lin, "On the Mitchell similarity measure and its application to pattern recognition," Pattern Recognition Letters, vol. 33, 2012, pp. 1219-1223.
- [3] K. Hung, K. Lin, "Long-term business cycle forecasting through a potential intuitionistic fuzzy least-squares support vector regression approach," Information Science, vol. 224, 2013, pp. 37-48.
- [4] C. Tung, S. Liu, B. S. Wang, "A comment on "on the Mitchell similarity measure and its application to pattern recognition," Pattern Recognition Letter, vol. 34, .2013, pp. 453-455.
- [5] P. C. P. Yen, K. Fan, H. C. Chao, "A new method for similarity measures for pattern recognition," Applied Mathematical Modeling, vol. 37, 2013, pp. 5335-5342.
- [6] K. Hung, P. Wang, "An integrated intuitionistic fuzzy similarity measures for medical problems," International Journal of Computational Intelligence Systems, vol. 7, 2014, pp. 327-343.
- [7] C. Chu, Y. Guo, "Developing similarity based IPA under intuitionistic fuzzy sets to assess leisure bikeways," Tourism Management, vol. 47, 2015, pp. 47-57.
- [8] K. Hung, J. Lin, P. Chu, "An extended algorithm of similarity measures and its application to radar target recognition based on intuitionistic fuzzy sets," Journal of Testing and Evaluation, vol. 43, 2015, pp. 878-887.
- [9] C. Tung, C. Hopscotch, "Discussion on similarity measure of its complement," Journal of Discrete Mathematical Sciences and Cryptography, vol. 18, 2015, pp. 417-432.
- [10] K. Atanassov, "Intuitionistic fuzzy sets," Fuzzy Set and System, vol. 20, 1986, pp. 87-96.

- [11] K. Atanassov, *Intuitionistic Fuzzy Sets: Theory and Applications*, Springer, Heidelberg, 1999.
- [12] K. Atanassov, P. Rangasamy, "On intuitionistic fuzzy sets and interval valued intuitionistic fuzzy sets," *Advanced Studies in Contemporary Mathematics*, vol. 18, 2009, pp. 1-8.
- [13] J. Kuppannan, P. Rangasamy, D. Thirupathi, N. Palaniappan, "Intuitionistic fuzzy approach to enhance text documents," *IEEE Transactions on Intelligent Transportation Systems*, 2006, pp. 733-737.
- [14] D. Li, C. Cheng, "New similarity measure of intuitionistic fuzzy sets and application to pattern recognitions," *Pattern Recognition Letters*, vol. 23, .2002, pp. 221-225.
- [15] H. B. Mitchell, "On the Dengfeng - Chuntian similarity measure and its application to pattern recognition," *Pattern Recognition Letters*, vol. 24, .2003, pp. 3101-3104.
- [16] K. Hung, W. T. Chouhuang, G. K. Yang, P.C. Julian, "An efficient Newton-Raphson procedure for determining the optimal inventory replenishment policy," *Journal of the Chinese Institute of Engineers* , vol. 25, 2008, pp. 237-246.
- [17] J. Lin, H. C. Chao, P. Julian, "Improved solution process for inventory model with ramp-type demand under stock-dependent consumption rate," *Journal of the Chinese Institute of Engineers*, vol. 29, 2012, pp. 219-225.
- [18] C. Tung, "A note on the inventory models with ramp type demand of negative exponentially distributed changing point," *Journal of Industrial and Production Engineering*, vol. 30, 2013, pp. 15-19.
- [19] H. C. Chao, S. Lin, J. Lin, "Reply to a note on the inventory models with ramp-type demand of negative exponentially distributed changing point," *Journal of Production Engineering*, vol. 31, .2014, pp. 359-362.
- [20] D. Tanev, "On the intuitionistic fuzzy norm," *Intuitionistic Fuzzy Logics*, vol. 1, 1995, pp. 25-26.
- [21] C. S. Chu, K. C. Hung, P. Julian, "A complete pattern recognition approach under Atanassov's intuitionistic fuzzy sets," *Knowledge-Based System*, vol. 66, 2014, pp. 36-45.
- [22] W. Chou, "New algorithm of similarity measures for pattern-recognition problems," *Journal of Testing and Evaluation*, vol. 44, 2016, pp. 1473-1484.



AD Publications

**Sector-3, MP Nagar, Bikaner,
Rajasthan, India**

www.adpublications.org, info@adpublications.org